



## An Analysis of Surface Currents in the Western Beaufort and Northeastern Chukchi Seas

### Principal Investigators:

Rachel A. Potter

Seth L. Danielson

College of Fisheries and Ocean Sciences  
University of Alaska Fairbanks

Final Report

May 2022

OCS Study BOEM 2022-014

## An Analysis of Surface Currents in the Western Beaufort and Northeastern Chukchi Seas



Photo credit: Surface capillary wave field with swell and patches of surface flow divergence (slick areas) in the northeastern Chukchi Sea, 15 August 2015. Photograph by Seth Danielson.

Citation: Potter, R.A. and S.L. Danielson, 2022. An Analysis of Surface Currents in the Western Beaufort and Northeastern Chukchi Seas. Final Report, OCS Study BOEM 2022-014, University of Alaska Coastal Marine Institute and USDO, BOEM Alaska OCS Region.

### Contact Information:

*uaf-cmi@alaska.edu*

<https://www.uaf.edu/cfos/research/cmi>

This study was funded by the U.S. Department of the Interior, Bureau of Ocean Energy Management Alaska OCS Region and the University of Alaska Fairbanks through Cooperative Agreement M20AC00001. This report is available online at <https://www.boem.gov/akpubs>.

The views and conclusions contained in this document are those of the authors and should not be interpreted as representing the opinions or policies of the U.S. Government. Mention of trade names or commercial products is not an endorsement by the U.S. Government.

## Table of Contents

<b>List of Tables</b> .....	<b>iv</b>
<b>List of Figures</b> .....	<b>iv</b>
<b>List of Appendix Figures</b> .....	<b>ix</b>
<b>Executive Summary</b> .....	<b>xi</b>
<b>1.0 Introduction</b> .....	<b>1</b>
<b>2.0 Methods</b> .....	<b>5</b>
2.1 High-Frequency Radar Data .....	5
2.2 Moored Acoustic Doppler Current Profiler Data.....	9
2.3 Satellite-Tracked Drifter Data.....	11
2.4 Meteorological Data.....	12
2.5 Analyses .....	13
<b>3.0 Results</b> .....	<b>14</b>
3.1 Surface Current Lateral Structure: Long-term mean .....	14
3.2 Surface Current Lateral Structure: Wind effects .....	18
3.3 Surface Current Flow Field Lateral Structure: Self-organized Maps .....	23
3.4 Flow Field Vertical Structure.....	27
3.5 The Lagrangian Flow Field.....	36
3.6 Flow Field Case Studies.....	38
<b>4.0 Discussion</b> .....	<b>45</b>
4.1 Flow Field Structure .....	45
4.2 Ecological Importance .....	47
<b>5.0 Conclusions</b> .....	<b>48</b>
5.1 Recommendations.....	48
<b>Acknowledgments</b> .....	<b>49</b>
<b>References</b> .....	<b>50</b>
<b>Appendices</b> .....	<b>52</b>
Appendix A: Mean current speed magnitude by year. ....	52
Appendix B: Mean current variance magnitude by year. ....	53
Appendix C: Surface current composites for the case of weak mean daily wind speed and blowing from each of the four quadrants.....	54
Appendix D: Flow field divergence based on wind speed and direction. ....	56
Appendix E: Flow field relative vorticity based on wind speed and direction.....	57
Appendix F: Self-organized Maps by Year .....	58

**List of Tables**

Table 1: Sample years, dates, and number of days with data in each year..... 5

Table 2: Mooring name, location, water depth, date range of HFR-mooring overlap, and number of hours of overlap between the HFR and mooring time series ..... 10

**List of Figures**

Figure 1: Location map of the Pacific Arctic region with water body and place names. Persistent currents are shown with solid arrows; intermittent or poorly known flows are denoted with dashed arrows. Bering Strait mooring A3 is marked with a yellow star and the CEO mooring site with a blue star. Abbreviation KS denotes Kotzebue Sound. Depth isopleths are contoured with thin black lines at 25, 70, 100, and 200 m. .... 1

Figure 2: Place names map showing the location of Hanna Shoal and Barrow Canyon. Bathymetric shading (colors) denote depths from 0 m (yellow) to 150 m depth (purple); contours are drawn at 20, 40, 60, 80, 100, 200, 1000, and 2000 m depth levels..... 2

Figure 3: Cape Simpson site initial antenna deployment in 2013 (left). Coastal erosion seen at this site in August 2018 (right), where tens of meters of coastline eroded over the course of the prior 5 years. The antenna pictured at left was lost to the sea during the fall of 2017 due to storm-induced erosion..... 3

Figure 4: Daily average surface currents of the western Beaufort Sea on July 23, 2017. Bathymetric contours are shown with gray lines. Current vector orientation denotes the flow direction and color denotes the speed (cm s-1)..... 4

Figure 5: Map showing the location of the HFR installations (stars) and grid points of the final daily averaged dataset (circles) used in this study. Bathymetric shading (colors) denote depths from 0 m (yellow) to 150 m depth (purple); contours are drawn at 20, 40, 60, 80, 100, 200, 1000, and 2000 m depth levels ..... 6

Figure 6: Example spectral returns from the Point Barrow HFR. Left: A correctly defined spectral peak (green) outlined in white. Right: The white outline identifying the spectral peak has truncated two sections of green on the left side of the peak, requiring the need for new spectra defining coefficients..... 7

Figure 7: HFR data coverage, showing the number of valid days of data returns at each grid point in each year ..... 8

Figure 8: Number of days represented by each grid point after quality control, 2013 – 2018..... 9

Figure 9: ADCP mooring locations (red circles) and HFR data locations (small blue dots) showing the proximity of the mooring data to each HFR grid point. Bathymetric shading (background colors) denotes depths from 0 m (yellow) to 200 m depth (purple) ..... 10

Figure 10: The upper panel shows the location of all sub-surface (30 m depth) drogue drifter position fixes (blue circles) in 2013, and the lower panel shows the 2015 dataset. Coincident HFR data points (red crosses) show locations of HFR-drifter data overlap in time..... 11

Figure 11: Daily mean wind speed and direction vectors from the PABR weather station for all days in the analyzed HFR dataset ..... 12

Figure 12: Mean of all daily average HFR current fields over 2013 – 2018. The red vector located at PABR denotes the mean wind over the same 362 days of the HFR record. Color shading depicts bathymetric depths between 0 m (yellow) and 150 m depth (purple).....	14
Figure 13: Mean speed ( $\text{cm s}^{-1}$ ) of the HFR flow field for all 362 days in the record. Bathymetric contours are drawn at 20, 40, 60, 80, 100, 200, 1000, and 2000 m depth levels. ....	15
Figure 14: Variance ( $\text{cm}^2 \text{s}^{-2}$ ) of the HFR flow field for all 362 days in the record. Bathymetric contours are drawn at 20, 40, 60, 80, 100, 200, 1000, and 2000 m depth levels. ....	16
Figure 15: Ellipses showing the orientation, magnitude, and eccentricity along and across the principal axis of variation. ....	16
Figure 16: Divergence ( $\text{cm s}^{-1} \text{km}^{-1}$ ) of the mean HFR flow field shown in Figure 12, excluding the outer grid points with fewer data. Blue colors denote convergence and red colors denote divergence. ....	17
Figure 17: Vorticity Rossby number (dimensionless) of the mean HFR flow field shown in Figure 12, excluding the outer grid points with fewer data .....	17
Figure 18: Mean surface current (blue) and wind (red) vectors for the case of strong (daily average $> 6 \text{ m s}^{-1}$ ) winds blowing to the SW. N denotes the number of days of data that comprise this composite.....	18
Figure 19: Mean surface current (blue) and wind (red) vectors for the case of strong (daily average $> 6 \text{ m s}^{-1}$ ) winds blowing to the SE. N denotes the number of days of data that comprise this composite.....	19
Figure 20: Mean surface current (blue) and wind (red) vectors for the case of strong (daily average $> 6 \text{ m s}^{-1}$ ) winds blowing to the NW. N denotes the number of days of data that comprise this composite.....	20
Figure 21: Mean surface current (blue) and wind (red) vectors for the case of strong (daily average $> 6 \text{ m s}^{-1}$ ) winds blowing to the NE. N denotes the number of days of data that comprise this composite.....	21
Figure 22: Top panel: Mean surface current (blue) and wind (red) vectors for the case of weak (daily average $< 4 \text{ m s}^{-1}$ ) winds blowing from all directions. N denotes the number of days of data that comprise this composite. Bottom left panel: Vorticity Rossby number of the current vector map at top. Bottom right panel: Divergence ( $\text{cm s}^{-1} \text{km}^{-1}$ ) of the current vector map at top. Blue colors denote convergence and red colors denote divergence .....	22
Figure 23: Self-organized map (SOM) patterns 1 (top) and 2 (bottom), shown with the percentage of all daily mean HFR maps that comprise this composite. The black vector at Utqiagvik denotes the wind speed and direction for the days that correspond to the depicted SOM patterns. ....	24
Figure 24: Self-organized map (SOM) patterns 3 (top) and 4 (bottom), shown with the percentage of all daily mean HFR maps that comprise this composite. The black vector at Utqiagvik denotes the wind speed and direction for the days that correspond to the depicted SOM patterns. ....	25

Figure 25: Self-organized map (SOM) patterns 5 (top) and 6 (bottom), shown with the percentage of all daily mean HFR maps that comprise this composite. The black vector at Utqiaġvik denotes the wind speed and direction for the days that correspond to the depicted SOM patterns. .... 26

Figure 26: Comparison of east-west (U, top panel) and north-south (V, bottom panel) currents collected at mooring site BC2 for all hours of ADCP and HFR data record overlap at this site. Red traces show the vertically-averaged ADCP data; blue traces show the surface HFR data. The hourly data shown in this plot were collected over the course of five years and are displayed chronologically on the horizontal axis as consecutive observation number. .... 27

Figure 27: Mean PABR wind (black), HFR surface current (blue), and ADCP subsurface current (red) velocity vectors at all mooring sites. The vectors at each mooring site are averaged over the full period of HFR/ADCP record overlap for that installation..... 28

Figure 28: Near-surface vertical current shear (vertical axes) based on wind component magnitude (horizontal axes) at the 17 mooring sites. East-west wind and shear components are plotted with blue and the north-south wind and shear components are plotted in red..... 29

Figure 29: Upper ocean shear response based on wind velocity components, where the data is binned for wind component magnitudes between  $-20$  and  $+20 \text{ m s}^{-1}$ . The response to zonal wind is shown for the zonal shear (red stars) and meridional shear (blue stars). The response to meridional winds is shown for the zonal shear (blue circles) and meridional shear (red circles). Note difference in scale across all subplot vertical axes..... 29

Figure 30: Mooring BC2 vertical shear in speed (left) and direction (right) from surface (HFR) and subsurface (ADCP) data based on the four wind speed (WS) and direction criteria shown in the legend. The wind component,  $U_w$ , represents the component aligned with the principal axis of variation ..... 30

Figure 31: Mooring BC6 vertical shear in speed (left) and direction (right) from surface (HFR) and subsurface (ADCP) data based on the four wind speed (WS) and direction criteria shown in the legend. The wind component,  $U_w$ , represents the component aligned with the principal axis of variation ..... 31

Figure 32: Mooring SBN vertical shear in speed (left) and direction (right) from surface (HFR) and subsurface (ADCP) data based on the four wind speed (WS) and direction criteria shown in the legend. The wind component,  $U_w$ , represents the component aligned with the principal axis of variation ..... 32

Figure 33: Mooring HSNE50 vertical shear in speed (left) and direction (right) from surface (HFR) and subsurface (ADCP) data based on the four wind speed (WS) and direction criteria shown in the legend. The wind component,  $U_w$ , represents the component aligned with the principal axis of variation. .... 33

Figure 34: Water speed shear profiles at mooring BC2 under conditions of the angle between the winds and the surface currents as noted in the color legend: blue =  $0 \ll 90$ ; red =  $-90 \ll 0$ ; cyan =  $90 \ll 180$ ; magenta =  $-180 \ll -90$ . Upper left panel shows the shear profiles for wind speed  $\leq 6 \text{ m s}^{-1}$  and  $U_w < 0$ ; upper right panel shows the shear profiles for wind speed  $> 6 \text{ m s}^{-1}$  and  $U_w < 0$ ; lower left panel shows the shear profiles for wind speed  $\leq 6 \text{ m s}^{-1}$  and  $U_w > 0$ ; lower right panel shows the shear profiles for wind speed  $> 6 \text{ m s}^{-1}$  and  $U_w > 0$  ..... 34

Figure 35: Profiles of water column shear separated by the sign of the near-surface shear, based on the slope of the shear profile between the HFR data at the surface and the first good ADCP data point below the surface. The profiles are shown with negative (blue) and positive (red) shear profiles. Each panel is labeled with the mooring site name and the percentage of time that the site experienced each near-surface shear condition. Only moorings with full resolution 1 m vertical bin spacing are shown here ..... 35

Figure 36: Mean vertical profile of current speeds (solid lines) across all moorings based on positive (red) and negative (blue) shears between the surface HFR current and the closest-to-surface ADCP current. On either side of the mean profiles, 95% confidence limits are shown with dashed lines Based on the profiles shown in Figure 35 ..... 35

Figure 37: Comparison of data from Drifter 122541 and the HFR. The upper left and upper right panels show the U and V velocity components, respectively, with blue lines showing the drifter data and red dots showing the coincident HFR data. The lower left panel shows the scatter between the drifter and HFR data for the U (blue) and V (red) components. The lower right panel is a map showing the drifter location (blue symbols) and the location of coincident HFR data (red symbols)..... 36

Figure 38: Time series of U (upper panel) and V (lower panel) components of the currents (drifter = blue, HFR = red) and PABR winds (black, scaled by a factor of 10). All data from the 2013 drifter deployments are plotted here. .... 37

Figure 39: Scatterplot of all 1,279 drifter-HFR data pairs from the 2013 and the 2015 30 m depth drogued drifters ..... 37

Figure 40: One-day average flow field maps of the currents (left), relative vorticity (upper right), and divergence fields (lower right). The three wind vectors shown at Utqiaġvik display the mean daily wind vector for the displayed date (red), the prior day (black), and two days prior (blue) ..... 39

Figure 41: One-day average flow field maps of the currents (left), relative vorticity (upper right), and divergence fields (lower right). The three wind vectors shown at Utqiaġvik display the mean daily wind vector for the displayed date (red), the prior day (black), and two days prior (blue) ..... 40

Figure 42: One-day average flow field maps of the currents (left), relative vorticity (upper right), and divergence fields (lower right). The three wind vectors shown at Utqiaġvik display the mean daily wind vector for the displayed date (red), the prior day (black), and two days prior (blue) ..... 40

Figure 43: One-day average flow field maps of the currents (left), relative vorticity (upper right), and divergence fields (lower right). The three wind vectors shown at Utqiaġvik display the mean daily wind vector for the displayed date (red), the prior day (black), and two days prior (blue) ..... 41

Figure 44: One-day average flow field maps of the currents (left), relative vorticity (upper right), and divergence fields (lower right). The three wind vectors shown at Utqiaġvik display the mean daily wind vector for the displayed date (red), the prior day (black), and two days prior (blue) ..... 41

Figure 45: One-day average flow field maps of the currents (left), relative vorticity (upper right), and divergence fields (lower right). The three wind vectors shown at Utqiaġvik display the mean daily wind vector for the displayed date (red), the prior day (black), and two days prior (blue) ..... 42

Figure 46: One-day average flow field maps of the currents (left), relative vorticity (upper right), and divergence fields (lower right). The three wind vectors shown at Utqiaġvik display the mean daily wind vector for the displayed date (red), the prior day (black), and two days prior (blue) ..... 42

Figure 47: One-day average flow field maps of the currents (left), relative vorticity (upper right), and divergence fields (lower right). The three wind vectors shown at Utqiaġvik display the mean daily wind vector for the displayed date (red), the prior day (black), and two days prior (blue) ..... 43

Figure 48: One-day average flow field maps of the currents (left), relative vorticity (upper right), and divergence fields (lower right). The three wind vectors shown at Utqiaġvik display the mean daily wind vector for the displayed date (red), the prior day (black), and two days prior (blue) ..... 43

Figure 49: One-day average flow field maps of the currents (left), relative vorticity (upper right), and divergence fields (lower right). The three wind vectors shown at Utqiaġvik display the mean daily wind vector for the displayed date (red), the prior day (black), and two days prior (blue) ..... 44

Figure 50: Map depicting an idealized rendering of the typical surface currents in the study region. .... 47

**List of Appendix Figures**

Figure A1: Mean current speeds ( $\text{cm s}^{-1}$ ) of the HFR flow field by year. Bathymetric contours are drawn at 20, 40, 60, 80, 100, 200, 1000, and 2000 m depth levels..... 52

Figure B1: Mean variance ( $\text{cm}^2 \text{s}^{-2}$ ) of the HFR flow field by year ..... 53

Figure C1: Average surface current vectors for wind speed  $< 4 \text{ m s}^{-1}$ ,  $U < 0$ , and  $V < 0$ . ..... 54

Figure C2: Average surface current vectors for wind speed  $< 4 \text{ m s}^{-1}$ ,  $U > 0$ , and  $V < 0$ . ..... 54

Figure C3: Average surface current vectors for wind speed  $< 4 \text{ m s}^{-1}$ ,  $U < 0$  and  $V > 0$ . ..... 55

Figure C4: Average surface current vectors for wind speed  $< 4 \text{ m s}^{-1}$ ,  $U < 0$  and  $V > 0$ . ..... 55

Figure D1: Divergence ( $\text{cm s}^{-1} \text{ km}^{-1}$ ) composites based on wind speed and direction..... 56

Figure D2: Divergence ( $\text{cm s}^{-1} \text{ km}^{-1}$ ) composites based on wind speed and direction..... 56

Figure E1: Relative vorticity composites based on wind speed and direction ..... 57

Figure E2: Relative vorticity composites based on wind speed and direction ..... 57

Figure F1: Self-organized map (SOM) patterns 1 (top) and 2 (bottom) for all daily HFR mean maps from 2013. .... 58

Figure F2: Self-organized map (SOM) patterns 3 (top) and 4 (bottom) for all daily HFR mean maps from 2013. .... 59

Figure F3: Self-organized map (SOM) patterns 5 (top) and 6 (bottom) for all daily HFR mean maps from 2013. .... 60

Figure F4: Self-organized map (SOM) patterns 1 (top) and 2 (bottom) for all daily HFR mean maps from 2014. .... 61

Figure F5: Self-organized map (SOM) patterns 3 (top) and 4 (bottom) for all daily HFR mean maps from 2014. .... 62

Figure F6: Self-organized map (SOM) patterns 5 (top) and 6 (bottom) for all daily HFR mean maps from 2014. .... 63

Figure F7: Self-organized map (SOM) patterns 1 (top) and 2 (bottom) for all daily HFR mean maps from 2015. .... 64

Figure F8: Self-organized map (SOM) patterns 3 (top) and 4 (bottom) for all daily HFR mean maps from 2015. .... 65

Figure F9: Self-organized map (SOM) patterns 5 (top) and 6 (bottom) for all daily HFR mean maps from 2015. .... 66

Figure F10: Self-organized map (SOM) patterns 1 (top) and 2 (bottom) for all daily HFR mean maps from 2016. .... 67

Figure F11: Self-organized map (SOM) patterns 3 (top) and 4 (bottom) for all daily HFR mean maps from 2016. .... 68

Figure F12: Self-organized map (SOM) patterns 5 (top) and 6 (bottom) for all daily HFR mean maps from 2016. .... 69

Figure F13: Self-organized map (SOM) patterns 1 (top) and 2 (bottom) for all daily HFR mean maps from 2017. .... 70

Figure F14: Self-organized map (SOM) patterns 3 (top) and 4 (bottom) for all daily HFR mean maps from 2017. .... 71

Figure F15: Self-organized map (SOM) patterns 5 (top) and 6 (bottom) for all daily HFR mean maps from 2017. .... 72

Figure F16: Self-organized map (SOM) patterns 1 (top) and 2 (bottom) for all daily HFR mean maps from 2018. .... 73

Figure F17: Self-organized map (SOM) patterns 3 (top) and 4 (bottom) for all daily HFR mean maps from 2018. .... 74

Figure F18: Self-organized map (SOM) patterns 5 (top) and 6 (bottom) for all daily HFR mean maps from 2018. .... 75

## Executive Summary

We process and analyze six years (2013 – 2018) of high-frequency radar (HFR) data from the western Beaufort and northeastern Chukchi Seas. Based on local wind speed and direction, composite averages of the flow field reveal a system of surface current regimes that dominate the synoptic-scale variability. Our analyses allow us to develop an updated map of the mean July – October surface flow field based on 362 days of processed HFR data.

The spatially high-resolution HFR dataset provides insights into the lateral structure of the flow field, some aspects of which have not been previously described in the scientific literature. These include maps of the vorticity and divergence fields (1) for the mean state, (2) as a function of wind speed and direction, and (3) for select 1-day snapshots in time. We identify key locations where the shape of the coastline and seafloor bathymetry, in conjunction with winds, exert strong control over the flow field. These include the eastern edge of Barrow Canyon where the coastal flow in the western Beaufort Sea converges with the along-canyon flow of the Alaska Coastal Current; the head of Barrow Canyon; the eastern side of the mouth of Barrow Canyon; and a small un-named canyon near 153°W in the western Beaufort Sea.

A recurrent gyre in the western Beaufort Sea straddles the shelf and slope region, normally rotating in an anticyclonic (clockwise) fashion. The gyre, which emerges even in the long-term mean flow field, tends to occur under the influence of the prevailing winds that blow to the southwest. Winds that blow to the northeast occasionally reverse the orientation of the gyre, causing cyclonic (counterclockwise) rotation. The gyre tends to decay when wind forcing is absent or weak.

Maps of the surface flow field vorticity and divergence fields provide indications of the dynamics that control the circulation. Features of note include convergent flow near the head of Barrow Canyon (near Wainwright), near the confluence of the U.S. Chukchi and Beaufort Seas (near Utqiagvik), and near the mouth of Barrow Canyon. In the mean, the flow field exhibits positive vorticity through most of the length of Barrow Canyon (as the water depths increase downstream) but turns negative at the mouth of Barrow Canyon and to the east, along the western Beaufort Sea slope, and then following the gyre circulation toward shore and back to Barrow Canyon along the Beaufort coast. The transition between sense of rotation occurs at the northernmost extent of the western Beaufort shelf, where the bathymetric contours transition from southwest-northwest to northwest-southeast orientations.

Oceanographic moorings within the HFR data mask provide vertical profile estimates of subsurface currents, and these are analyzed in conjunction with the HFR data to assess velocity shears in the upper 10 m of the water column. We find that, while the HFR-based currents have great similarity to the barotropic (water column average) flow, there exists appreciable shear in speed and/or direction. The shears are, in part, a function of the relative orientation between the surface wind and the underlying currents.

The complexity of the flow field in this region reduces the accuracy of simple wind speed/direction-based estimates of surface drift. The results of this study can be applied to improve oil spill trajectory calculations.

## 1.0 Introduction

Understanding the circulation on Alaska's Arctic continental shelves (Figure 1) is important to the application of National Environmental Policy Act (NEPA) requirements in the permitting and oversight process of offshore activities associated with the oil and gas industry. Previous support from the Bureau of Ocean Energy Management (BOEM), Shell Oil, the Alaska Ocean Observing System (AOOS), ConocoPhillips Alaska, the National Center for Island Maritime and Extreme Environment Security (CIMES), the State of Alaska Coastal Impact Assistance Program (CIAP), and the North Slope Borough has supported the collection of a unique open water season surface current velocity dataset that covers the western Beaufort and northeastern Chukchi Seas. Data coverage extends from the coastal zone to beyond the U.S. Beaufort/Chukchi shelf break, including Barrow Canyon's intersection with the continental slope from 2013 to 2018.

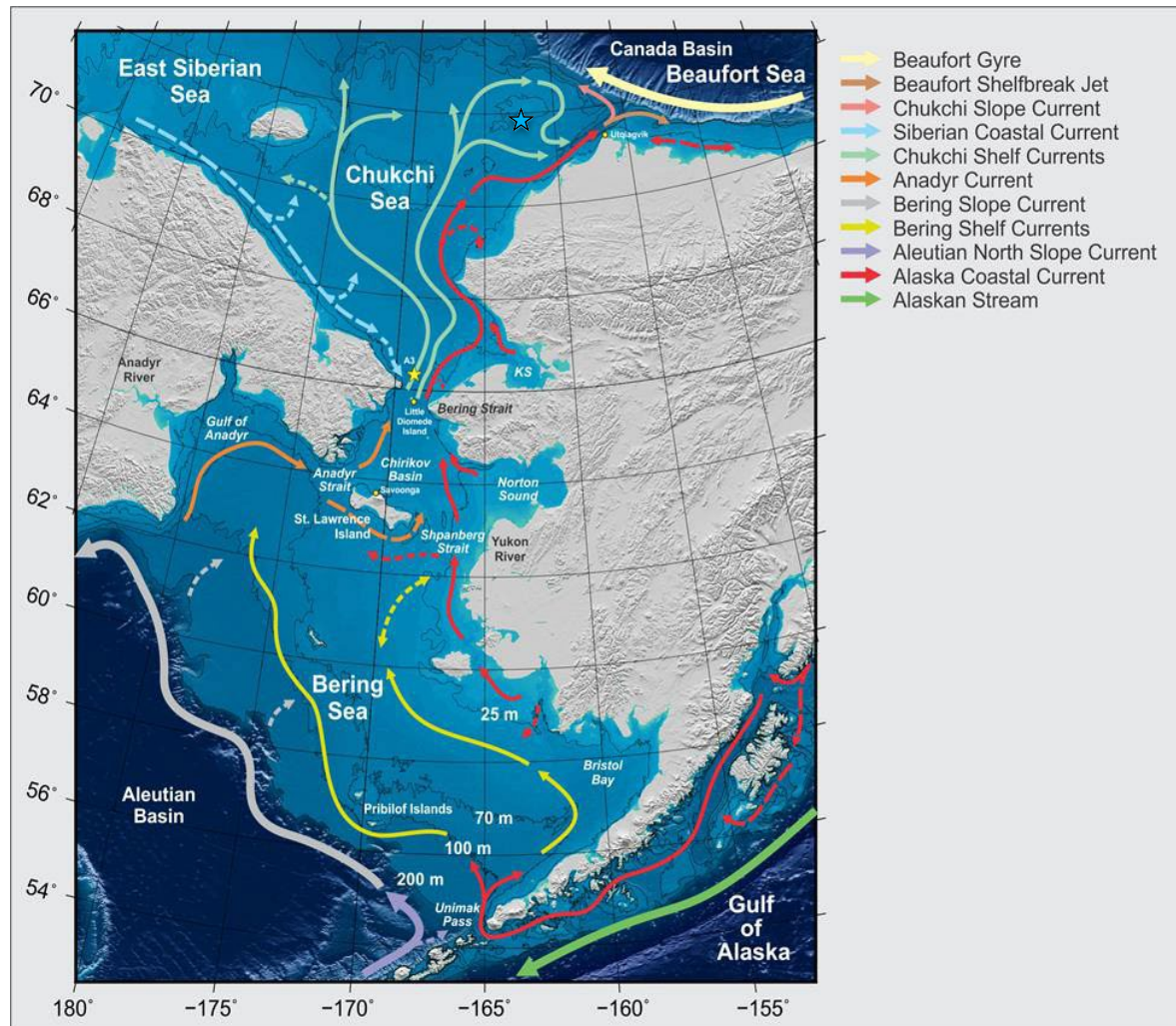


Figure 1: Location map of the Pacific Arctic region with water body and place names. Persistent currents are shown with solid arrows; intermittent or poorly known flows are denoted with dashed arrows. Bering Strait mooring A3 is marked with a yellow star and the CEO mooring site with a blue star. Abbreviation KS denotes Kotzebue Sound. Depth isopleths are contoured with thin black lines at 25, 70, 100, and 200 m. Reprinted from Danielson et al. (2020).

In this study, six years of high-frequency radar (HFR) data from the western Beaufort and northeastern Chukchi Seas (Figure 2) is processed and analyzed in conjunction with other in situ ocean current data and observed winds. We evaluate the relationship between surface currents measured by the HFR systems and subsurface currents measured by seasonal and year-round oceanographic moorings, as well as the relationship between the wind and the surface flow field structure and evolution and satellite-tracked drifters. This study provides an updated scientific understanding of the surface circulation (1) in the northeastern Chukchi Sea near Hanna Shoal and Barrow Canyon, (2) in the western Beaufort Sea from Point Barrow to Smith Bay, and (3) for surface-to-subsurface relationships in flow throughout the study region.

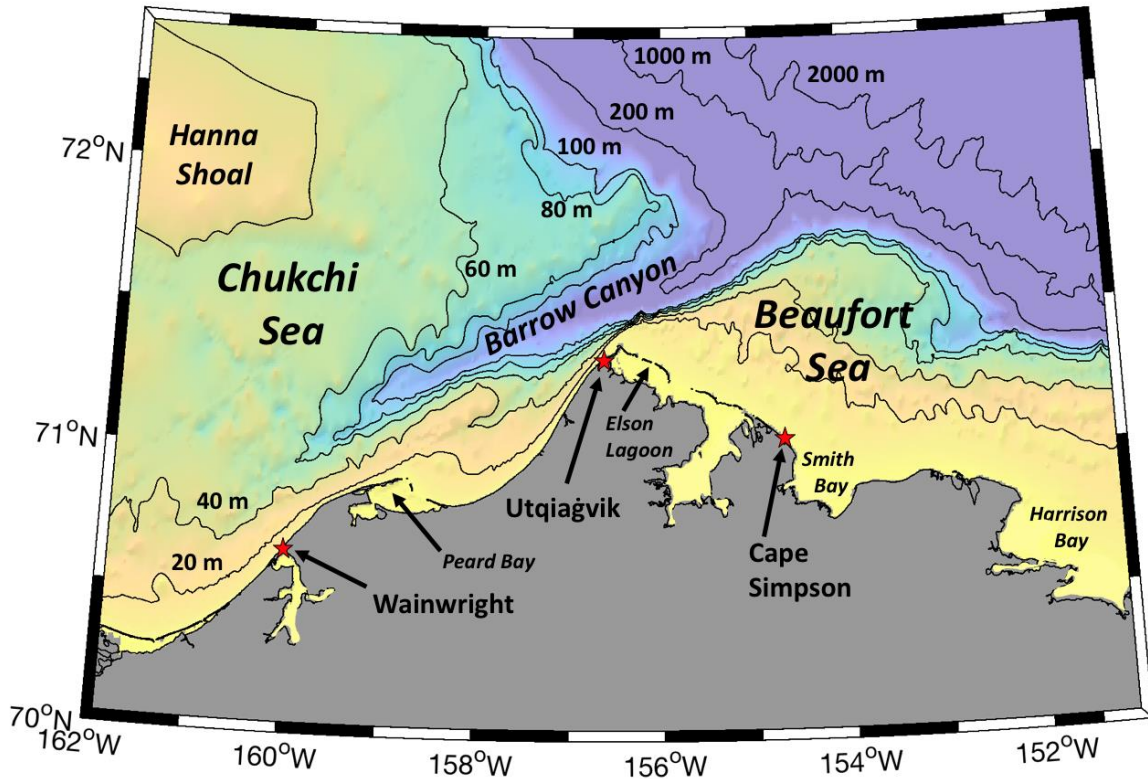


Figure 2: Place names map showing the location of Hanna Shoal and Barrow Canyon. Bathymetric shading (colors) denotes depths from 0 m (yellow) to 150 m depth (purple); contours are drawn at 20, 40, 60, 80, 100, 200, 1000, and 2000 m depth levels.

The first measurements of surface currents using HFR in the western Beaufort Sea were made by the University of Alaska Fairbanks (UAF) beginning September 2013 and have continued to present during open water seasons. Though initially part of a BOEM supported study (Weingartner, et al., 2017a), since June 2015 HFR surface current data has been collected in the U.S. Chukchi and Beaufort Seas with funding from the AOOS, North Slope Borough, and Shell Oil purely for operational applications and without funding for quality control, analysis, or academic publication.

Improving our knowledge of the regional circulation is directly related to identifying the potential effects of offshore exploration and development. The results can help improve existing oil spill trajectory models, oil spill risk assessment, and emergency response planning (Danielson and Weingartner, 2007). Identifying areas where convergence and recirculation are found provides valuable environmental cues

for the entire ecosystem. For example, Okkonen et al. (2009) found that whales are often seen near frontal formations on the western Beaufort shelf during weak winds. Mapping circulation features derived from the surface current data could be used in conjunction with results from a number of ecological studies including BOEM's Aerial Surveys of Arctic Marine Mammals project; the NSF-funded Arctic Winds, Fish, Fins and Feathers project; the NSF-funded Beaufort Lagoons Long-Term Ecological Research program; and the Collaborative Alaskan Arctic Studies Program (CAASP; formerly the North Slope Borough Shell Baseline Studies Program) study of forage fish in Arctic lagoons.

The Beaufort coast is a region of high coastal erosion (Figure 3). Recent data have shown that, on a decadal scale, the rate of erosion on the Beaufort coast is ~2.5 times higher than it has been in the past, with Drew Point now losing ~17.2 m yr<sup>-1</sup> (Jones et al., 2018). Our surface current mapping field site installed 70 m from the shoreline at Cape Simpson in 2013 had to be moved back from the beach in 2018 to save equipment from being washed into the Arctic Ocean. The fate of the sediment being released into coastal waters by erosion is a factor for offshore drilling structures and pipelines and could change navigation pathways, impact biological habitat, and alter the availability of carbon in the biological system. Additionally, recent years have seen longer periods of open water due to record low sea ice cover. These changes directly affect the livelihood of local communities and their relationship with the marine environment and could potentially cause changes in marine mammal and seabird behavior. Hence, during a time of environmental change, this study's findings will help inform BOEM NEPA documentation.



Figure 3: Cape Simpson site initial antenna deployment in 2013 (left) and coastal erosion seen at the site in August 2018 (right). Tens of meters of coastline eroded during the prior 5 years. The antenna pictured at left was lost to the sea during the fall of 2017 due to storm-induced erosion.

Past measurements of surface currents using HFR and satellite-tracked drifters in the western Beaufort Sea have captured a complex circulation field. Weingartner et al. (2017a and 2017b) reported briefly on 2013 western Beaufort Sea surface currents finding mean westward flow nearshore, except nearshore surface flow was generally eastward when winds were from the southwest. Westward currents near the Beaufort coast often converge with northeastward currents flowing past Point Barrow (Figure 4), and recirculation features north-northeast of Cape Simpson were commonly noted in the real-time data. Improving characterization of the flow provides information to support search and rescue efforts and marine forecasting and navigation and will advance our understanding of the dispersal of ocean-borne

contaminants (e.g., oil spills in the coastal areas of the U.S. Chukchi and Beaufort Seas) and other processes that are important to the climate and dynamics of the Arctic Ocean.

Vertical shear is an important characteristic of the flow field that can affect the fate of oil and other ocean-borne contaminants, and its presence can confound the interpretation of surface motions relative to subsurface mooring-based measurements. The presence of vertical shear of the horizontal velocity field is well known but is not well described in the study region. Acoustic doppler current profilers (ADCPs) collect data in depth-binned increments through the water column but struggle with accuracy in the uppermost 5 m of the water column due to waves and sidelobe contamination from the reflection surface. The vertical shear in the water column in the northeastern Chukchi and western Beaufort Seas may be prone to complex behaviors due to the influence of total water depth relative to the surface and seafloor Ekman layers; stratification (including the variable presence of sea ice melt and the Alaskan Coastal Current); and setup of the large-scale pressure gradient, bathymetric steering, and direction and strength of the wind relative to the other factors. Hence, we undertake a combined analysis of the subsurface ADCP flow field in conjunction with the surface flow field as resolved by the HFR network.

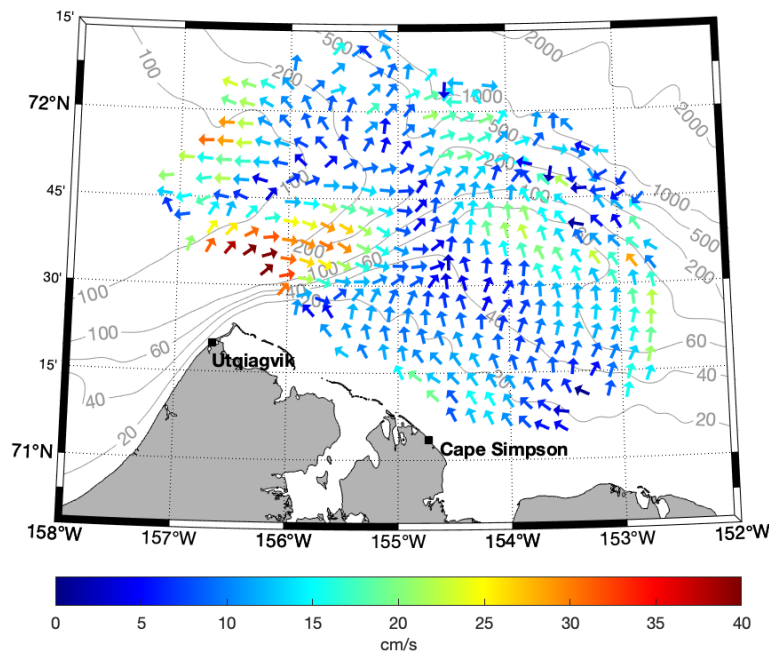


Figure 4: Daily average surface currents of the western Beaufort Sea on July 23, 2017. Bathymetric contours are shown with gray lines. Current vector orientation denotes the flow direction and color denotes the speed ( $\text{cm s}^{-1}$ ).

We note that the Chukchi Ecosystem Observatory (CEO) mooring site deployed in 2014 (Figure 1) is one of the few year-round long-term monitoring stations in the Pacific Arctic region and the only one that strives to measure physics along with nutrient and carbon chemistry, particles, zooplankton, fish, and marine mammals (Danielson et al., 2017a; Hauri et al., 2018; Lalande et al., 2021). The present study helps us characterize the flow field in the vicinity of the CEO and places this monitoring focal point in a regional spatial context. The CEO mooring data provides continuity between the U.S. Chukchi oil exploration years of 2008 – 2015 and the years following, after Shell Oil exited from the region.

This study examines the relationship between regional winds and the circulation patterns that develop over the western Beaufort Sea and the northeastern Chukchi Sea. To classify surface circulation and its relationship to subsurface shear, we (1) process and quality control surface current data, (2) examine the relationships between the regional winds and the circulation patterns in the study region, and (3) compare surface current estimates with moored ADCP measurements to derive the relationship of surface waters to those at depth. Section 2 describes the datasets used and their handling, Section 3 presents the results of the analyses, Section 4 provides discussion, and Section 5 offers conclusions and recommendations.

## 2.0 Methods

In this section, we describe the HFR data processing and the final dataset’s spatial and temporal coverage as well as the quality assurance steps taken to obtain a self-consistent dataset that is free of bias between days and between years of sampling. We also introduce the ADCP and satellite-tracked drifter datasets and the meteorological data and briefly review our approach to data analysis.

### 2.1 High-Frequency Radar Data

Hourly surface currents were measured using HFR systems manufactured by CODAR Ocean Sensors. Utilizing 5 MHz as the operating frequency, one-dimensional currents are obtained up to ~180 km offshore from each field site and combined to create two-dimensional currents on a 6 km grid. In this analysis, we focus on the data collected by HFR systems located in Wainwright, Point Barrow (~10 miles northeast of Utqiagvik), and Cape Simpson during the 2013 – 2018 open water seasons (Table 1). Data coverage varied in spatial and temporal extent from year to year, with a range of 58 to 64 days sampled each year.

Table 1: Sample years, dates, and number of days with data in each year.

Year	First day of data in both mask clusters	Last day of data in both mask clusters	# of days with data
2013	30 August	28 October	60
2014	20 August	18 October	60
2015	22 August	24 October	64
2016	27 August	23 October	58
2017	21 July	19 September	61
2018	29 August	26 October	59

The three stations produced data in two clusters, or data masks (Figure 5). The first cluster, sampled by sites in Wainwright and Point Barrow, is fully in the northeastern Chukchi Sea. Its northern edge extends from Hanna Shoal to the upper half of Barrow Canyon in the east and just west of Wainwright along the western edge of the data mask. The second cluster, sampled by sites at Point Barrow and Cape Simpson, covers the lower (eastern) half of Barrow Canyon and the western Beaufort Sea, encompassing grid points that include both the shelf and upper continental slope.

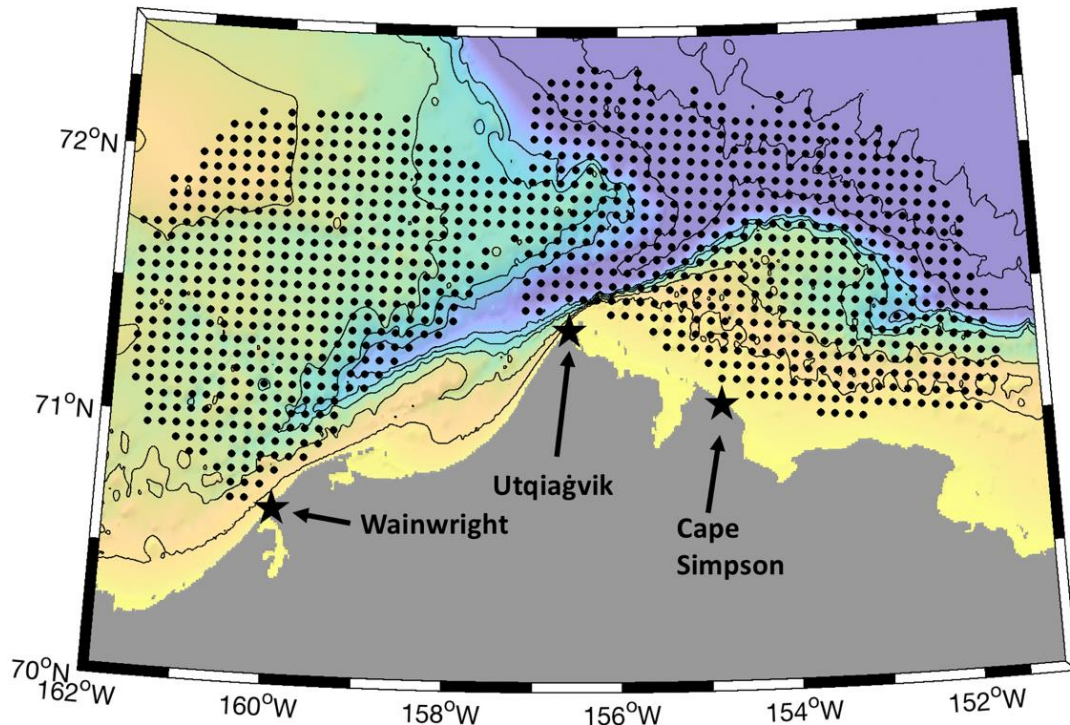


Figure 5: Map showing the location of the HFR installations (stars) and grid points of the final daily averaged dataset (circles) used in this study. Bathymetric shading (colors) denotes depths from 0 m (yellow) to 150 m depth (purple); contours are drawn at 20, 40, 60, 80, 100, 200, 1000, and 2000 m depth levels.

The HFR systems measure the radio wave backscatter off 30 m wavelength ocean waves using the reflected Doppler spectra (Barrick et al., 1985). Each HFR site was calibrated for background spectral noise that could cause signal interference (Barrick and Lipa, 1986). Since ocean waves are required for operation, and the radar signal does not propagate over land or ice, the resulting extent of spatial coverage is variable and limited to periods of open water. Ionospheric interference is another limitation; nightly reflections of the transmitted 5 MHz signal by the ionosphere lower the signal-to-noise ratio > 90 km offshore, resulting in reduced data coverage (Teague, 2001).

A spectral file of the backscatter contains the Bragg shift, which increases with faster currents. These real-time backscattered spectra were subjected to visual inspection to ensure the optimal processing parameters and reprocessed to obtain the most accurate current measurements. The presence of sea ice, intense fall storms, and the strong Alaska Coastal Current (ACC) offshore of Wainwright often split the spectral signal into multiple peaks, overwhelming the default parameters used to derive the current velocities and resulting in truncated current speeds and data gaps. To correct for these discrepancies, spectral peak-finding settings were optimized for the local environment, a labor-intensive effort of optimizing the smoothing value and power range in which to look for the surface current signal (Figure 6). A persistent data gap north of Point Barrow, caused by the distance the radar signal had to cross to reach the water, required similar fixes to the spectra definition.

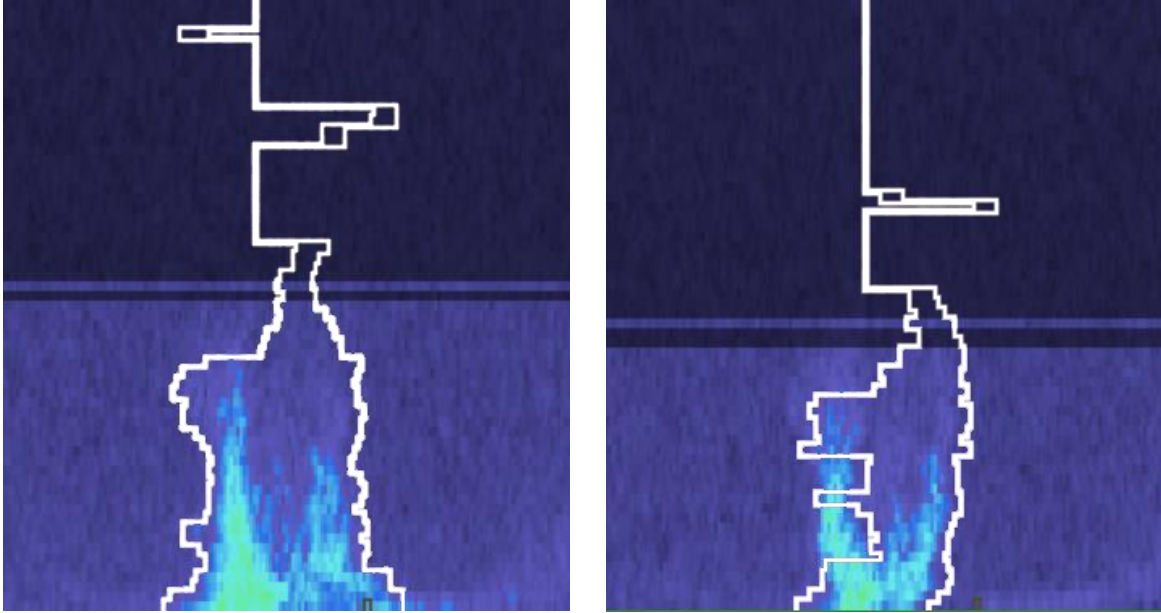


Figure 6: Example spectral returns from the Point Barrow HFR. Left: A correctly defined spectral peak (green) outlined in white. Right: The white outline identifying the spectral peak has truncated two sections of green on the left side of the peak, requiring the need for new spectra defining coefficients.

After the new parameters were defined and the time periods they applied to in the dataset were identified, the spectra were reprocessed into one-dimensional velocities. One-dimensional velocities greater than three standard deviations from the temporal mean of each grid point were removed. Using a 9 km averaging radius around each grid point, the one-dimensional velocities were then used to calculate the two-dimensional surface current. Grid points with less than 60% hourly temporal coverage for each year were flagged and removed, as were velocities greater than 200 cm/s and those with a geometric dilution of precision (GDOP) > 1.25.

The spatial extent and number of samples per grid point (Figures 7 and 8) provide a means for assessing the representativeness of some of the data comparisons in this report. Regions with fewer data points (typically at the edges of the good data coverage regions) commonly have a higher GDOP and/or a lower signal-to-noise ratio, commensurate with a decrease in data quality. For example, coverage in 2017 extended slightly farther across the continental slope than coverage in the other years and the data shown in this region are necessarily biased to the year 2017. The total number of days sampled at each grid point is shown in Figure 8; sample days ranged from 7 to 351 (362 days total are represented in the dataset), with a mean of 208 and a median of 234.

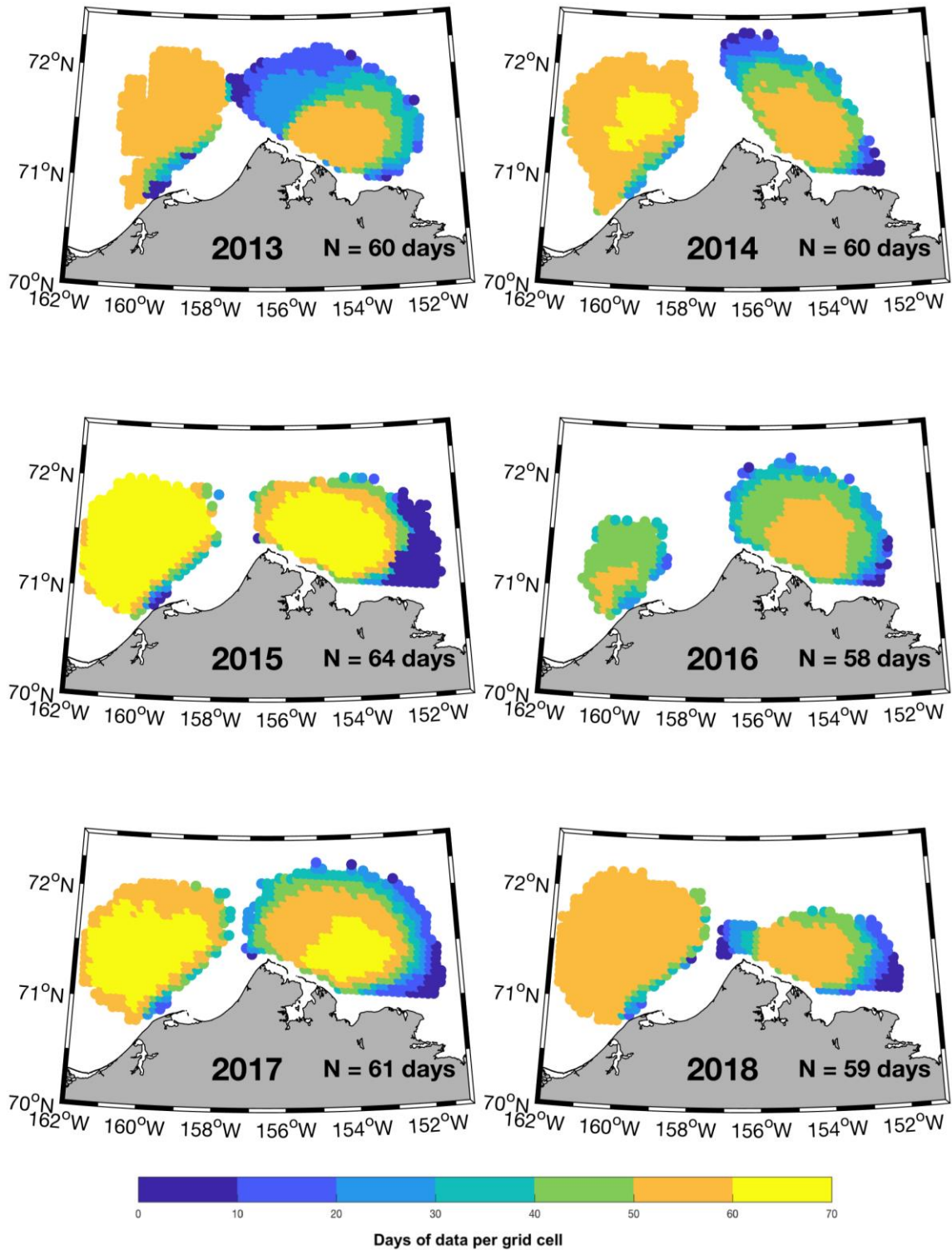


Figure 7: HFR data coverage showing the number of valid days of data returns at each grid point in each year.

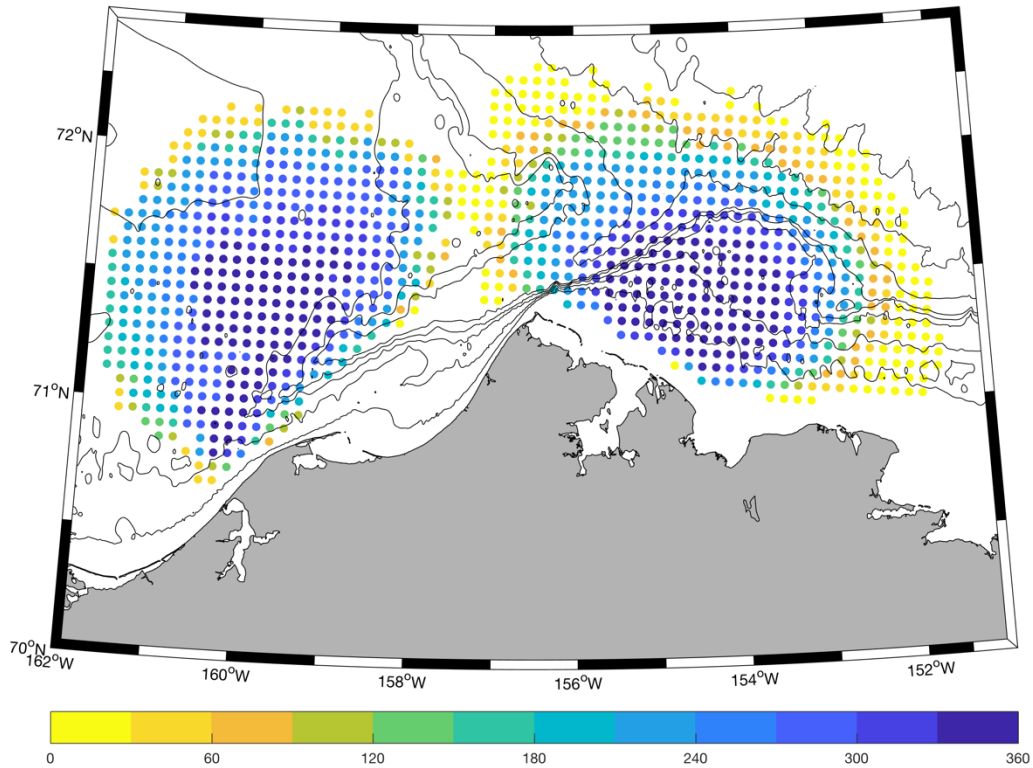


Figure 8: Number of days represented by each grid point after quality control, 2013 – 2018.

## 2.2 Moored Acoustic Doppler Current Profiler Data

Funded by BOEM, industry, the State of Alaska CIAP, North Pacific Research Board, and CAASP (Weingartner et al., 2017a; Stabeno et al., 2018; Vollenweider et al. 2018; Danielson et al., 2017b), year-round and summer-only moorings with ADCPs have been deployed at a few dozen sites across the U.S. Chukchi and Beaufort Seas. Many of these deployments took place between 2009 – 2012, before the installation of the Cape Simpson HFR expanded surface current coverage west of Point Barrow in 2013.

To examine connections between the northeastern Chukchi and western Beaufort, our primary study focus is on the years 2013 – 2018, but we have HFR data for 2009 – 2016 that covered the northeastern Chukchi Sea from south and west of Wainwright to north and west of Point Barrow. We utilized this extended area in space and time to maximize the number of HFR-ADCP data pairs for comparison (Figure 9).

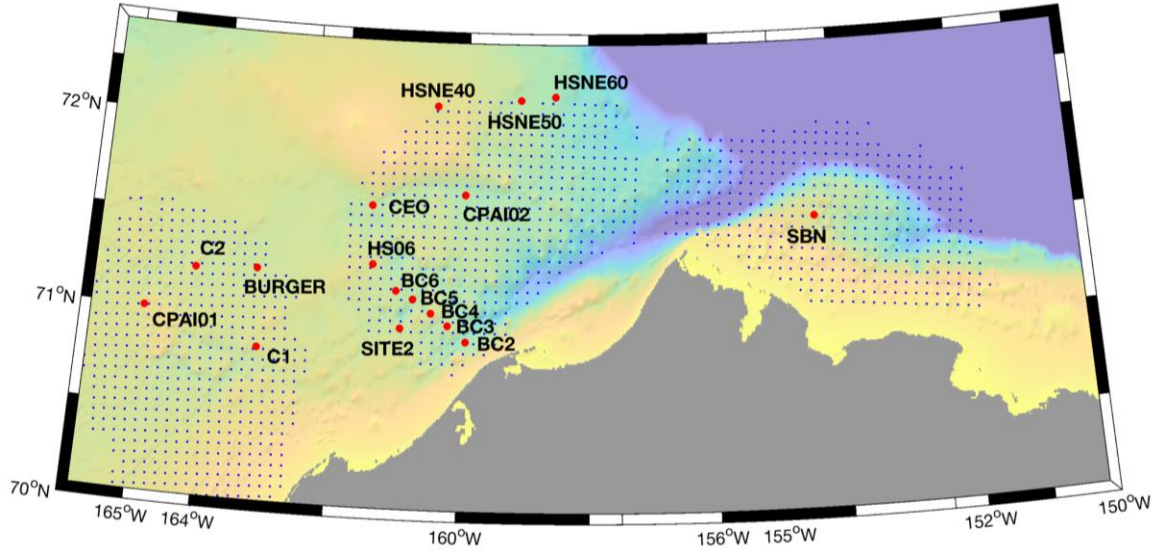


Figure 9: ADCP mooring locations (red circles) and HFR data locations (small blue dots) showing the proximity of the mooring data to each HFR grid point. Bathymetric shading (background colors) denotes depths from 0 m (yellow) to 200 m depth (purple).

Table 2: Mooring name, location, water depth, date range of HFR-mooring overlap, number of hours (N) of overlap between the HFR and mooring time series, and distance between the mooring site and Utqiagvik airport (km). Dates and times are given in Universal Time Coordinated (UTC).

Mooring Name	Longitude (°W)	Latitude (°N)	Start Date and Time (UTC)	End Date and Time (UTC)	N	Distance (km)
BC2	-159.9400	70.9200	17-Aug-2010 12:00:00	19-Oct-2014 09:00:00	9777	121
BC3	-160.2300	71.0000	17-Aug-2010 12:00:00	12-Nov-2011 23:00:00	4728	128
BC4	-160.4950	71.0600	17-Aug-2010 12:00:00	13-Nov-2011 00:00:00	4637	135
BC5	-160.7900	71.1300	17-Aug-2010 12:00:00	13-Nov-2011 00:00:00	4619	144
BC6	-161.0600	71.1700	18-Aug-2010 12:00:00	01-Nov-2011 06:00:00	4307	154
CEO	-161.5000	71.6000	21-Sep-2014 13:00:00	29-Nov-2017 08:00:00	6364	171
HSNE40	-160.5000	72.1200	24-Aug-2012 21:00:00	19-Sep-2014 11:00:00	3724	160
HSNE50	-159.1200	72.1600	25-Aug-2012 19:00:00	19-Sep-2014 07:00:00	3788	127
HSNE60	-158.5500	72.1800	24-Aug-2012 21:00:00	19-Sep-2014 06:00:00	3813	117
HS06	-161.4500	71.3000	27-Aug-2011 14:00:00	12-Nov-2011 11:00:00	1846	167
SBN	-154.3620	71.5483	19-Aug-2014 18:00:00	16-Sep-2015 14:00:00	2074	90
SITE2	-160.9700	70.9800	10-Sep-2009 18:00:00	02-Nov-2010 23:00:00	4485	155
BURGER	-163.2800	71.2400	13-Aug-2011 16:00:00	14-Nov-2011 15:00:00	2232	232
CPAI01	-165.0000	71.0000	13-Aug-2012 12:00:00	31-Oct-2012 23:00:00	1908	297
CPAI02	-160.0000	71.6700	03-Aug-2011 15:00:00	08-Oct-2013 05:00:00	5242	122
C1	-163.1938	70.8388	06-Oct-2011 21:00:00	14-Nov-2011 15:00:00	931	237
C2	-164.2495	71.2196	19-Sep-2010 17:00:00	01-Nov-2010 08:00:00	1024	267

### 2.3 Satellite-Tracked Drifter Data

Subsurface-drogued (30 m) oceanographic satellite-tracked drifters were deployed in the U.S. Chukchi Sea by the National Oceanic and Atmospheric Administration Pacific Marine Environmental Laboratory in 2013 and 2015. Processed hourly drifter data were aligned with the closest HFR grid point to generate a set of drifter/HFR velocity data pairs (Figure 10). These data points were quantitatively and qualitatively assessed for shear and similarity of the velocity components. The drifters use ARGOS satellite system position fixes, which are less accurate than Global Positioning System (GPS) position locations. Hence, the data are useful for bulk comparisons, but analyses requiring high precision data are precluded.

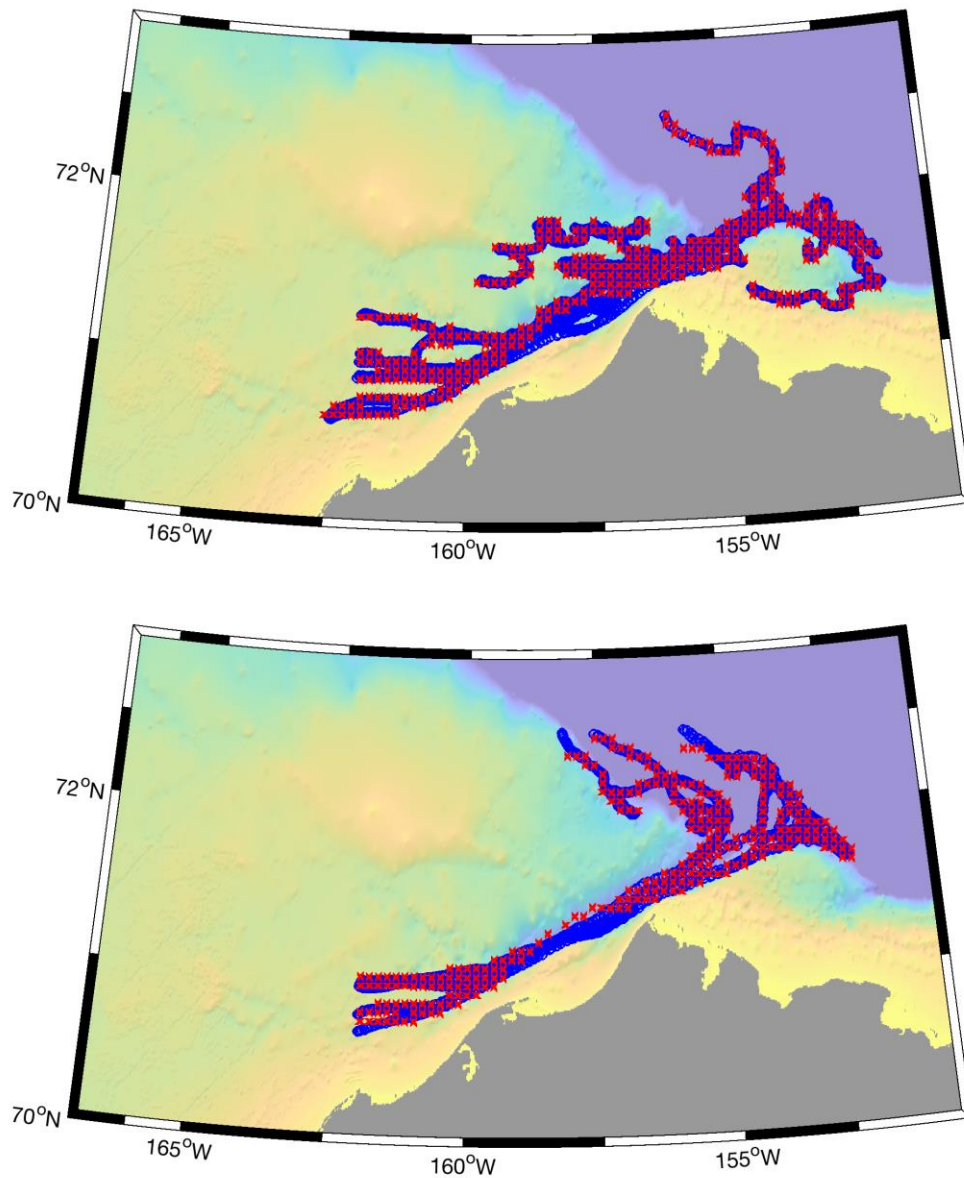


Figure 10: The upper panel shows the location of all sub-surface (30 m depth) drogued drifter position fixes (blue circles) in 2013, and the lower panel shows the 2015 dataset. Coincident HFR data points (red crosses) show locations of HFR-drifter data overlap in time.

## 2.4 Meteorological Data

Meteorological weather station data comes from the Utqiagvik airport (National Weather Service station PABR) and was extracted for the following parameters: date and time, wind direction (degrees), and wind speed ( $\text{m s}^{-1}$ ). The meteorological data were accessed from the National Climate Data Center (NCDC; <http://www.ncdc.noaa.gov/>) on 10 August 2012, 14 January 2014, and 10 January 2015 and from the National Center for Environmental Information (NCEI; <https://www.ncei.noaa.gov/>) on 28 April 2021.

We converted winds into east/west and north/south vector time series (oceanographic direction convention with positive east and north) and subjected them to a manual inspection process through which spikes and stuck sensor readings are removed. Bad data were identified by instances of an otherwise smoothly changing vector time series undergoing large (e.g.,  $> 15 \text{ m s}^{-1}$ ) instantaneous jumps and then immediately returning to nearly the original level at the next time step. Data were linearly interpolated to the top of each observation hour. Interpolated data were retained only for those that fell within observational data gaps shorter than six hours

For the daily HFR data maps and their analysis, we assembled the associated daily mean wind vector from the hourly PABR dataset (Figure 11). Given a typical atmospheric synoptic time scale of 3 – 5 days, the daily averaging allows us to coarsely resolve all major flow events that are forced by passing storm systems.

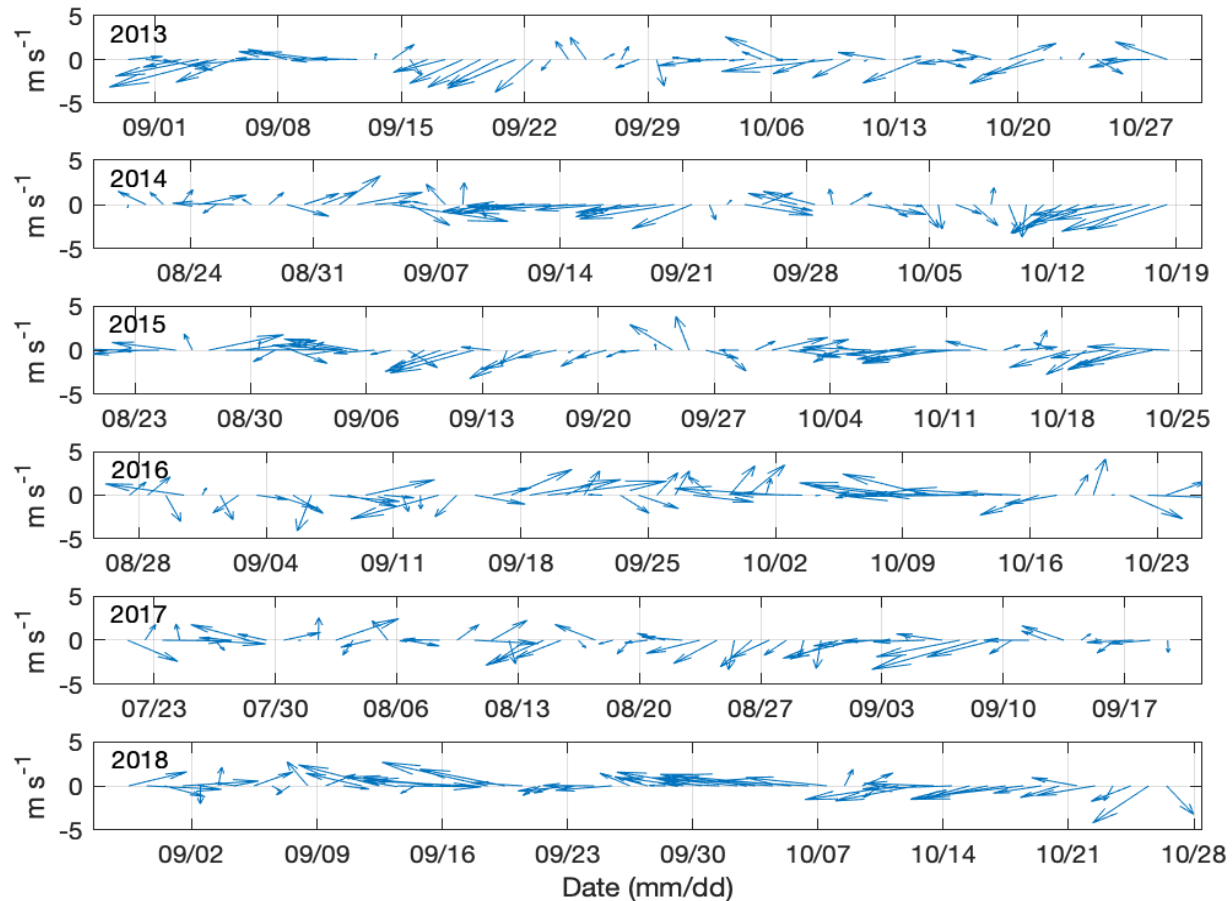


Figure 11: Daily mean wind speed and direction vectors from the PABR weather station for all days in the analyzed HFR dataset.

## 2.5 Analyses

Analysis of the current data includes the computation of flow statistics of the total data record and assessments of the flow field based on a variety of aggregation criteria. Aggregated data maps and plots are qualitatively described to highlight features that haven't been thoroughly addressed in the scientific literature. Metrics include daily mean speed and direction, variance, principal axes of variation, and eccentricity of the current ellipse. These are computed at HFR grid points and for the ADCP depth bins in the underlying water column. Time-lagged correlation analysis provides the basis for relating flow field variations to wind conditions. Following a linear interpolation to re-grid the HFR data onto a regular latitude-longitude grid, we compute (Eq. 1) the relative vorticity ( $\zeta_r$ ) of the surface currents as the curl of the horizontal velocity field, scaled by planetary vorticity ( $f$ ):

$$\zeta = f^{-1} \left[ \frac{\partial v}{\partial x} - \frac{\partial u}{\partial y} \right] \quad [\text{Eq. 1}]$$

This dimensionless ratio is a Rossby number, and thus represents the relative strength of the flow field rotational tendency relative to the Coriolis force.

Our time series analytical approach is primarily based on a comparison of coincident ADCP profile data with time series of surface currents from the HFR grid point closest to the mooring deployment site. Because HFR data coverage changes with wind conditions, ionosphere activity, radio frequency interference, and sea ice cover, the HFR data records have many gaps; therefore, we selected the mooring-HFR data pairs that provide the most complete temporal overlap. We characterize the basic statistical properties of each dataset (i.e., mean speed/direction, variance, eddy vs. steady kinetic energies) and then make comparisons between the two while under the influence of wind from each of the four cardinal quadrants. We devote particular attention to assessments of the vertical shear.

Self-organized mapping (SOM) is a machine learning technique that algorithmically groups arbitrary complex, nonlinear data into a user-defined number of characteristic patterns represented by simple geometric relationships (Kohonen, 2001). Through an iterative combination of competitive (shape-preserving) and cooperative (neighbor-influenced) learning techniques, the SOM algorithm can converge to an objectively optimal set of patterns (similarity maps) that describes the character of the underlying dataset, assigning each data record to one of the identified patterns. Fang et al. (2017) performed a SOM analysis on HFR data from the northeastern Chukchi Sea. Following that approach, we apply the technique to analyses of the surface velocity fields of the combined western Beaufort and northeastern Chukchi Seas HFR data for the years when we have data from both regions (2013 – 2018). We aggregate our findings based on dominant modes of system behavior, as identified by our SOM and statistical analyses and by prior studies that have identified flow field relationships to the driving surface winds (e.g., Weingartner et al., 2017a).

Alignment of the wind, ADCP, and HFR data proceeded as follows:

1. We selected the HFR data grid point closest to each mooring deployment site and formed an hourly time series of HFR data for periods when mooring deployment and HFR data overlap.
2. We constructed ADCP profiles over the upper 50 m of the water column (or less in shallower water), blanking the upper 6 m of the ADCP data to avoid contamination from surface waves, and interpolating to 1 m depth levels.
3. We assembled a time series of the PABR wind speed and direction data for the periods of ADCP and HFR data overlap.

### 3.0 Results

In this section, we analyze the HFR data alone and in conjunction with moored ADCP data and satellite-tracked drifter data.

#### 3.1 Surface Current Lateral Structure: Long-term Mean

We begin by computing the mean daily surface current vectors at all resolved HFR grid points (Figure 12). The six-year dataset yielded 362 days of usable averages, although the spatial coverage varied from year to year as a consequence of antenna siting, calibrations, number of high wind events, bearing angles, and changes in the local environment. The average wind vector for these days from PABR is directed weakly toward the southwest ( $-2.10 - 0.51i$  m s<sup>-1</sup>), which is close in both magnitude and direction to the 1940 – 2020 long-term mean PABR wind vector ( $-2.00 - 0.43i$  m s<sup>-1</sup>).

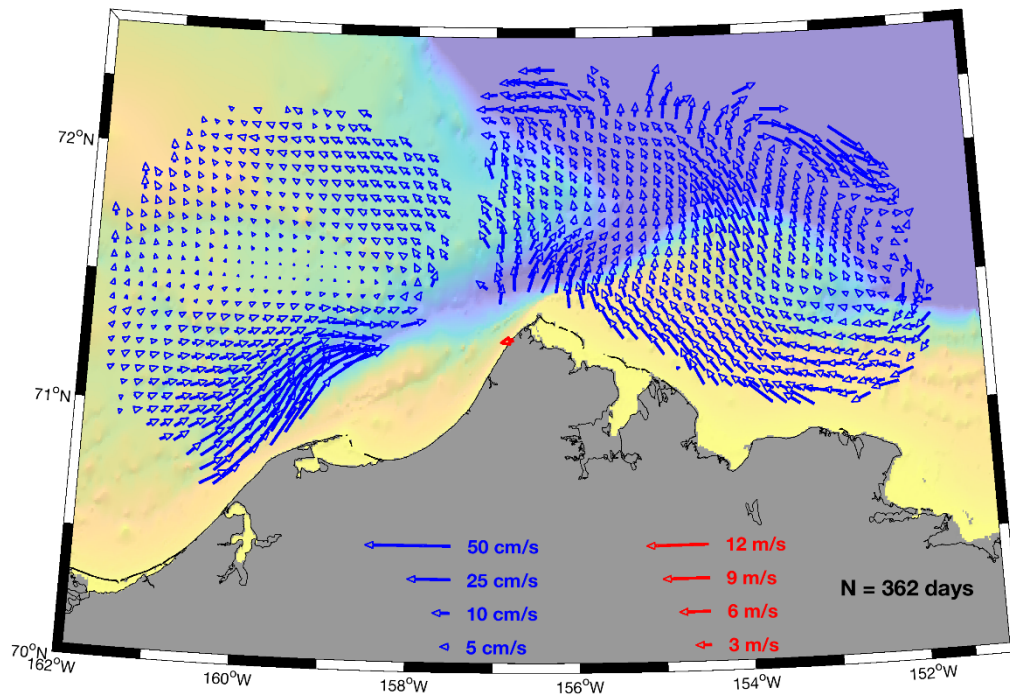


Figure 12: Mean of all daily average HFR current fields over 2013 – 2018. The red vector located at PABR denotes the mean wind over the same 362 days of the HFR record. Color shading depicts bathymetric depths between 0 m (yellow) and 150 m depth (purple).

The mean HFR surface current field and the associated maps of mean speed (Figure 13, shown as annual means in Appendix A), current variance (Figure 14, shown as annual means in Appendix B), principal axes (Figure 15), divergence (Figure 16), and vorticity (Figure 17) depict the following notable features:

1. The swift ACC that funnels into Barrow Canyon from the southwest. The ACC's cross-shelf structure is shown to extend about 40 km away from the coast near Wainwright.
2. Elevated speeds close to shore in the Beaufort Sea, which are associated with relatively low levels of flow variance, suggesting some degree of persistence associated with the prevailing wind forcing.

3. Elevated speeds near the diverging and turning bathymetry at the eastern side of the mouth of Barrow Canyon, where the orientation of the bathymetric contours change from southwest-northeast to northwest-southeast.
4. Over much of Hanna Shoal, the surface currents primarily have a northward orientation.
5. Surface currents to the east and southeast of Hanna Shoal are directed, in agreement with Ekman dynamics relative to the mean wind vector, to the northwest.
6. Low flow variance between Hanna Shoal and Barrow Canyon.
7. Transport through Barrow Canyon is enhanced by flow directed northwestward from the western Beaufort Sea shelf.
8. Flow exits Barrow Canyon undergoing a counterclockwise rotation near the western side and clockwise rotation on the eastern side.
9. Upper slope waters flow onto the Beaufort shelf in the vicinity of a topographic depression (minor canyon) that exists near 153°W.
10. Flow convergence at the head of Barrow Canyon, at the intersection of the U.S. Chukchi and Beaufort Seas in Barrow Canyon, along the coast in the Beaufort Sea, and at the mouth of Barrow Canyon.
11. Flow divergence over the outer Beaufort shelf between 153 and 154.5°W and near 72°N.
12. Positive curl whose vorticity exceeds that of the Coriolis force along the length of Barrow Canyon and along the Chukchi slope west of Barrow Canyon. Negative curl along the Beaufort continental slope east of Barrow Canyon and on the inner portion of the Beaufort shelf.

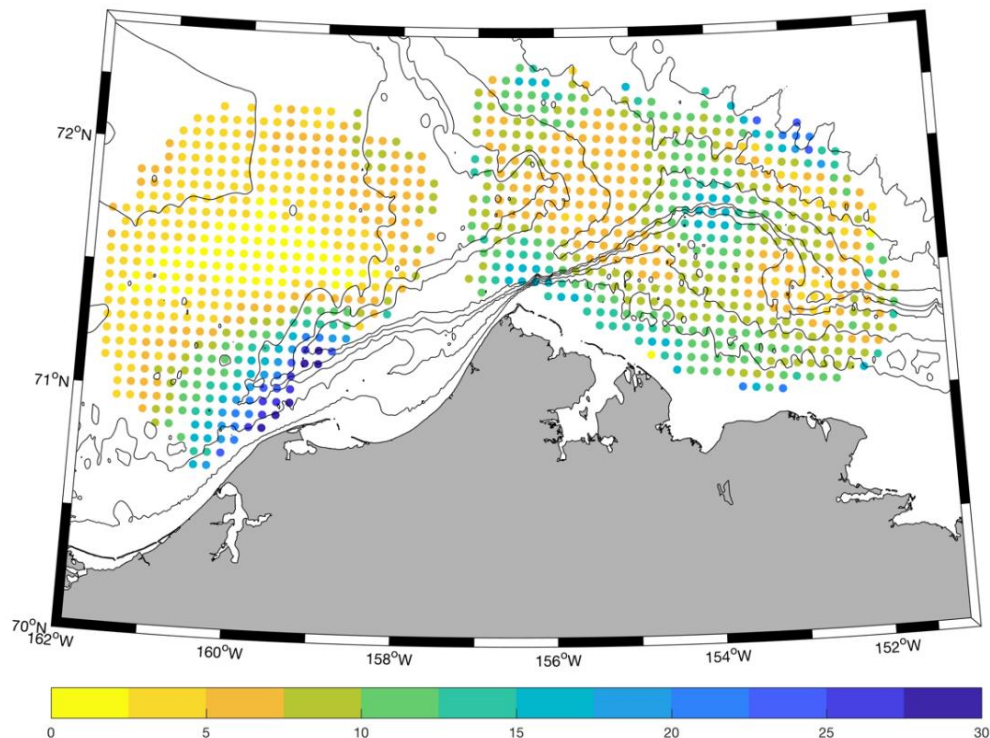


Figure 13: Mean speed ( $\text{cm s}^{-1}$ ) of the HFR flow field for all 362 days in the record. Bathymetric contours are drawn at 20, 40, 60, 80, 100, 200, 1000, and 2000 m depth levels.

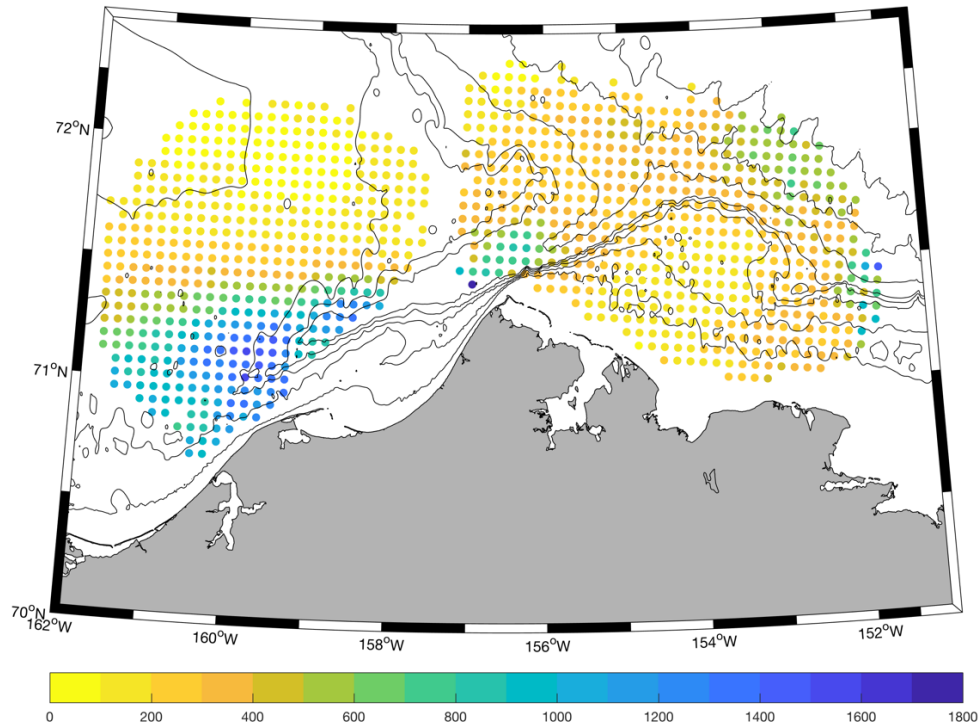


Figure 14: Variance ( $\text{cm}^2 \text{s}^{-2}$ ) of the HFR flow field for all 362 days in the record. Bathymetric contours are drawn at 20, 40, 60, 80, 100, 200, 1000, and 2000 m depth levels.

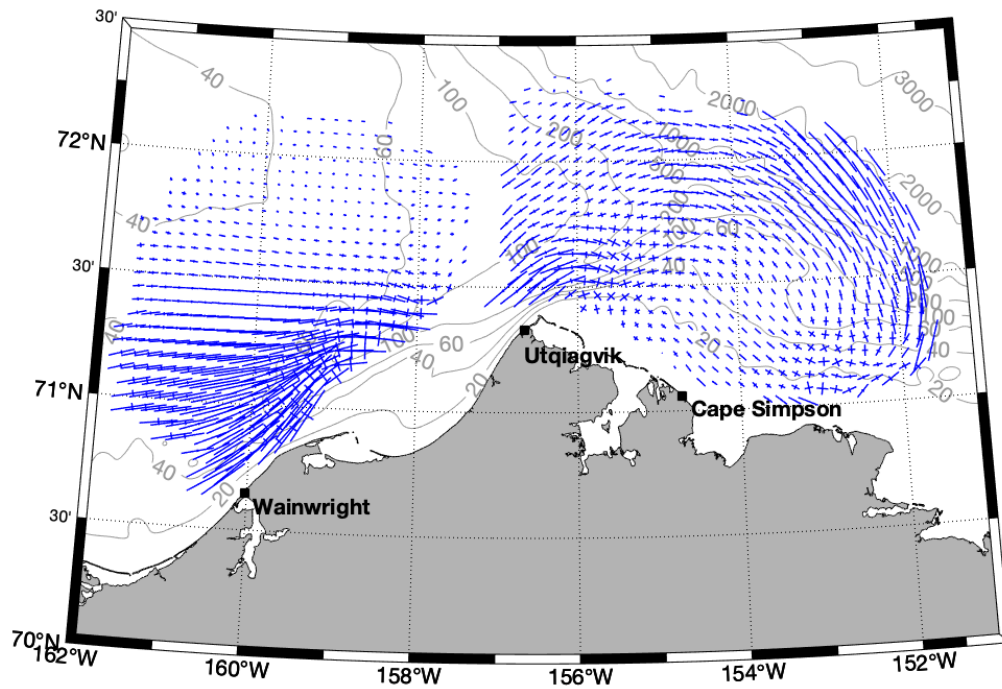


Figure 15: Ellipses showing the orientation, magnitude, and eccentricity along and across the principal axis of variation.

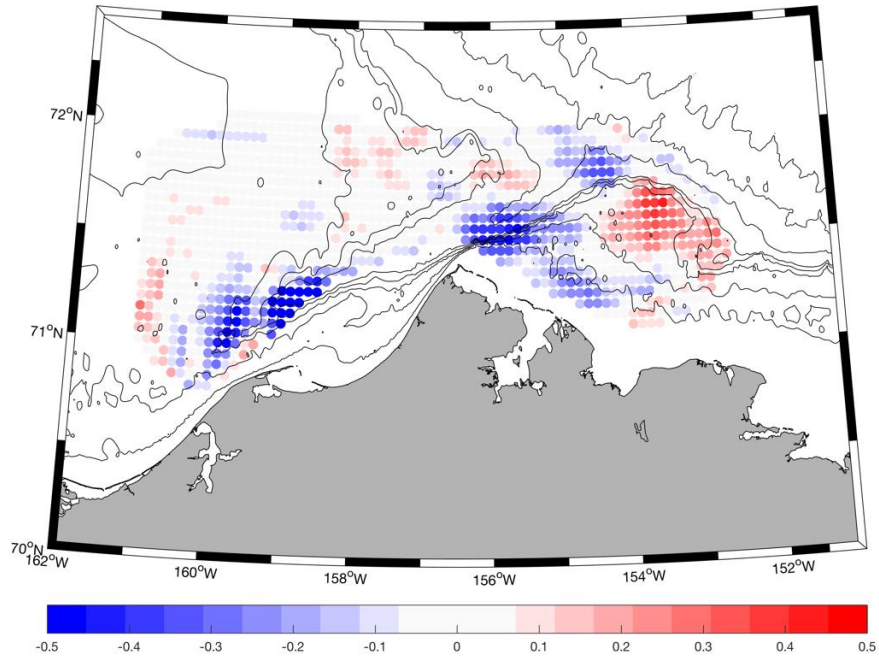


Figure 16: Divergence ( $\text{cm s}^{-1} \text{ km}^{-1}$ ) of the mean HFR flow field shown in Figure 12, excluding the outer grid points with fewer data. Blue colors denote convergence and red colors denote divergence.

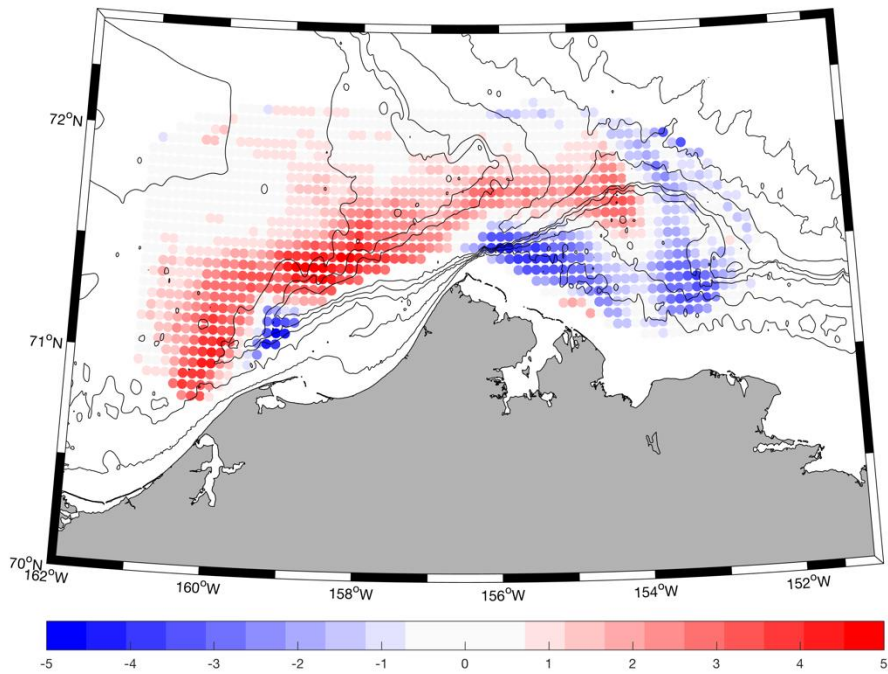


Figure 17: Vorticity Rossby number (dimensionless) of the mean HFR flow field shown in Figure 12, excluding the outer grid points with fewer data.

The mean flow map and associated statistical summaries (Figures 12 – 17) are somewhat challenging to interpret because they represent the average of many vectors that change orientation in time, due to the fluctuating nature of the total current field. Because many of the flow field variations are known to be wind-driven in this region (Pickart et al., 2013; Weingartner et al., 2017a; 2017b), we next turn to a more nuanced analysis that is based on both wind speed and direction.

### 3.2 Surface Current Lateral Structure: Wind Effects

Several studies (e.g., Okkonen et al., 2009; Schultze and Pickart, 2012; Fang et al., 2017; Weingartner et al., 2017a; Pickart et al., 2013; Danielson et al., 2017; Danielson et al., 2018) have found that the northeastern Chukchi Sea flow field is prone to considerable reorganization from day to day, including current reversals, especially under the influence of winds that exceed  $\sim 6 \text{ m s}^{-1}$ . Hence, we generate a set of surface current maps (Figures 18 – 21) that show the average flow field under the influence of daily mean wind speeds  $> 6 \text{ m s}^{-1}$  when the daily mean wind vectors are oriented from each of the four cardinal quadrants (NE, SE, SW, and NW).

Nearly 40% of the days in our study (132 out of 362) occurred under the influence of winds having a mean daily wind speed of more than  $6 \text{ m s}^{-1}$ . Of these 132, more than half (69) were subject to strong winds (Figure 18) that approximated the prevailing southwestward wind direction (winds blowing from the NE to the SW). The mean surface currents for the strong southwestward-blowing wind condition exhibit the following characteristics:

1. Up-canyon flow and a reversed ACC west of Point Barrow.
2. Cross-canyon flow east of Point Barrow.
3. Westward flow along the Beaufort Sea coast.
4. On-shelf flow near  $153^\circ\text{W}$  in the Beaufort Sea, forming an anticyclonic (clockwise) gyre system that straddles the outer shelf and slope region.
5. Westward flow past Hanna Shoal.

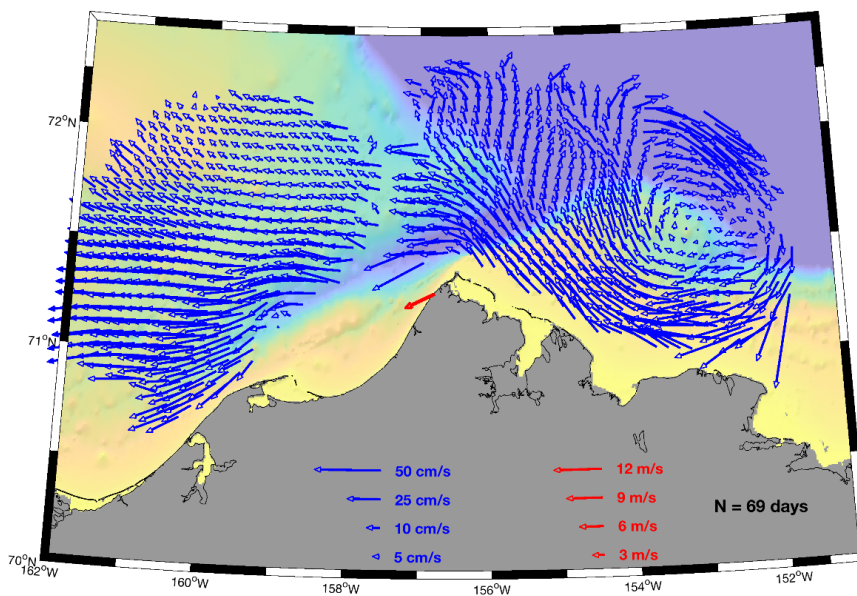


Figure 18: Mean surface current (blue) and wind (red) vectors for the case of strong winds (daily average  $> 6 \text{ m s}^{-1}$ ) winds blowing to the SW. N denotes the number of days of data that comprise this composite.

Only 10 days were subject to the influence of southeastward-blowing winds having a mean daily wind speed of more than  $6 \text{ m s}^{-1}$  (Figure 19). We caution that this composite likely suffers in quality due to the small sample size. The mean surface currents for the strong southeastward wind conditions exhibit the following characteristics:

1. Down-canyon flow with a strong on-shore component directed from the NW to the SE.
2. Eastward flow from Barrow Canyon onto the western Beaufort shelf.
3. On-shelf flow northwest of Barrow Canyon.
4. Potential recirculation of shelf break waters back into Barrow Canyon as they rejoin the ACC south of Hanna Shoal.
5. Weak eastward flow along the Beaufort Sea coast.
6. Westward flow along the Beaufort shelf break.

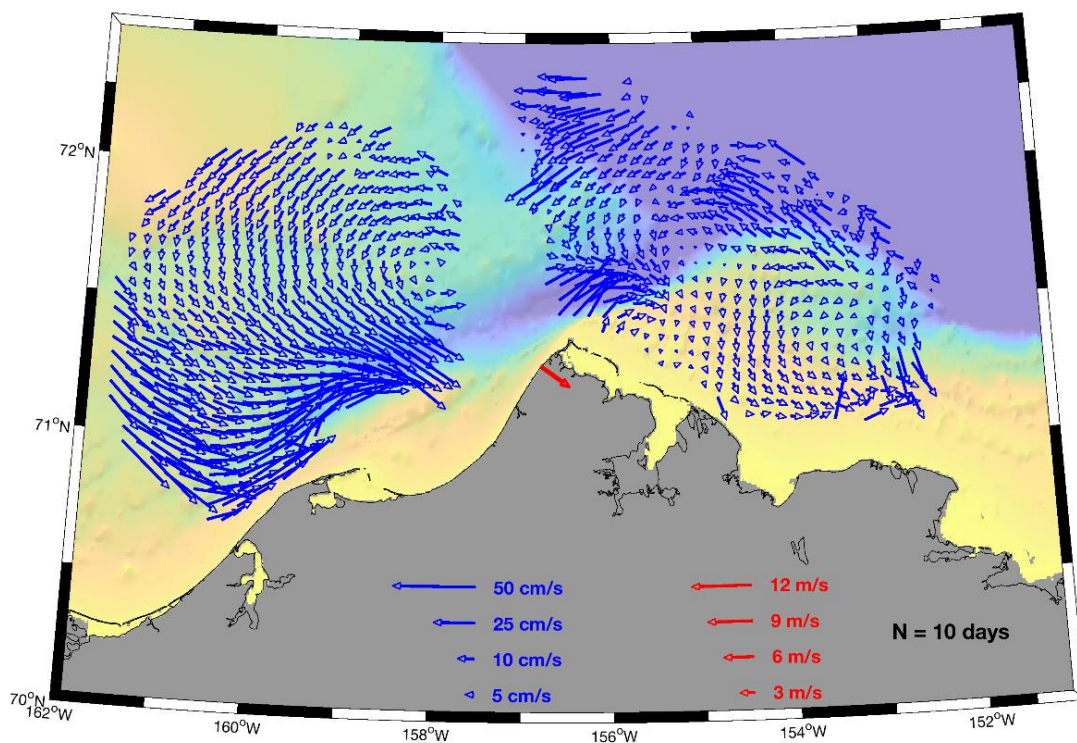


Figure 19: Mean surface current (blue) and wind (red) vectors for the case of strong winds (daily average  $> 6 \text{ m s}^{-1}$ ) blowing to the SE. N denotes the number of days of data that comprise this composite.

Thirty-five days (Figure 20) occurred under the influence of northwestward-blowing winds having a mean daily wind speed of more than  $6 \text{ m s}^{-1}$ . The mean surface currents for the strong northwestward wind conditions exhibit the following characteristics:

1. Down-canyon flow in Barrow Canyon, with a possible offshore deflection of the ACC near the head of the canyon.
2. Northwestward flow on the outer shelf east and southeast of Hanna Shoal.
3. Strong northwestward flow in the Beaufort Sea's coastal zone that converges with the flow in Barrow Canyon, deflecting this flow northward.
4. Along-shelf flow near  $153^\circ\text{W}$  on the western Beaufort slope.
5. Northward flow across the outer western Beaufort shelf.

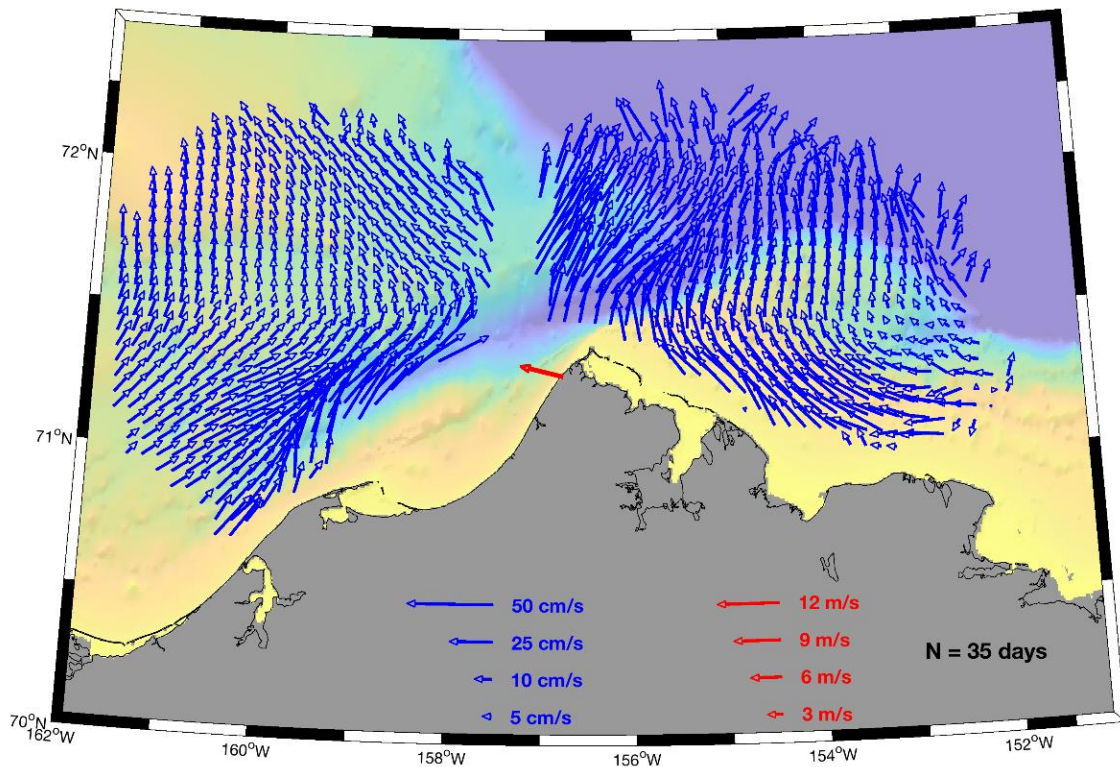


Figure 20: Mean surface current (blue) and wind (red) vectors for the case of strong winds (daily average  $> 6 \text{ m s}^{-1}$ ) blowing to the NW. N denotes the number of days of data that comprise this composite.

Eighteen days) were under the influence of northeastward-blowing winds having a mean daily wind speed of more than  $6 \text{ m s}^{-1}$  (Figure 21). The mean surface currents for the strong northeastward wind conditions exhibit the following characteristics:

1. On the south side of Hanna Shoal, eastward flow that feeds the Barrow Canyon transport.
2. Strong down-canyon flow in Barrow Canyon.
3. Eastward flow onto the Beaufort shelf as the current flows past Point Barrow.
4. Off-shore flow in the Beaufort slope region near  $153^\circ\text{W}$ .
5. A cyclonic (counterclockwise) recirculation cell from the shelf break and slope region back into the mouth of Barrow Canyon, with some flow continuing westward along the Chukchi shelf break.

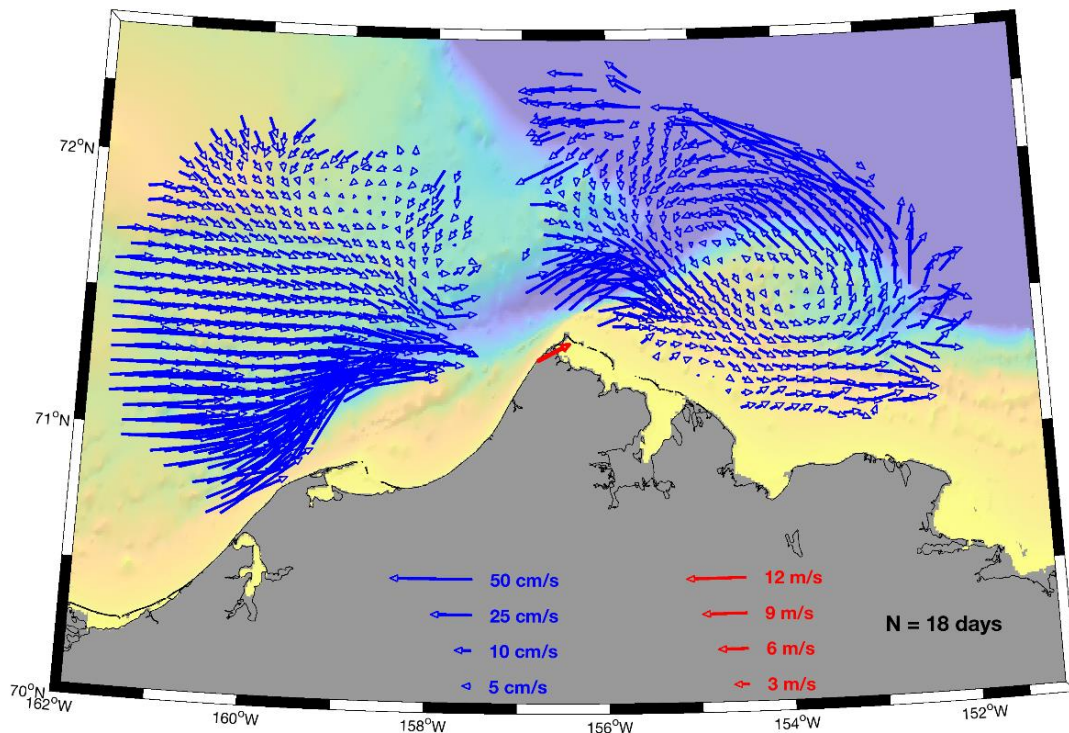


Figure 21: Mean surface current (blue) and wind (red) vectors for the case of strong winds (daily average  $> 6 \text{ m s}^{-1}$ ) blowing to the NE. N denotes the number of days of data that comprise this composite.

Together, the four composites based on energetic winds that are shown in Figures 18 – 21 depict a flow system that alternates between strongly contrasting regimes, portions of which have not been previously described in the scientific literature and which represent a newly updated understanding of flow pathways in this region. Portions of these results will need verification by future research. The advection patterns depicted by these regimes likely exert dominant control over the advection of plankton, oil, nutrients, and other important water-borne biotic and abiotic constituents.

Composites for the condition of weak wind ( $< 4 \text{ m s}^{-1}$ ) blowing from the same four quadrants as the above analysis are provided in Appendix C. These show relatively modest differences between wind directions. Thus, we create a single composite (Figure 22) for all of these days.

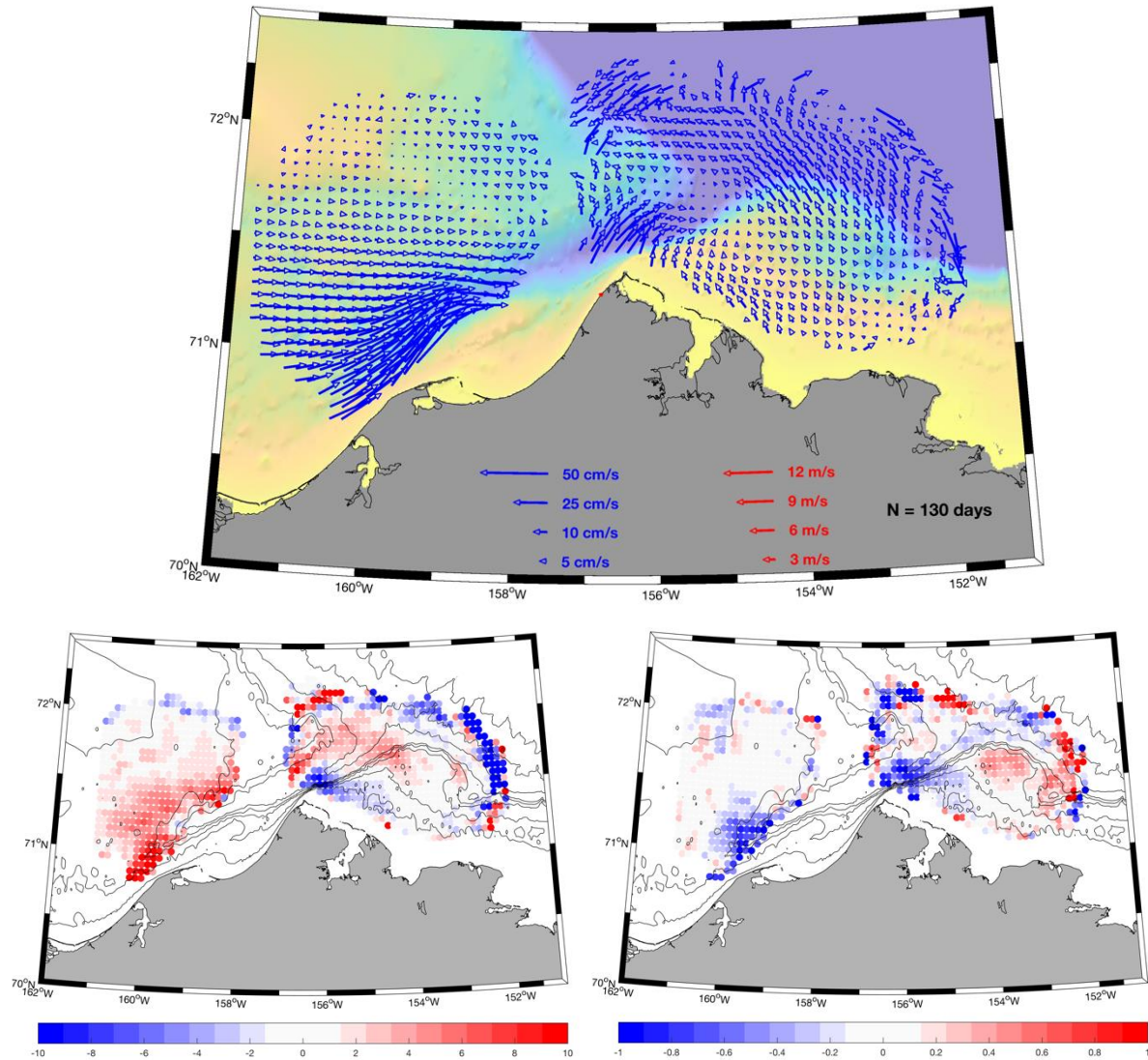


Figure 22: Top panel: Mean surface current (blue) and wind (red) vectors for the case of weak winds (daily average  $< 4 \text{ m s}^{-1}$ ) blowing from all directions. N denotes the number of days of data that comprise this composite. Bottom left panel: Vorticity Rossby number of the current vector map at top. Bottom right panel: Divergence ( $\text{cm s}^{-1} \text{ km}^{-1}$ ) of the current vector map at top. Blue colors denote convergence and red colors denote divergence.

The weak wind composite shows a number of features in common with the averages shown above. These include enhanced ACC flow down Barrow Canyon, westward flow on the western Beaufort shelf that converges with the Barrow Canyon flow, relatively weak flow over Hanna Shoal, positive relative vorticity and convergent flow for the waters entering Barrow Canyon from the north and west, divergent flow over the outer Beaufort shelf, and convergent flow where the Beaufort Sea's westward-directed coastal flow impinges upon Barrow Canyon. More details on divergence and vorticity based on wind speed and direction are shown in Appendices D and E, respectively. Some features near the edge of the data masks are likely the consequence of few data points (e.g., the southwestward flow onto the Chukchi shelf from the Chukchi slope and eastward-oriented vectors along the northeast side of the Beaufort Sea HFR mask).

### 3.3 Surface Current Flow Field Lateral Structure: Self-organized Maps

Self-organized map (SOM) analysis is applied to the full multi-year dataset comprised of all daily averages. Appendix F contains the results of SOM analyses on a year-by-year basis and can help us assess the overall stability, consistency, and representativeness of the multiyear analysis. Like the aggregate flow maps presented above, low data coverage in a grid cell tends to affect our results. For the SOMs shown here, the flow field is damped at these locations; the small magnitude vectors observed at the edges of the data mask reflect this bias.

Sensitivity testing of the SOM results revealed six distinct patterns that can be separated into two primary groupings defined by characteristics of flow magnitude, spatial structure, and orientation (Figures 23 – 25). SOM patterns 1 – 4 all depict an eastward-flowing ACC that is directed into Barrow Canyon. They comprise 14.1%, 29.8%, 11.3%, and 13.2% of the dataset, respectively. The SOM pattern 3 has the weakest coastal current of these four, and it is associated with a relatively strong and flow-opposing wind vector. SOM patterns 5 and 6 comprise 24.0% and 7.5% of the data, respectively. Both depict a reversed ACC and enhanced westward flow on the Beaufort shelf, with SOM pattern 5 having the stronger flow field (and wind field) of the two. The Chukchi flow field near Wainwright has more of an offshore component in SOM pattern 6, suggesting that this condition could be associated with an along-shore convergence relative to the shelf currents west of the HFR grid shown here and as observed by Fang et al. (2017). SOM patterns 5 and 6 also show an on-shelf flow near 153°W and southeastward flow along the Beaufort slope. Together with the westward flow closer to shore, these patterns form an anticyclonic gyre centered near the western side of the small canyon near 153°W.

Some features are found in common across all six SOM patterns. All show westward flow on the inner Beaufort Sea shelf (offshore of Elson Lagoon). All depict a cross-isobath flow from the shelf onto the upper continental slope just east of the mouth of Barrow Canyon (near 154°W).

SOM patterns 1 – 4 show a surface current that deflects westward along the Chukchi slope as it exits Barrow Canyon. SOM patterns 5 and 6 also depict surface currents oriented in this direction, but rather than following the bathymetric contours, for these two cases of strong southwestward blowing winds, the currents in lower Barrow Canyon are directed across the canyon, consistent with Ekman wind forcing dynamics.

Over the broad expanse of shelf between Hanna Shoal and lower Barrow Canyon, all SOM patterns show a flow that is oriented to the northwest with modest speed magnitudes.

The lack of any SOM pattern showing a reversed flow on the Beaufort shelf suggests that these multiyear SOM patterns miss a substantial component of the variability that is endemic to this region. This flow variability emerges in the composite averages (Figure 21) but is too ephemeral to be revealed with our SOM analysis.

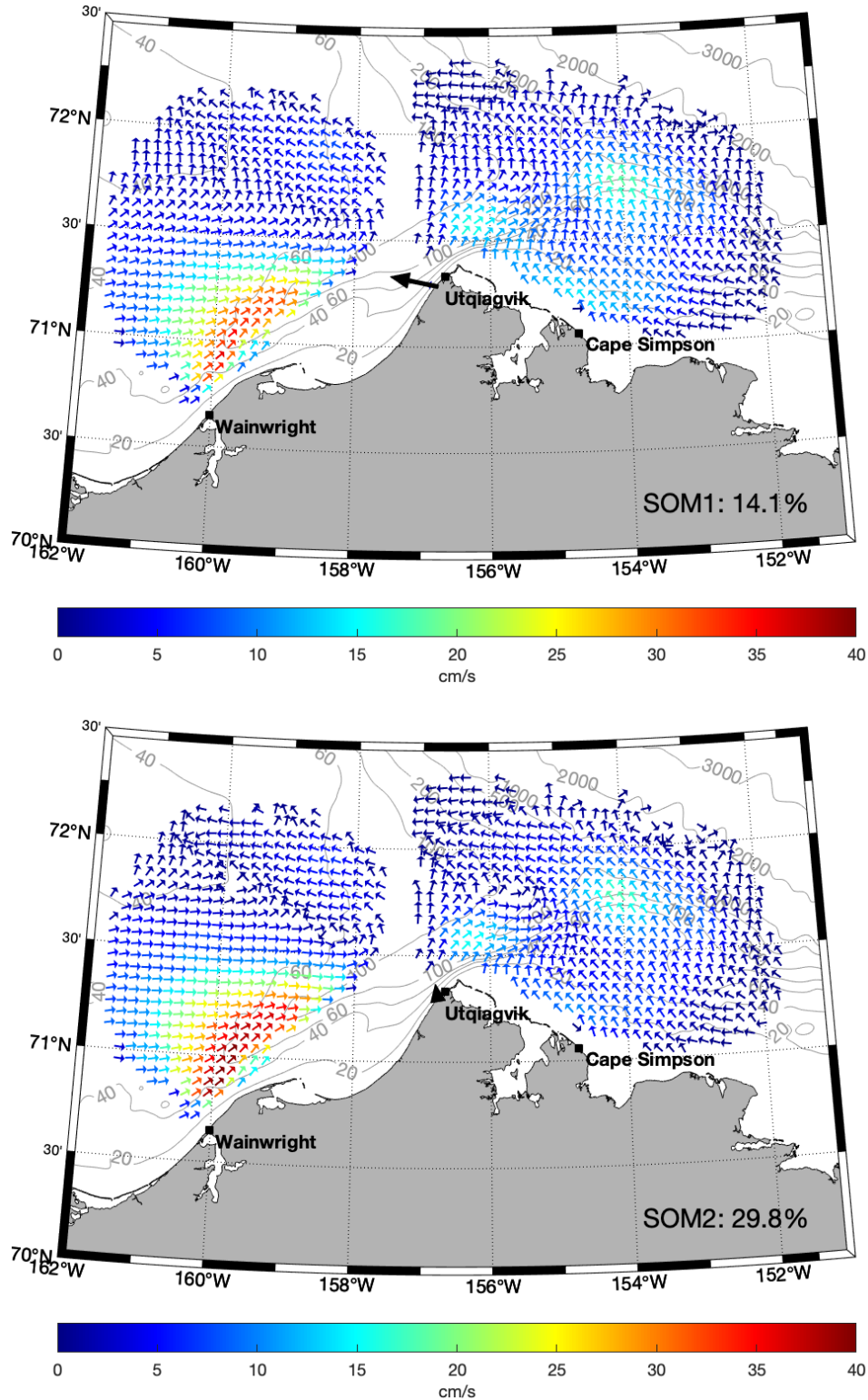


Figure 23: Self-organized map (SOM) patterns 1 (top) and 2 (bottom), shown with the percentage of all daily mean HFR maps that comprise this composite. The black vector at Utqiaġvik denotes the wind speed and direction for the days that correspond to the depicted SOM patterns.

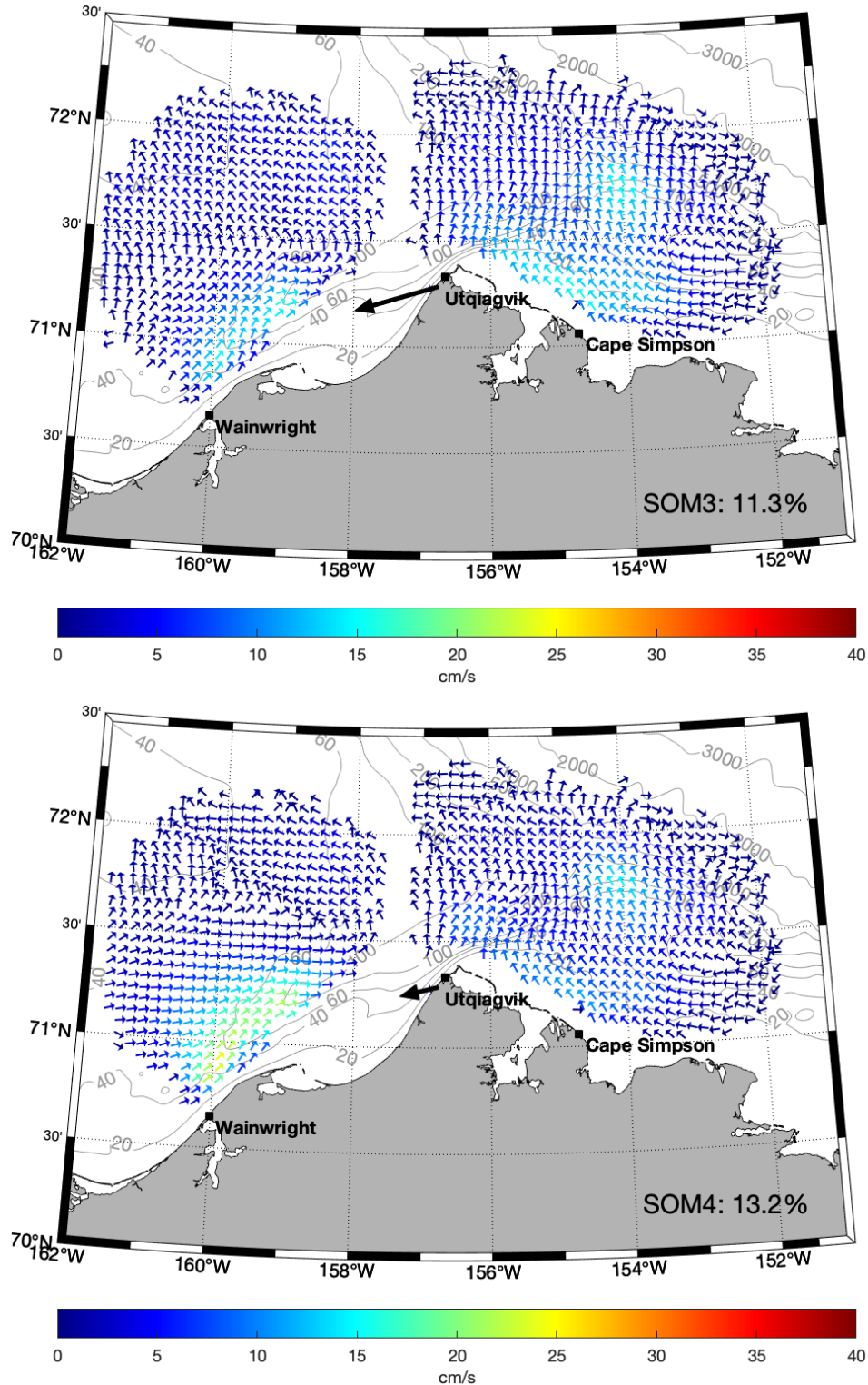


Figure 24: Self-organized map (SOM) patterns 3 (top) and 4 (bottom), shown with the percentage of all daily mean HFR maps that comprise this composite. The black vector at Utqiagvik denotes the wind speed and direction for the days that correspond to the depicted SOM patterns.

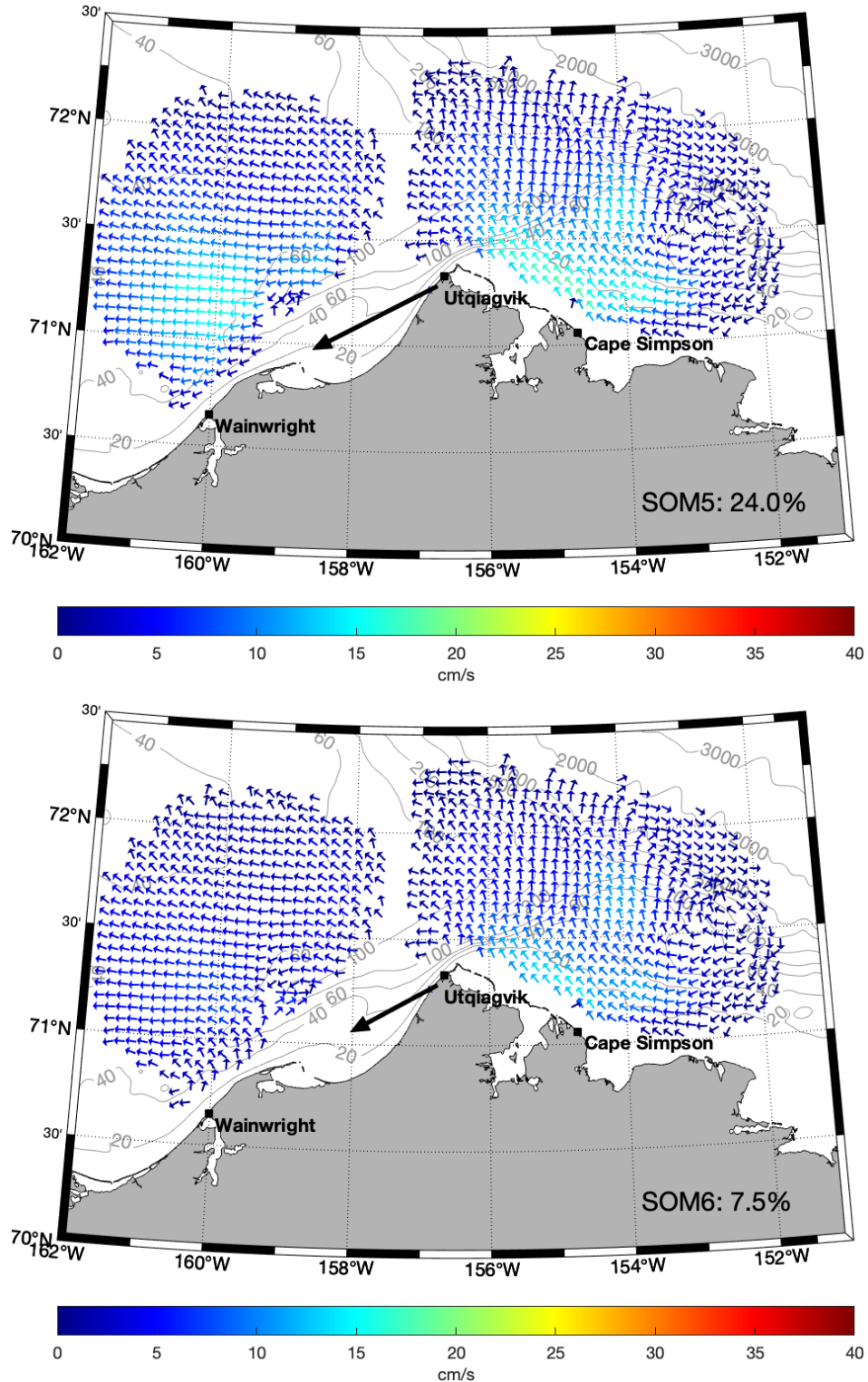


Figure 25: Self-organized map (SOM) patterns 5 (top) and 6 (bottom), shown with the percentage of all daily mean HFR maps that comprise this composite. The black vector at Utqiagvik denotes the wind speed and direction for the days that correspond to the depicted SOM patterns.

### 3.4 Flow Field Vertical Structure

The ADCP data allow us to assess the nature of the subsurface velocity field and the degree to which the HFR and ADCP data capture the same current features of flow events, and their timings. While the overall agreement between the two datasets is clear visually (Figure 26), it is also apparent that the surface flows do not provide a perfect representation of the subsurface flows, and vice versa. This mismatch in the flow field vertically is a key motivation for this study, as we are interested in the nature of the velocity shear within the water column.

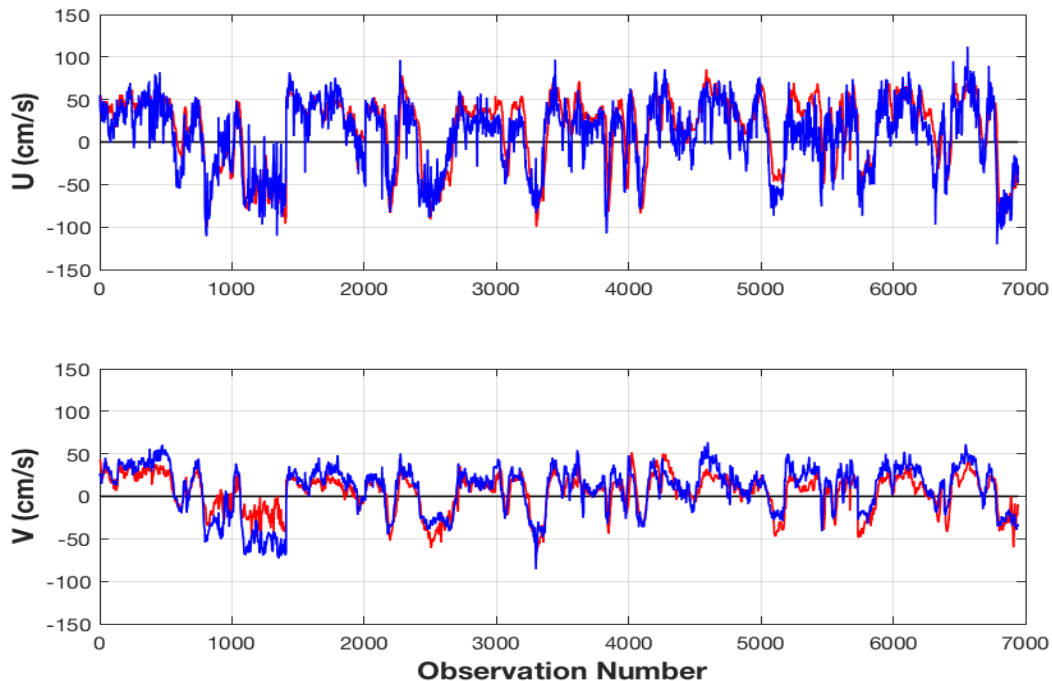


Figure 26: Comparison of east-west (U, top panel) and north-south (V, bottom panel) currents collected at mooring site BC2 for all hours of ADCP and HFR data record overlap at this site. Red traces show the vertically-averaged ADCP data; blue traces show the surface HFR data. The hourly data shown in this plot were collected over five years and are displayed chronologically on the horizontal axis as consecutive observation numbers.

Record-length mean values of the surface HFR, vertically-averaged ADCP, and wind vectors (Figure 27) show that, in the mean, the surface currents are sheared relative to the subsurface flow at all mooring sites. In many cases, the mean ocean flows are oriented at an obtuse angle relative to the wind direction, with a relatively modest angle between the surface and subsurface flow vectors. In some cases, the surface flow is oriented at approximately 45 degrees to the right of the wind (e.g., HSNE60 and BCW) and, in most cases, the mean subsurface flow is oriented to the right of the surface flow. Both orientations are broadly consistent with surface Ekman dynamics. At BC2, BC3, and BC4 the mean flow at the surface and at depth oppose the mean wind direction, showing that factors other than the wind exert primary influence on the flow approaching Barrow Canyon. At some locations, the subsurface velocity vector is oriented relative to the surface flow at an acute angle and to the left of the surface flow. At other locations, the subsurface flow is oriented at an acute angle but to the right of the surface flow. These contrasting orientations suggest a varying degree of influence from the surface and bottom boundary layers.

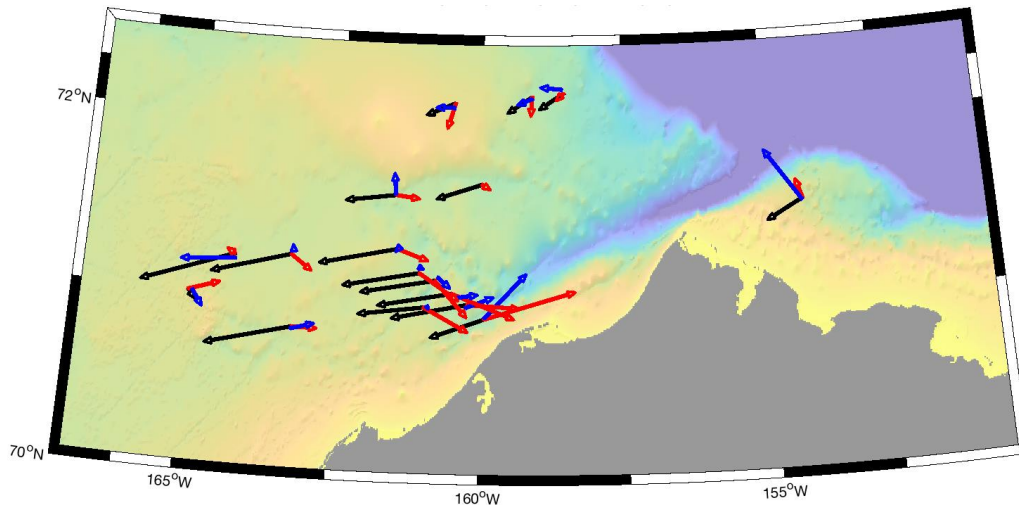


Figure 27: Mean PABR wind (black), HFR surface current (blue), and ADCP subsurface current (red) velocity vectors at all mooring sites. The vectors at each mooring site are averaged over the full period of HFR/ADCP record overlap for that installation.

We next turn to the meridional and zonal components of near-surface vertical shear of the lateral currents based on the surface HFR measurement and the closest-to-surface good ADCP velocity bin. For consistent comparison, shears are scaled by the separation distance, thus giving units of  $s^{-1}$ . Our first analysis shows a regionally-varying relationship between the winds and the shear response (Figures 28 and 29). For example, at mooring BC6 and C2 positive zonal wind anomalies are associated with positive shear anomalies. At SBN, in the western Beaufort Sea near the shelf break, positive zonal wind anomalies are associated with negative shears.

The shear relationship is further revealed when we average the shear responses as a function of wind speed. Notably, the magnitude of the shear response varies from site to site, as does the sign of the relationship (Figure 29). For example, stations CEO and CAPI01 exhibit a clear negative slope in the zonal shear response to zonal winds (black stars), while many of the sites show a positive relationship, and a few show no clear relationship (HSNE40, HSNE50, HSNE60, C1, C2, and Burger). For the meridional shear response to zonal winds, the HSNE moorings again exhibit no strong relationship, but some sites have meridional shear responses that are quite sensitive to the zonal wind magnitude and direction (CPAI02, BC4, BC5, and BC6). The response to zonal winds is also spatially variable, but there are no sites at which the response is clearly negative. Instead, both zonal and meridional shears respond with positive shear anomalies to positive wind anomalies, although the response is spatially nonuniform in magnitude. Aside from ocean dynamics, a lack of a strong relationship to the wind could be due to the distance between any mooring site and the PABR meteorological station.

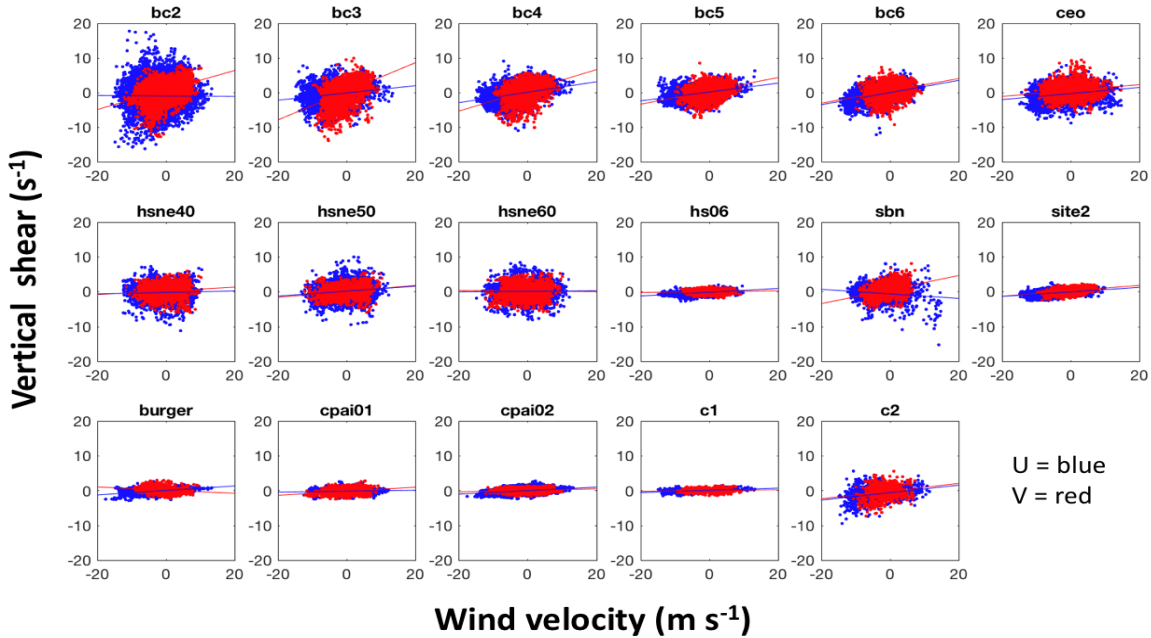


Figure 28: Near-surface vertical current shear (vertical axes) based on wind component magnitude (horizontal axes) at the 17 mooring sites. East-west wind and shear components are plotted in blue and the north-south wind and shear components are plotted in red.

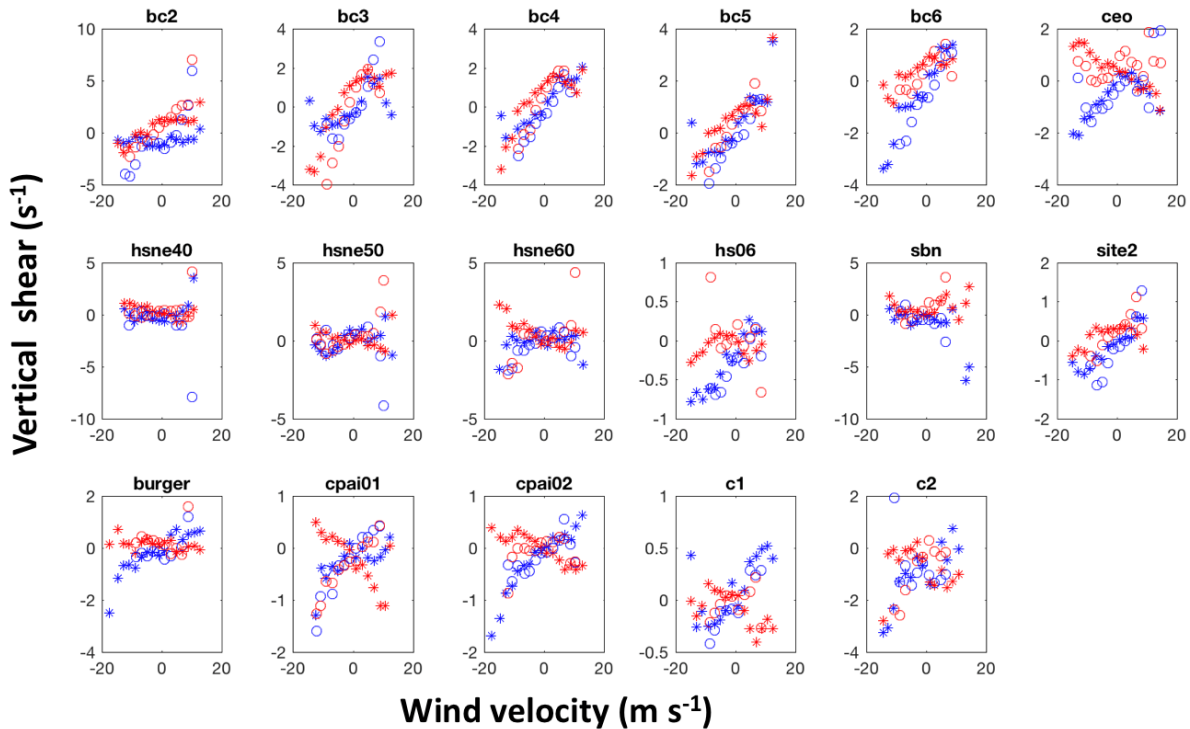


Figure 29: Upper-ocean shear response based on wind velocity components, where the data is binned for wind component magnitudes between  $-20$  and  $+20$   $\text{m s}^{-1}$ . The response to zonal wind is shown for the zonal shear (red stars) and meridional shear (blue stars). The response to meridional winds is shown for the zonal shear (blue circles) and meridional shear (red circles). Note the difference in scale across all subplot vertical axes.

We find that the local characteristic shape of the shear profile exhibits little variation at BC2 as a function of wind speed and direction (Figure 30) and that at this particular location the surface currents are usually weaker than currents at 5 – 20 m depth. The flow is westward (direction  $\sim 220^\circ\text{T}$ ) only for the case of strong westward winds (wind speed (WS)  $> 6 \text{ m s}^{-1}$ ) and the flow is eastward (direction  $\sim 70^\circ\text{T}$ ) for weak westward winds and all cases with eastward winds. However, even under the influence of eastward wind (heading with the prevailing currents), the HFR data show a somewhat slower surface velocity than the ADCP data record at depth. The reason for this relationship is not fully clear, but it may be related to surface boundary layer effects.

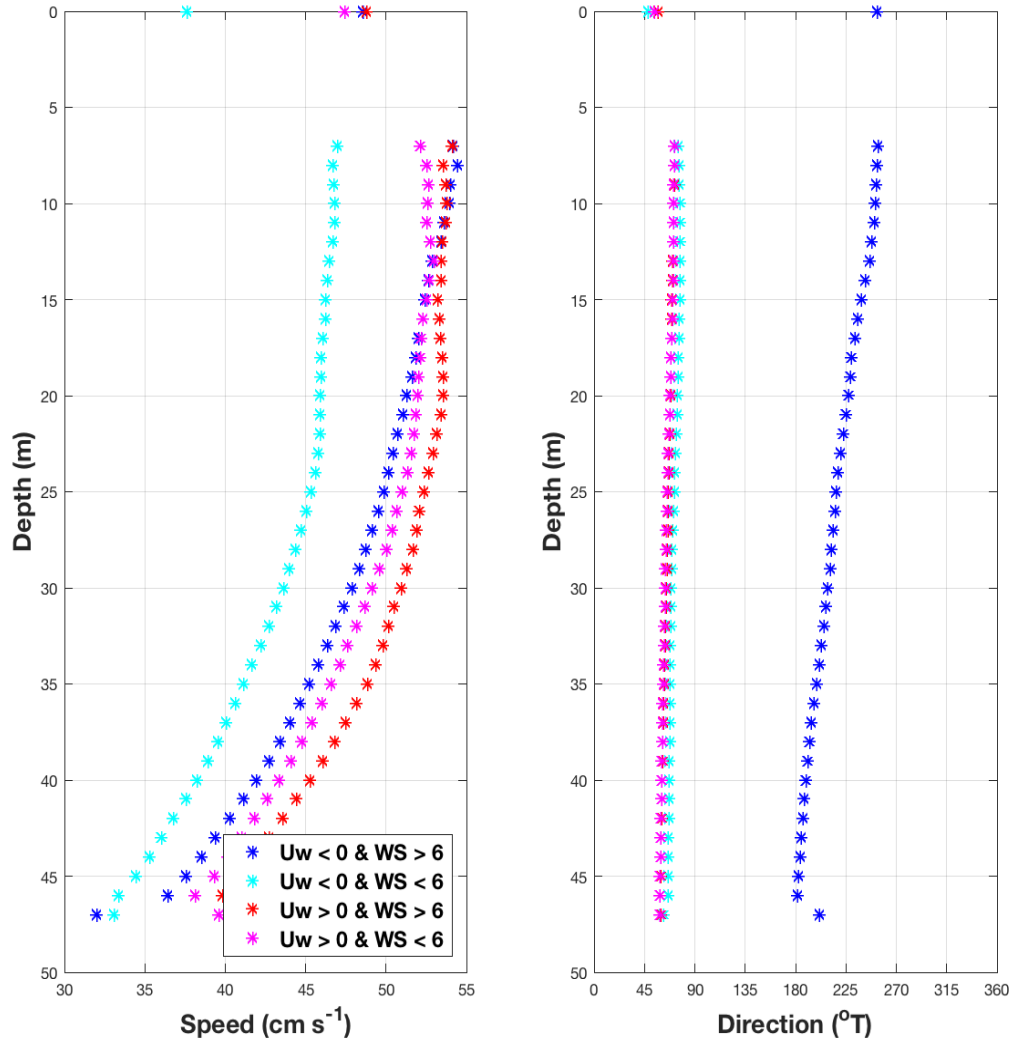


Figure 30: Mooring BC2 vertical shear in speed (left) and direction (right) from surface (HFR) and subsurface (ADCP) data based on the four wind speed (WS) and direction criteria are shown in the legend. The wind component,  $U_w$ , represents the component aligned with the principal axis of variation.

Farther offshore, mooring BC6 (Figure 31) shows a response that similarly exhibits little variation in direction for three of the cases but the strong westward case exhibits a strong directional shear, with the upper 10 m of the water column directed NW ( $\sim 300^\circ\text{T}$ ), while the bottom 20 m of the water column retains a direction that is close to the direction of the other three cases (between east and south). For strong westward wind, the sense of rotation downward from the surface is in opposite directions at BC2 and BC6.

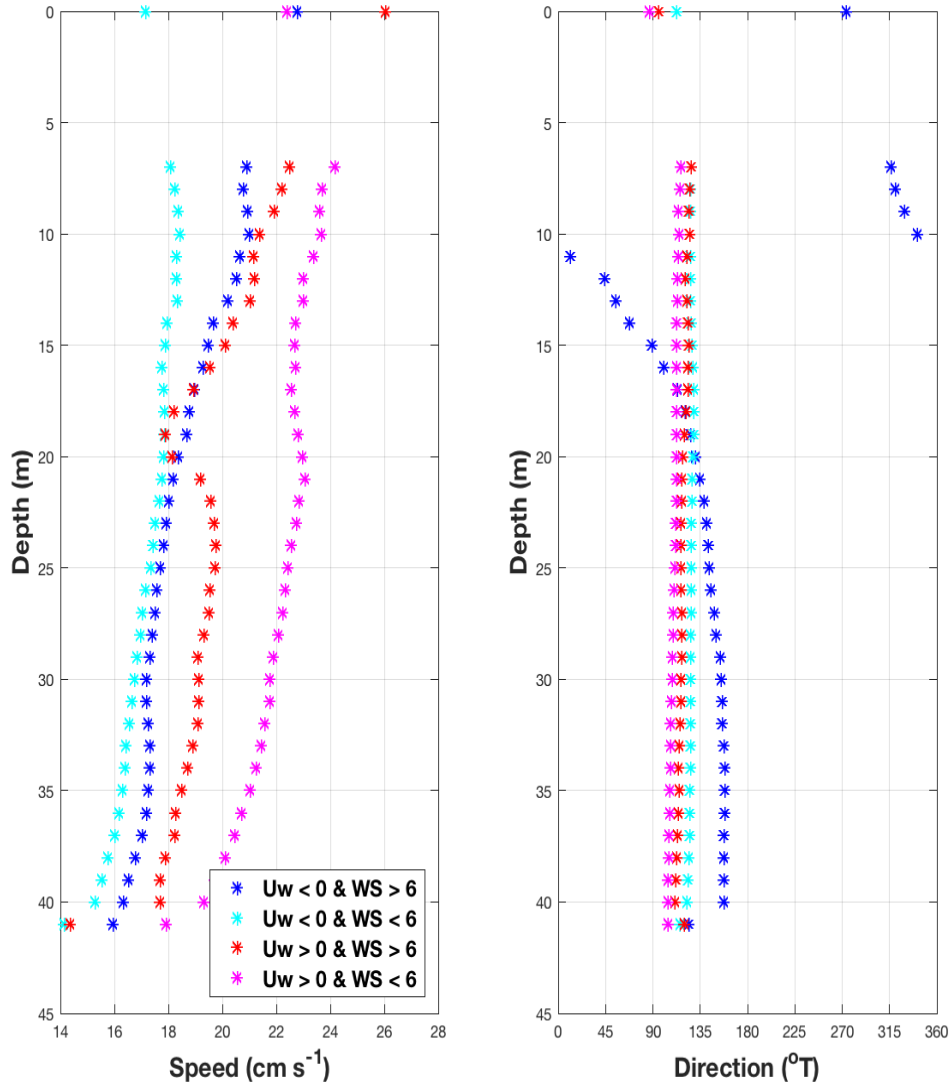


Figure 31: Mooring BC6 vertical shear in speed (left) and direction (right) from surface (HFR) and subsurface (ADCP) data based on the four wind speed (WS) and direction criteria shown in the legend. The wind component,  $U_w$ , represents the component aligned with the principal axis of variation.

Near the shelf break in the Beaufort Sea, mooring SBN data (Figure 32) show that the current direction as a whole is very sensitive to the wind direction and that upper water column shear is near nonexistent for  $U_w < 0$ . For  $U_w > 0$ , the surface current direction at this site is not well representative of the flow direction here sub-surface. In all wind cases, the surface flows at SBN are stronger than those found at depth.

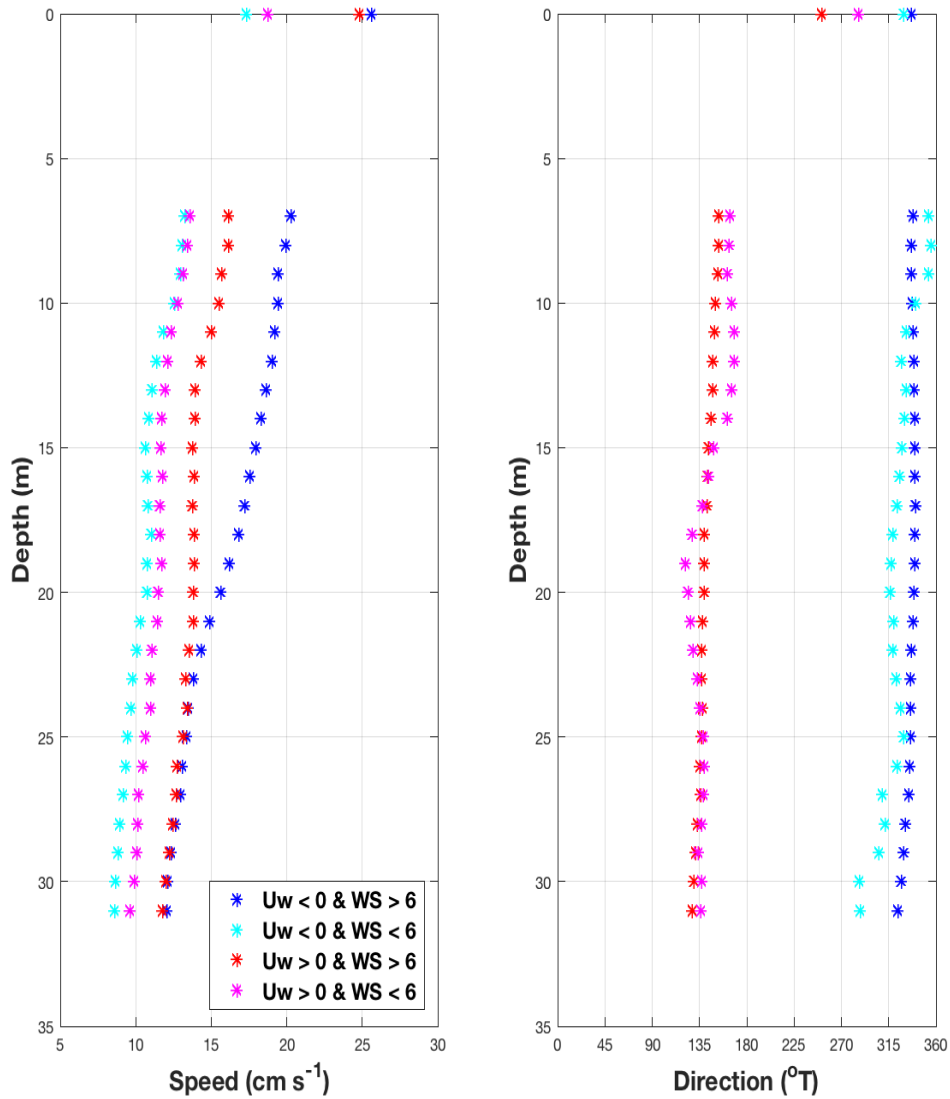


Figure 32: Mooring SBN vertical shear in speed (left) and direction (right) from surface (HFR) and subsurface (ADCP) data based on the four wind speed (WS) and direction criteria are shown in the legend. The wind component,  $U_w$ , represents the component aligned with the principal axis of variation.

North of Hanna Shoal, the currents at HNSE50 (Figure 33) and HSNE60 (not shown) reveal a strongly sheared upper water column in the presence of  $WS > 6 \text{ m s}^{-1}$ . For  $U_w < 0$  and  $WS > 6 \text{ m s}^{-1}$ , the upper water column is primarily sheared in direction, with currents below 15 m depth aligned ( $\sim 140 - 180^\circ\text{T}$ ) for all wind cases but with the 0 – 12 m depth currents oriented toward  $270 - 315^\circ\text{T}$ .

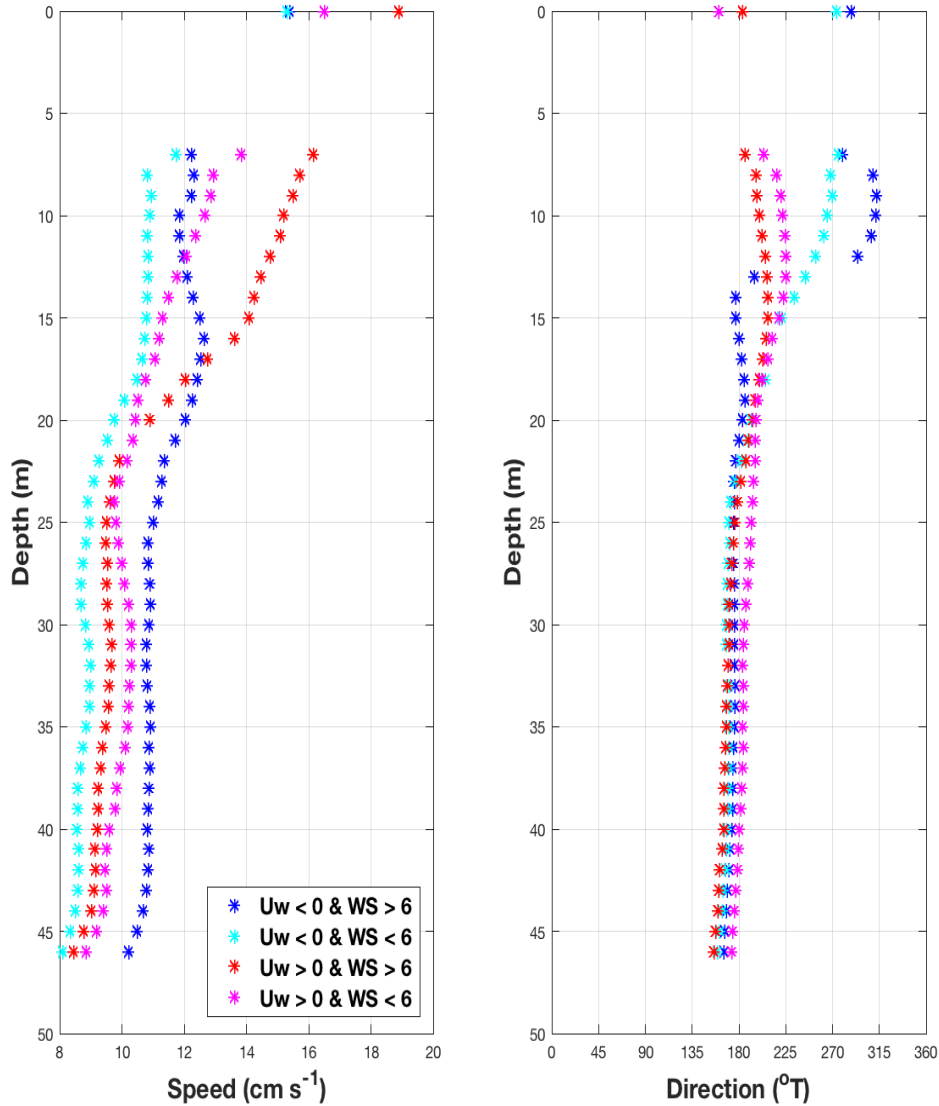


Figure 33: Mooring HSNE50 vertical shear in speed (left) and direction (right) from surface (HFR) and subsurface (ADCP) data based on the four wind speed (WS) and direction criteria are shown in the legend. The wind component,  $U_w$ , represents the component aligned with the principal axis of variation.

We also find that the character of the speed shear profile changes at some locations depending on the relative orientation of the winds and currents. For example, at BC2 (Figure 34) the shear of the mean speed for the four  $WS > 6 \text{ m s}^{-1}$  and  $U_w < 0$  cases  $90 \ll 180$ ,  $-180 \ll -90$ ,  $0 \ll 90$ , and  $-90 \ll 0$  is about 35, 45, 55 and 65  $\text{cm s}^{-1}$ , respectively. However, when  $WS > 6 \text{ m s}^{-1}$  and  $U_w > 0$ , the  $-180 \ll -90$  case shows a mean speed of about 25  $\text{cm s}^{-1}$ , while the other three cases all have notably stronger speeds of  $\sim 50 - 60 \text{ cm s}^{-1}$ .

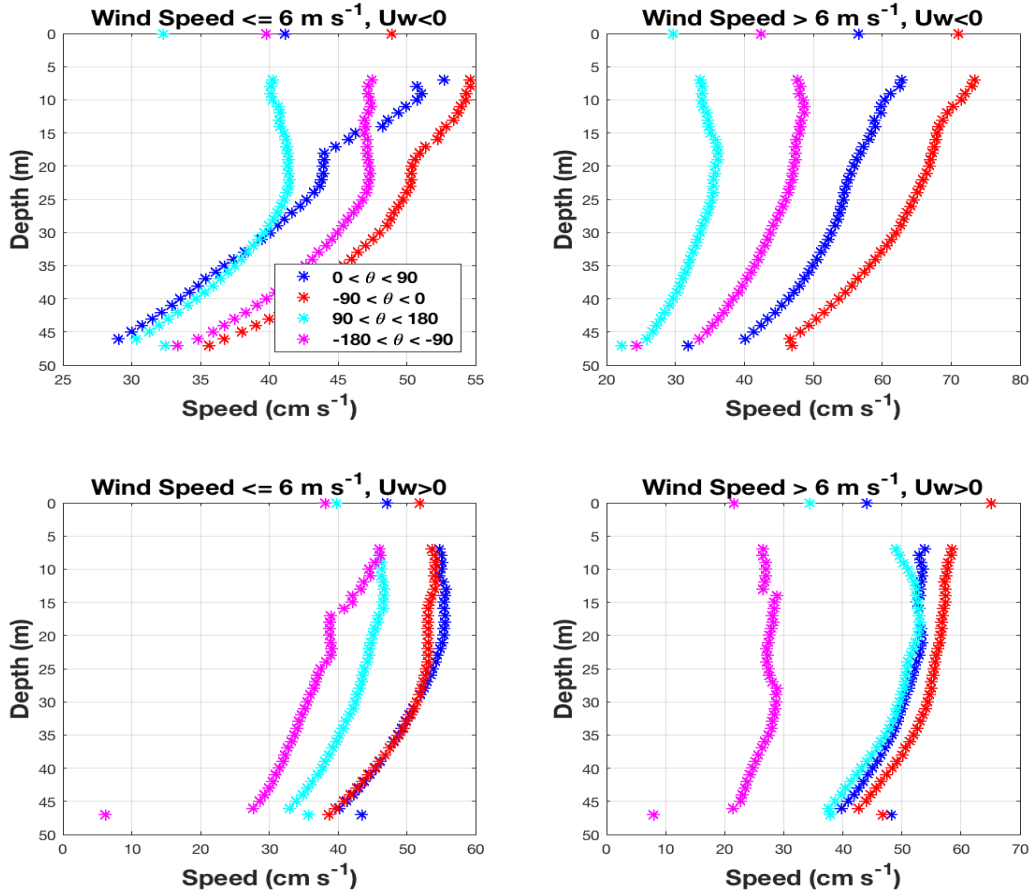


Figure 34: Water speed shear profiles at mooring BC2 under conditions of the angle between the winds and the surface currents as noted in the color legend: blue =  $0 < \theta < 90$ ; red =  $-90 < \theta < 0$ ; cyan =  $90 < \theta < 180$ ; magenta =  $-180 < \theta < -90$ . Upper left panel shows the shear profiles for wind speed  $\leq 6 \text{ m s}^{-1}$  and  $U_w < 0$ ; upper right panel shows the shear profiles for wind speed  $> 6 \text{ m s}^{-1}$  and  $U_w < 0$ ; lower left panel shows the shear profiles for wind speed  $\leq 6 \text{ m s}^{-1}$  and  $U_w > 0$ ; lower right panel shows the shear profiles for wind speed  $> 6 \text{ m s}^{-1}$  and  $U_w > 0$ .

Examination of the shape of the water speed shear profile (Figures 35) reveals that, for most sites, positive shear profiles (i.e., where the surface flow is larger in magnitude than the subsurface flow) are nearly always associated with smaller water column mean speeds. In contrast, negative shears close to the surface are associated with larger water column mean current speeds. Combining all mooring sites (Figure 36) shows a sizeable difference in the surface speeds between the two cases, while the mean shear profiles sit at the edge of the 95% confidence limits for that of the alternate phase shear condition.

Prior studies show that vertical shear on the Chukchi shelf varies spatially (Weingartner et al., 2013) and may be due to a combination of effects that include the proximity to the Chukchi Slope current, cross-shelf density gradients, and wind (Fang et al., 2020). Topographic effects such as convergence of  $f/h$  contours ( $h$  = water depth) may also play a role in regulating the scattering of topographic waves into higher mode fluctuations.

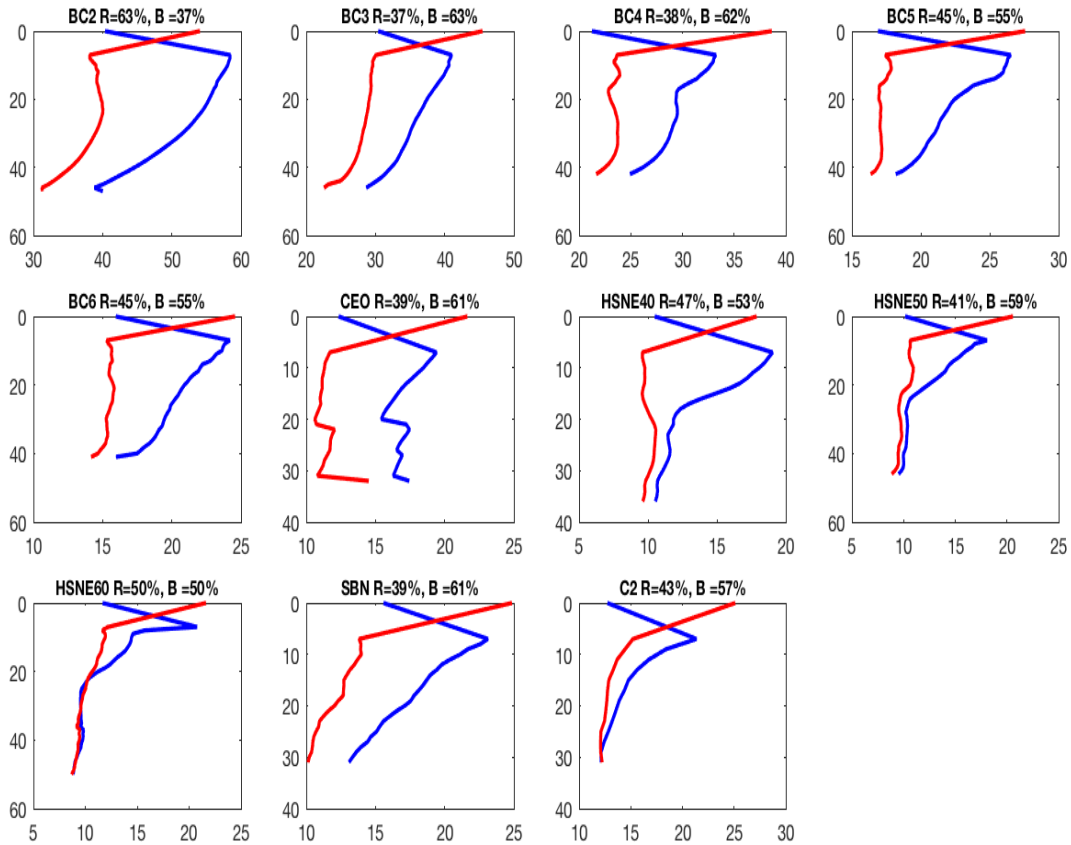


Figure 35: Profiles of water column shear separated by the sign of the near-surface shear, based on the slope of the shear profile between the HFR data at the surface and the first good ADCP data point below the surface. The profiles are shown with negative (blue) and positive (red) shear profiles. Each panel is labeled with the mooring site name and the percentage of time that the site experienced each near-surface shear condition. Only moorings with full resolution 1 m vertical bin spacing are shown here.

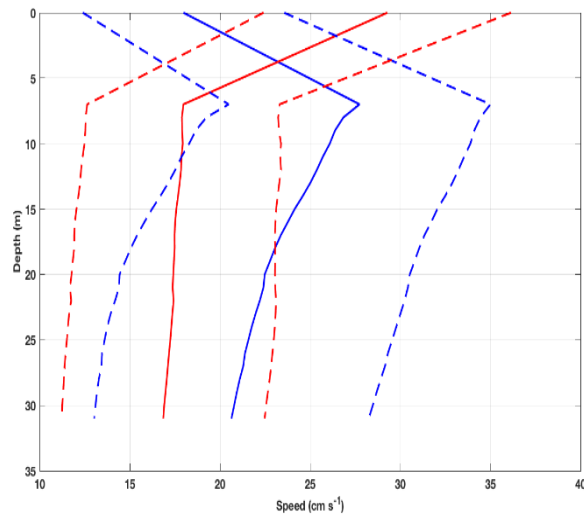


Figure 36: Mean vertical profile of current speeds (solid lines) across all moorings based on positive (red) and negative (blue) shears between the surface HFR current and the closest-to-surface ADCP current. On either side of the mean profiles, 95% confidence limits are shown with dashed lines. Based on the profiles shown in Figure 35.

### 3.5 The Lagrangian Flow Field

Two clusters of satellite-tracked drifters having subsurface (30 m depth) drogues passed through the HFR coverage mask from late August to early November 2013 and in August 2015 (Figure 10). One such drifter trajectory is shown in Figure 37 (lower right panel). In each deployment year, a cluster of drifters transited through Barrow Canyon within a few days of each other. Although most drifters showed a relatively small fraction of total overlap with coincident HFR data, the temporal separation of the drifters and the similarity in their tracklines allowed us to construct a companion set of velocity estimates nearly everywhere along each of the two sets of tracklines. The data examined in this analysis is based on 6880 hours of drifter data, for which we have 1279 hours of spatially and temporally coincident HFR data.

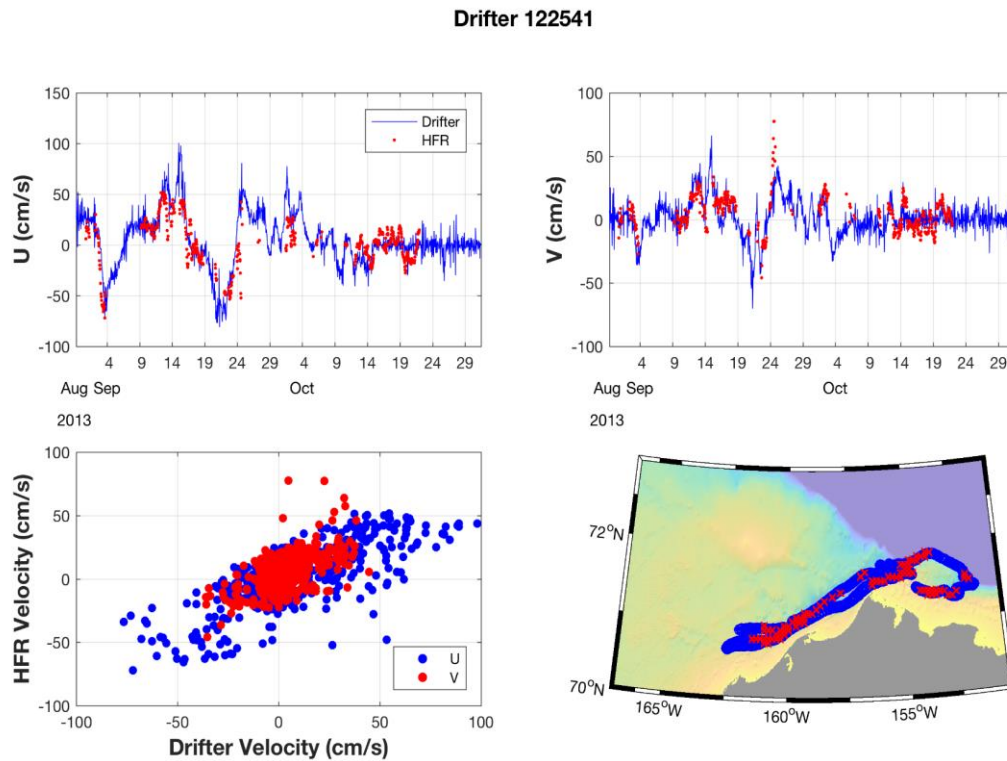


Figure 37: Comparison of data from Drifter 122541 and the HFR. The upper left and upper right panels show the U and V velocity components, respectively, with blue lines showing the drifter data and red dots showing the coincident HFR data. The lower left panel shows the scatter between the drifter and HFR data for the U (blue) and V (red) components. The lower right panel is a map showing the drifter location (blue symbols) and the location of coincident HFR data (red symbols).

The relationship between the drifter and HFR datasets (Figures 38 and 39) exhibits an average shear of about  $20 \text{ cm s}^{-1}$  with a shear standard deviation of  $13.5 \text{ cm s}^{-1}$ . For all data pairs, however, the mean velocity magnitude is indistinguishable ( $28.8 \text{ cm s}^{-1}$  for the drifters and  $27.9 \text{ cm s}^{-1}$  for the HFR), as is the standard deviation ( $21.7 \text{ cm s}^{-1}$  for the drifters and  $19.4 \text{ cm s}^{-1}$  for the HFR). These comparisons suggest that the net flow field is more sheared in direction than in magnitude. However, it also suggests that, for the purposes of tracking oil spills or other contaminants at the surface, satellite-tracked drifters with subsurface drogues at 30 m depth will provide only a rough measure of any oil speed and direction at the surface.

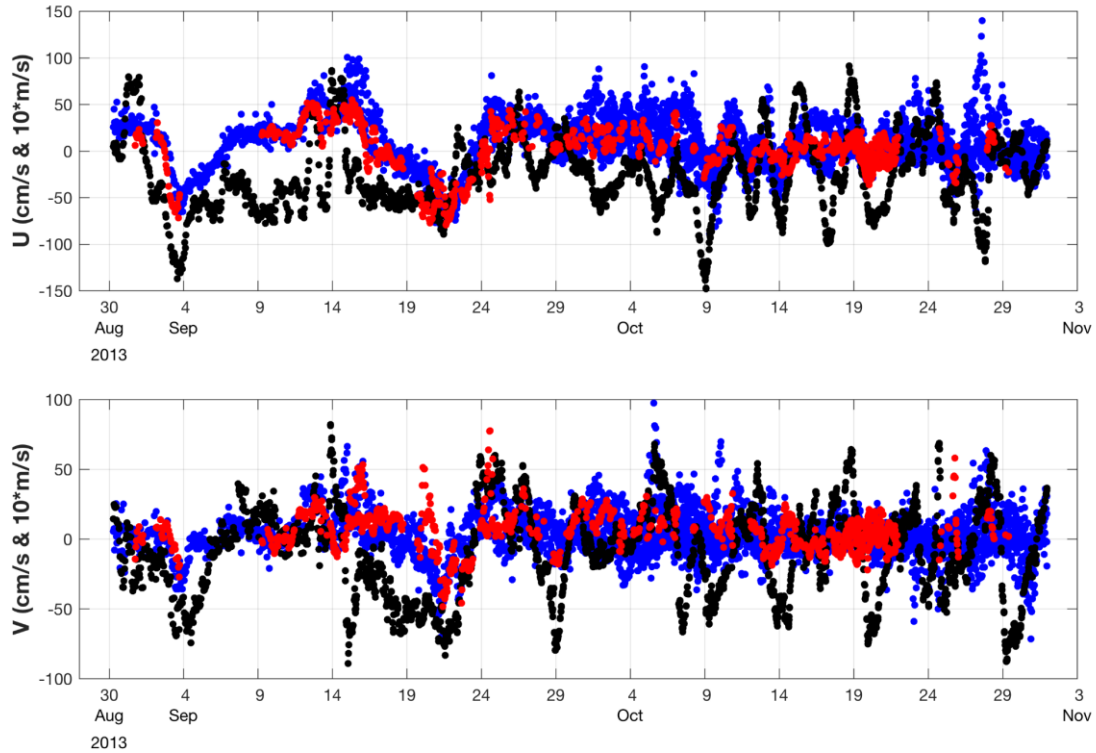


Figure 38: Time series of U (upper panel) and V (lower panel) components of the currents (drifter = blue, HFR = red) and PABR winds (black, scaled by a factor of 10). All data from the 2013 drifter deployments are plotted here.

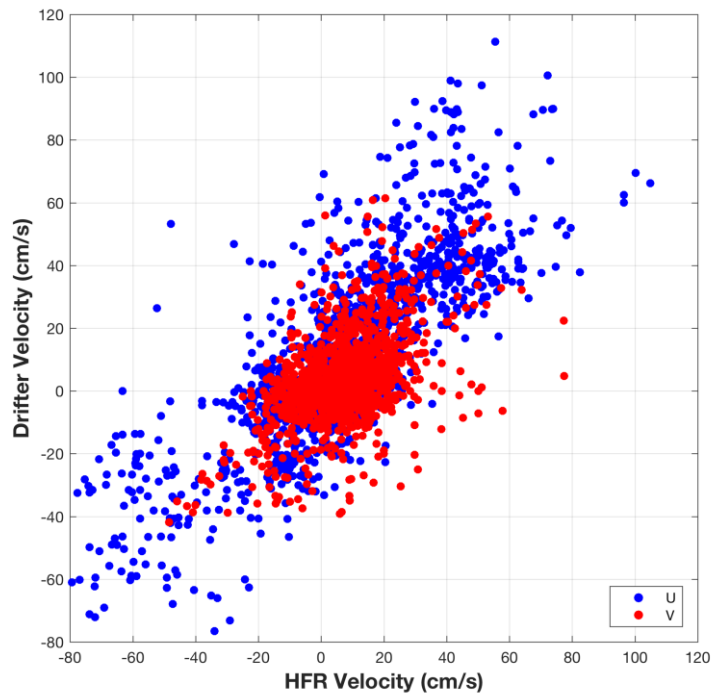


Figure 39: Scatterplot of all 1,279 drifter-HFR data pairs from the 2013 and the 2015 30 m depth drogued drifters.

### 3.6 Flow Field Case Studies

In this section, we display a series of single-day HFR averages to reduce the amount of aliasing and spatial artifacts associated with multi-day composites. These one-day snapshots of the flow field were selected in part to help show that the multi-day averages displayed in Section 3.2 are representative of the actual flow field under the influence of a system that has been given sufficient time to undergo rotational and magnitude adjustment under relatively constant forcing. We accomplish this by selecting snapshots of the flow field on the third consecutive day of having experienced winds with a similar magnitude and direction. Visual inspection confirms generally modest changes in flow field structure from the day before that shown. Figures 40 – 49 are organized sequentially by wind direction beginning with winds blowing to the east and then progressing in a clockwise fashion through winds to the southeast, south, southwest, and so on.

The case with winds having modest strength and blowing eastward (Figure 40) shows a well-developed ACC entering Barrow Canyon, a reversal (eastward currents) of the inner Beaufort shelf flow, and a bifurcation of the flow where the upper slope (60 – 100 m depths) turns from a southwest-northeast orientation to a northwest-southeast orientation. The westward branch of the bifurcation is directed along-isobath toward the northwest. In this case, currents near 148.5°W and north of 71.5°N are oriented to the west, possibly as an on-shelf extension of the Chukchi Slope current.

Winds blowing to the south and southeast (Figure 41) appear to retard the ACC and reverse the flow in the Beaufort, in lower Barrow Canyon, and over the easternmost extent of the Chukchi shelf. The flow diverges as it rounds the eastern side of the mouth of Barrow Canyon, and at the mouth of the canyon, the flow's positive vorticity carries it to the northwest.

A similar current regime is shown over the Chukchi Sea in the case of winds blowing to the south and southwest (Figures 42 and 43). The entire flow field in the Chukchi Sea reverses, and nearshore flow in the Beaufort is oriented to the west. Strong divergences over the western Beaufort and western side of the lower canyon are separated by a zone of convergent flow at the mouth of the canyon. The flow in the Chukchi exhibits primarily negative vorticity, while the vorticity in lower Barrow Canyon shows patterns that appear to be strongly regulated by the underlying bathymetry.

The flow pattern of Figure 43, which appears commonly through the record, depicts an anticyclonic gyre that straddles the western Beaufort shelf and continental slope region. The gyre naturally exhibits negative vorticity, which is consistent with the tendency for anticyclonic motion as the onshore leg of the gyre progresses into shallower water. Where the gyre crosses back into deeper waters at the mouth of Barrow Canyon, the flow becomes strongly divergent. This pattern closely mirrors the long-term mean flow field map shown in Figure 12. The flow field to the east of Hanna Shoal is directed to the northwest.

Under the influence of modestly strong winds with a westward orientation (Figure 44), the ACC does not reverse (the Ekman transport is northward), and the gyre shown in Figure 43 persists. But under stronger westward-blowing winds (Figure 45), the gyre disappears within the data coverage region, and the flow across the western Beaufort shelf is to the west before turning northward as it enters Barrow Canyon.

Winds directed to the northwest are relatively infrequent, but modest strength events can apparently disrupt the western Beaufort shelf-slope gyre (Figure 46). The Ekman component of this flow enhances the ACC down Barrow Canyon, while the current vectors over the western Beaufort are oriented to the north and northwest. Northward winds are similarly uncommon, but even relatively modest strength

winds in this orientation direct the Beaufort inner shelf water cross-isobath offshore and, in the example shown in Figure 47, a strong positive vorticity directs the flow into the mouth of Barrow Canyon. In this example, the Barrow Canyon flow is opposite (directed toward each other) at either end of the canyon. Clearly, this situation cannot be a steady-state representation without some third dimension of the flow field, such as water mass subduction.

A mid-canyon convergent flow is also depicted in Figure 48, with modest winds blowing mostly toward the east-northeast. In this case, an eastward-deflected jet enters the western Beaufort directly from Barrow Canyon. This is an example of the western Beaufort shelf gyre reversing so that it exhibits a cyclonic sense of rotation. With somewhat stronger winds in a similar direction, Figure 49 shows a similar cyclonic structure, although the Barrow Canyon flow remains directed toward the Canada basin, resulting in a strong convergence on the western flank of the gyre. The flow heading across-shelf toward the small canyon at 153°W is oriented to the left of the PABR wind vector.

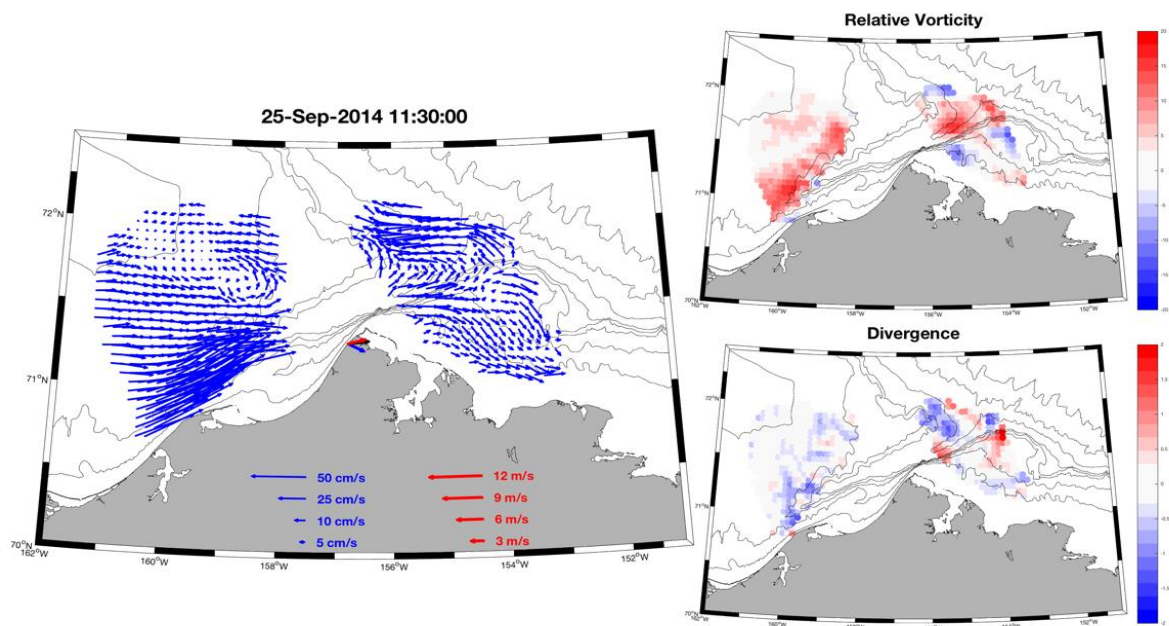


Figure 40: One-day average flow field maps of the currents (left), relative vorticity (upper right), and divergence fields (lower right). The three wind vectors shown at Utqiagvik display the mean daily wind vector for the displayed date (red), the prior day (black), and two days prior (blue).

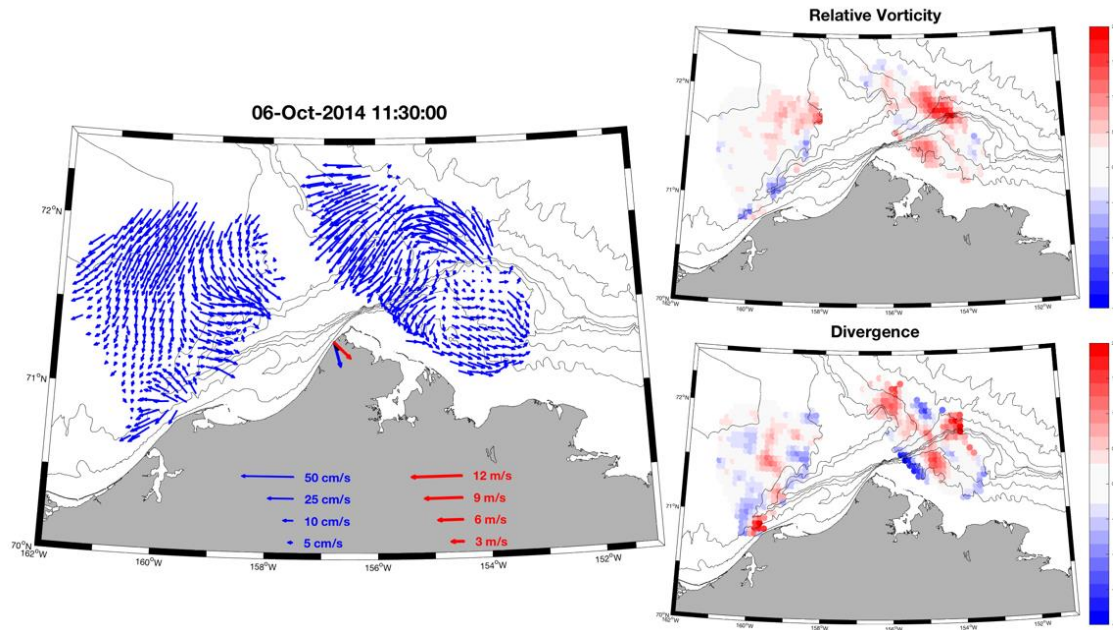


Figure 41: One-day average flow field maps of the currents (left), relative vorticity (upper right,) and divergence fields (lower right). The three wind vectors shown at Utqiagvik display the mean daily wind vector for the displayed date (red), the prior day (black), and two days prior (blue).

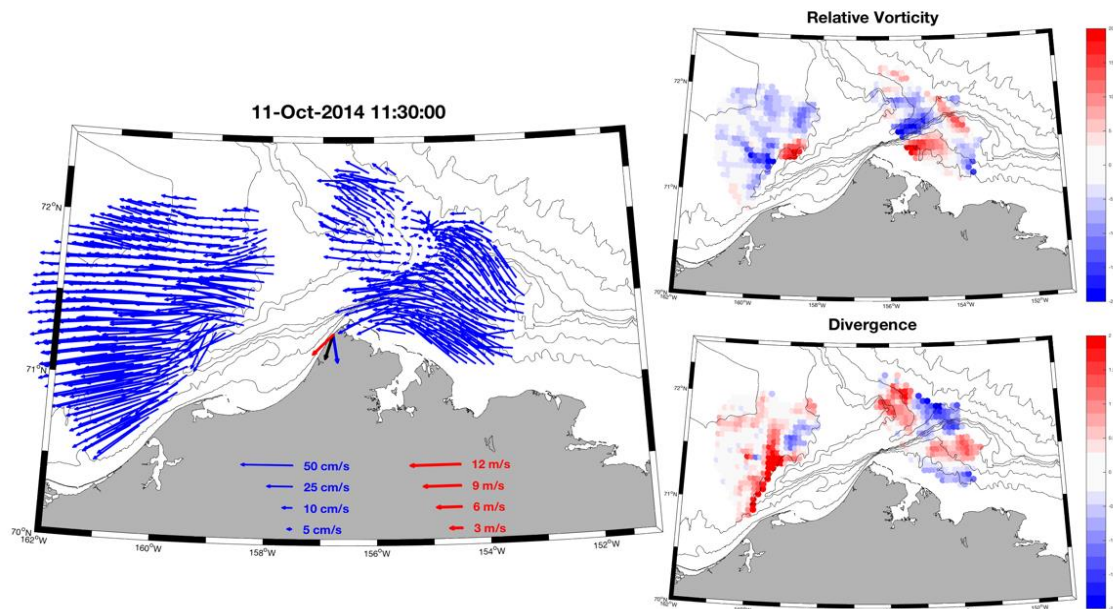


Figure 42: One-day average flow field maps of the currents (left), relative vorticity (upper right,) and divergence fields (lower right). The three wind vectors shown at Utqiagvik display the mean daily wind vector for the displayed date (red), the prior day (black), and two days prior (blue).

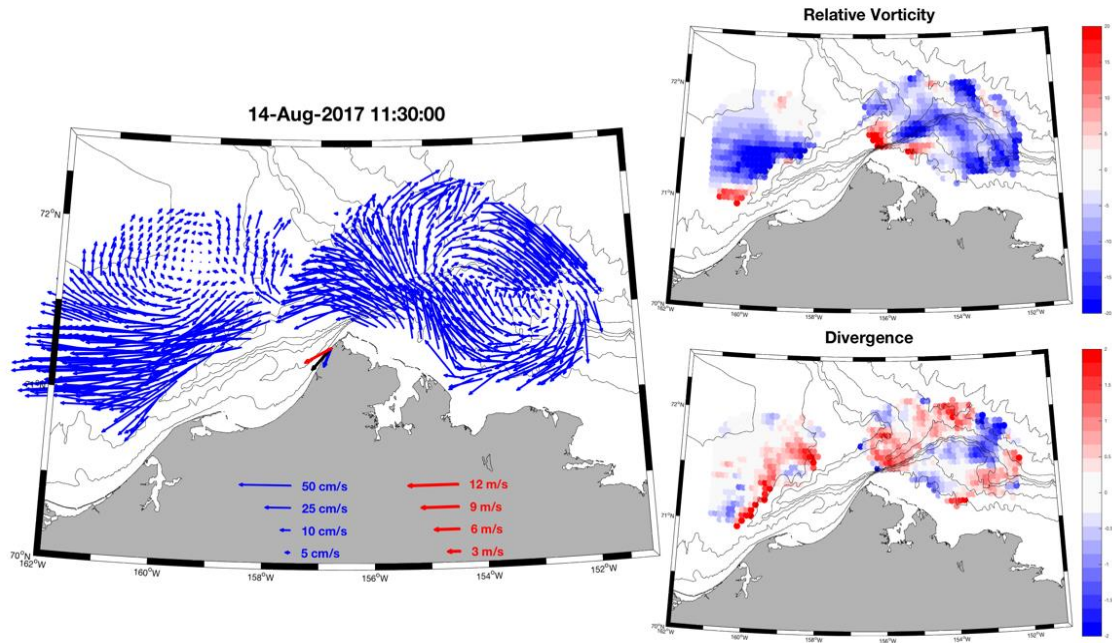


Figure 43: One-day average flow field maps of the currents (left), relative vorticity (upper right), and divergence fields (lower right). The three wind vectors shown at Utqiagvik display the mean daily wind vector for the displayed date (red), the prior day (black), and two days prior (blue).

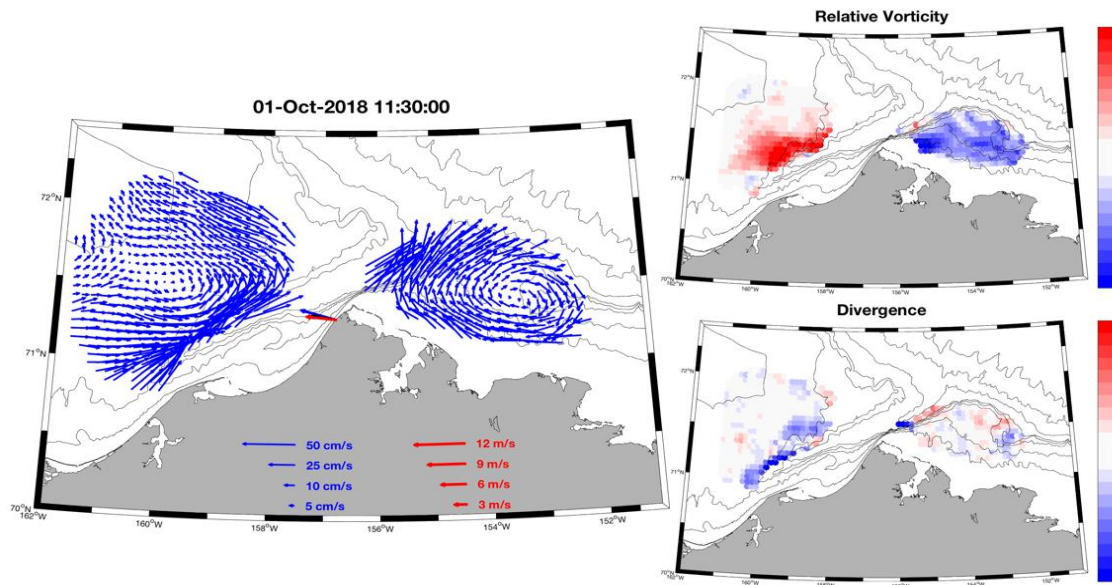


Figure 44: One-day average flow field maps of the currents (left), relative vorticity (upper right), and divergence fields (lower right). The three wind vectors shown at Utqiagvik display the mean daily wind vector for the displayed date (red), the prior day (black), and two days prior (blue).

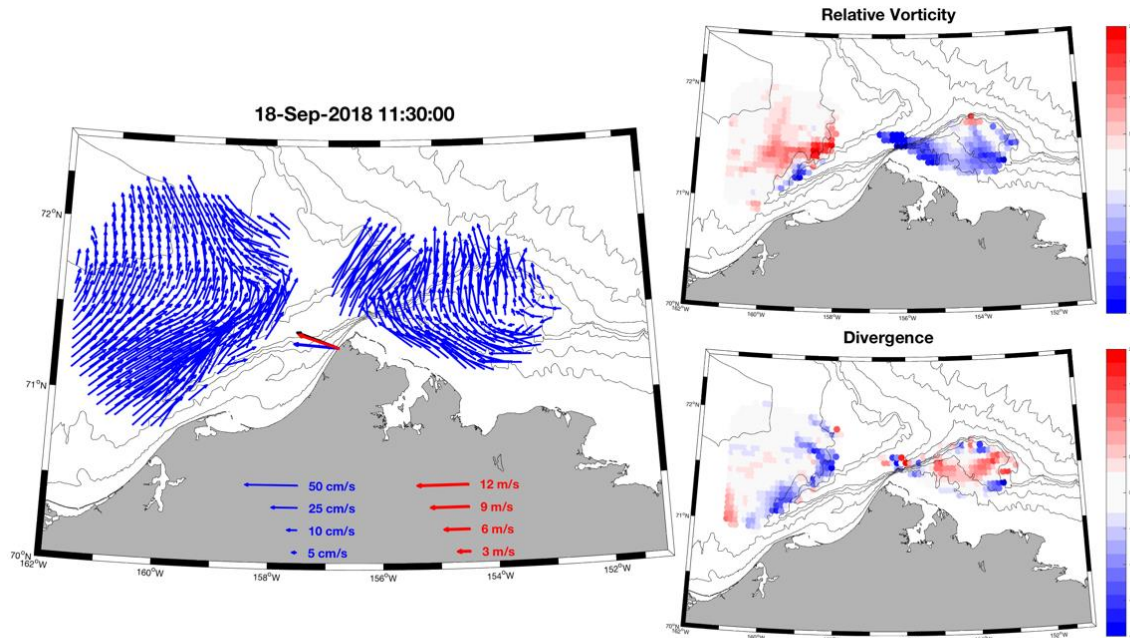


Figure 45: One-day average flow field maps of the currents (left), relative vorticity (upper right,) and divergence fields (lower right). The three wind vectors shown at Utqiagvik display the mean daily wind vector for the displayed date (red), the prior day (black), and two days prior (blue).

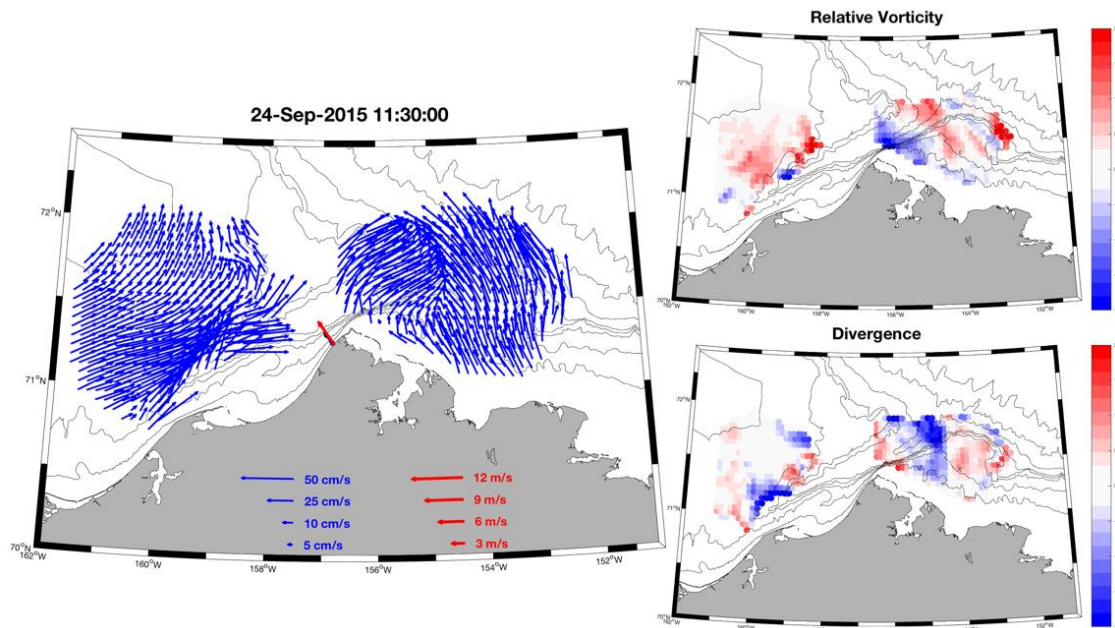


Figure 46: One-day average flow field maps of the currents (left), relative vorticity (upper right,) and divergence fields (lower right). The three wind vectors shown at Utqiagvik display the mean daily wind vector for the displayed date (red), the prior day (black), and two days prior (blue).

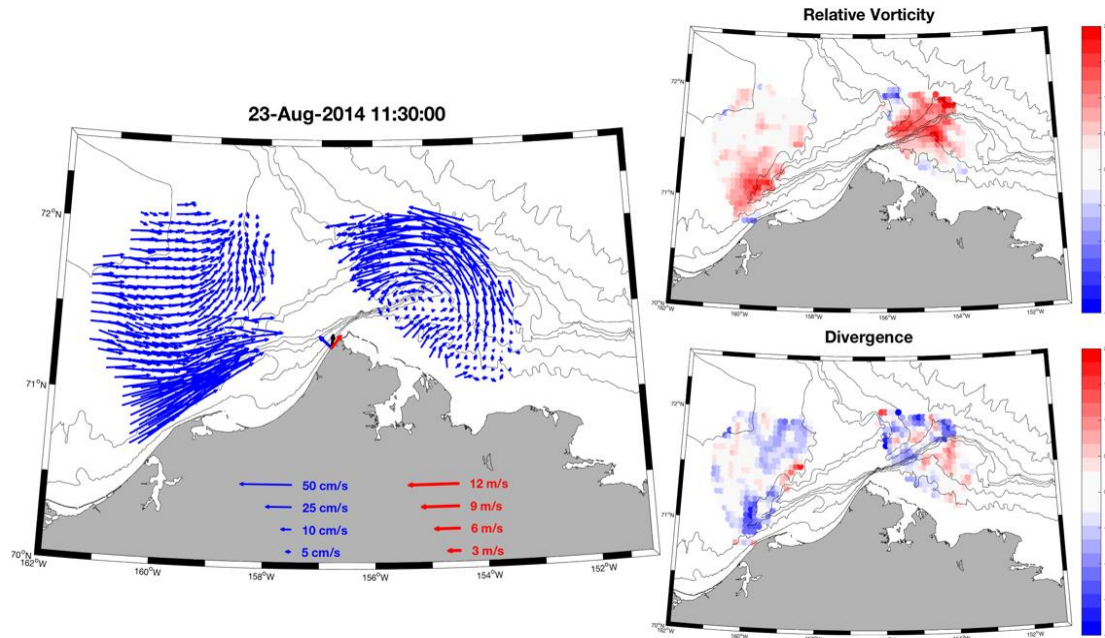


Figure 47: One-day average flow field maps of the currents (left), relative vorticity (upper right), and divergence fields (lower right). The three wind vectors shown at Utqiagvik display the mean daily wind vector for the displayed date (red), the prior day (black), and two days prior (blue).

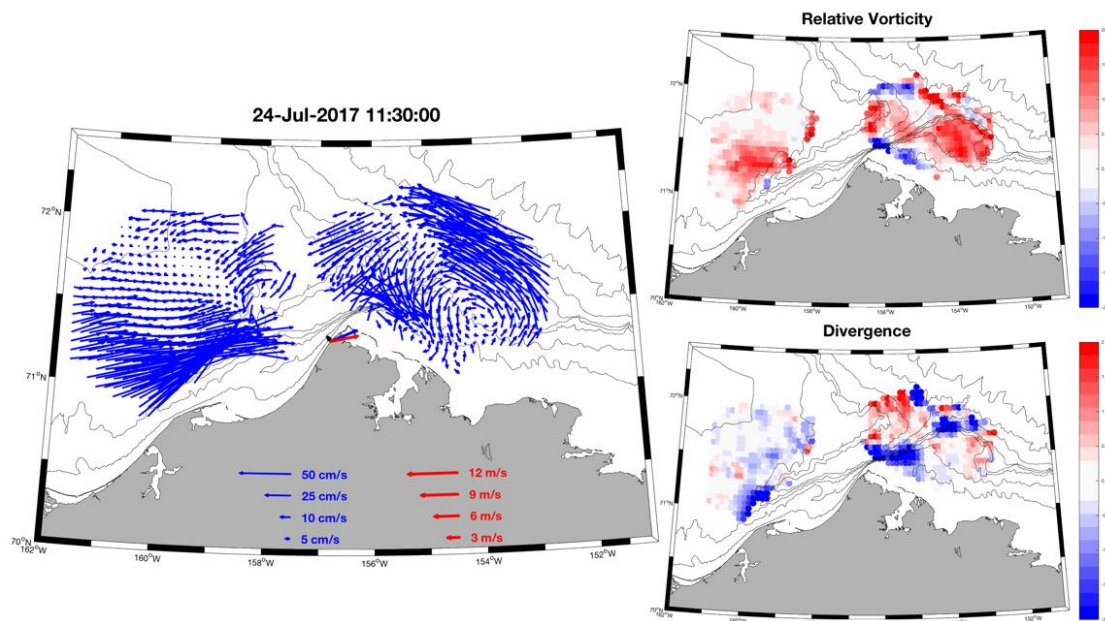


Figure 48: One-day average flow field maps of the currents (left), relative vorticity (upper right), and divergence fields (lower right). The three wind vectors shown at Utqiagvik display the mean daily wind vector for the displayed date (red), the prior day (black), and two days prior (blue).

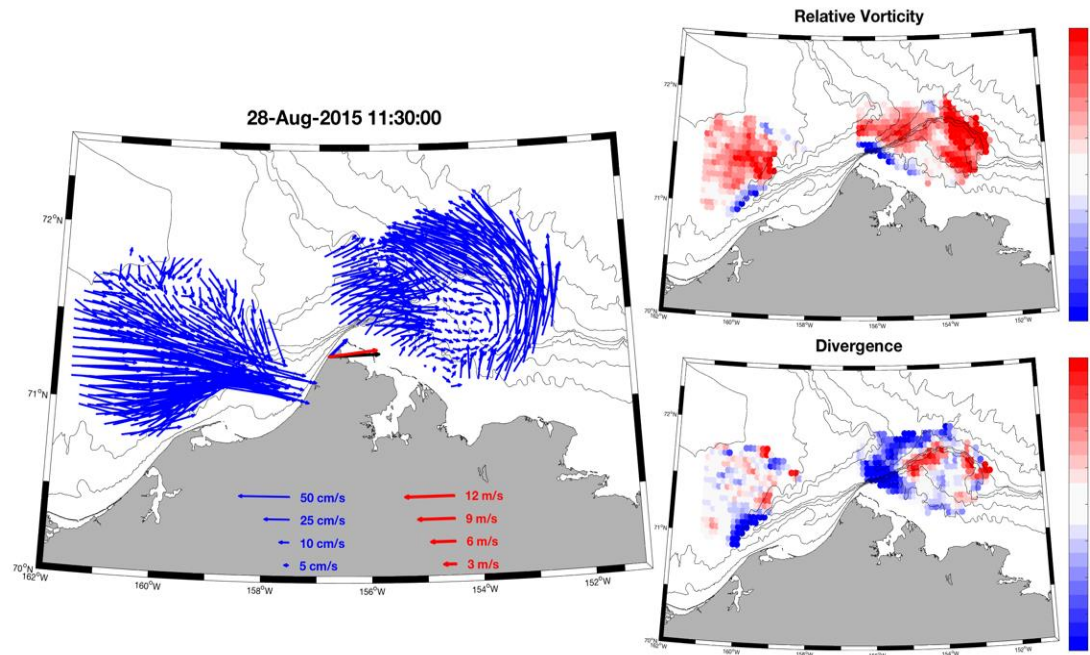


Figure 49: One-day average flow field maps of the currents (left), relative vorticity (upper right), and divergence fields (lower right). The three wind vectors shown at Utqiagvik display the mean daily wind vector for the displayed date (red), the prior day (black), and two days prior (blue).

## 4.0 Discussion

Our analysis of the surface flow field provides insight into the fine-scale spatial structure and temporal variability of the currents that exist at the junction between the U.S. Chukchi and Beaufort Seas. Although the HFR data reflect surface conditions only, comparison with available current velocity profiles shows that the surface conditions are generally representative of sub-surface conditions, although there often exists shear (speed and/or direction) in the upper 10 m of the water column that is controlled by the wind speed and direction relative to the underlying oceanic flow speed and direction.

### 4.1 Flow Field Structure

Taken together, the four composites based on strong winds ( $> 6 \text{ m s}^{-1}$  daily average; Figures 18 – 21) depict a wind forced surface current system that spends considerable time alternating between contrasting flow regimes. Portions of these regimes have not been previously described in the scientific literature with such spatial resolution, and thus our study represents a newly updated understanding of flow pathways across this region. Other portions are well documented, such as reversals of the Barrow Canyon flow (Weingartner et al., 2017a) and the eastward intrusion of ACC waters onto the western Beaufort shelf under the influence of eastward winds (Okkonen et al, 2009).

The strong wind days represent conditions in 132/362 of the sampled days (36%). Another 130/362 days (36%) are spent under the influence of weak to modest wind forcing ( $< 4 \text{ m s}^{-1}$ ). The flow field in this portion of the time is less energetic as a rule, and the patterns of the flow in these conditions have only modest dependence on the wind speed and direction. The flow field associated with weak wind forcing is structurally similar to the overall mean (Figure 12) but somewhat less energetic.

The HFR data allow us to resolve features in the flow field that are not attainable by other methods. The spatially high-resolution ( $\sim 6 \text{ km}$ ) nature of the data permits computation of the surface vorticity field which enables interpretation of flow dynamics beyond speed, direction, and pathway analyses. In particular, our maps showing the surface flow field divergence and vorticity fields are rich in structural detail and they highlight key locations of interest: the intersection of the U.S. Chukchi and Beaufort coastal flows in Barrow Canyon; the minor canyon near  $153^\circ\text{W}$  and the shelf region immediately west in the Beaufort Sea; and the slope bathymetry geometry and its intersection with Barrow Canyon.

The band of negative relative vorticity that stretches from the shelf break to the inner Beaufort shelf (Figure 17) suggests that this flow pathway may be controlled by vorticity dynamics (in addition to the time-varying influence of the winds). In general, negative relative vorticity is consistent with water column shrinkage and divergence, which is consistent with an on-shelf flow over the shoaling bathymetry. Such a flow field may exert strong influence over the upward and on-shelf advection of subsurface passively drifting plankton constituents (e.g., zooplankton – bowhead whale prey) and water (e.g., nutrients that fuel phytoplankton growth). We speculate that this vorticity balance could be a biologically important component and control of the local ecosystem.

The relationship between the near-surface shear and the shape and magnitude of the subsurface current speed profile (e.g., Figure 36) reveals key aspects of the nature of the flow field vertically and, potentially, the relationship between the currents and the wind. It appears that one may be able to deduce the structure of the water column currents simply by knowing the relative orientation between the wind and the mean water column flow direction. This understanding could inform the assessment and interpretation of ocean current structure during oil spill response efforts. For example, information from

low-cost oceanographic drifters and in-situ wind measurements may, together, be enough to meaningfully inform predictions of the subsurface flow field.

Near the edges of the HFR data grid, some features in the mean and composite surface flow field maps are likely a result of the daily-varying grid coverage and may not reflect the intended long-term mean for the associated conditions. For example, on the continental slope and east of the mouth of Barrow Canyon in the grand mean flow map, there exists a flow field component that is directed southeastward. This feature only showed up in the 2017 average flow field because the instruments had a particularly good offshore coverage that year. However, with relatively few days of data, this region should not be considered representative of the long-term mean. Nonetheless, the similarity between the snapshot case studies shown in Section 3.5 and the average flows shown in Figures 18 – 21 provide reassurance that these average fields are reasonable.

Presumably, a large portion of the flow continues past the gyre along the shelf break, forming the Beaufort extension of the ACC that comprises the Beaufort Jet in the summer months. We note that, despite the clear influence of the wind on these flow patterns shown in Figures 40 – 49, the relationship cannot be described by a simple Ekman forcing scenario. This means that simple wind speed and direction estimates of surface drift and oil trajectories may not be reliable across our study region.

We speculate that the formation of the Chukchi Slope current may depend, in part, on flow convergence within Barrow Canyon. The Beaufort Sea's westward-directed coastal flow could, at times, deflect the along-canyon flow over to the northern wall of the canyon. Should this occur, this flow will seek to maintain geostrophic balance and may follow the bathymetric contours that bend to the northwest and become the Chukchi Slope current (Corlett and Pickart, 2017). In the absence of a westward flowing coastal current in the Beaufort Sea, the Barrow Canyon outflow will feel the southern wall of the canyon more strongly and seek to turn eastward at the mouth of the canyon.

Despite the above caveats and other unknown factors, we can suggest an updated flow schematic for the study region (Figure 50). This map depicts the following key features:

1. Convergent flow of the ACC into the head of Barrow Canyon from the west and southwest.
2. A portion of the flow through Barrow Canyon is directed northwestward along the Chukchi slope.
3. Another portion of the flow through Barrow Canyon follows the shelf break bathymetry around the northernmost extension of the Beaufort Sea, which forms the eastern side of Barrow Canyon's mouth. The offshore part of this flow likely continues along the Beaufort slope to the southeast, but another portion tends to flow onto the western Beaufort shelf, forming the offshore branch of an anticyclonic gyre, and feeding the Beaufort coastal flow.

According to our SOM analysis, the anticyclonic gyre is present at least 30% of the time. In its normal rotational orientation, it appears to be a consequence of the mean Alaska Coastal Current flow (on its western and northern boundaries), a wind-driven component (on its eastern boundary), and the coastal constraint (on its southern boundary). The gyre's anticyclonic vorticity is compatible with the southward cross-shelf shoaling of water depths. In the mean, the Beaufort coastal flow is directed westward and upon reaching Barrow Canyon it crosses isobaths to converge with the ACC in Barrow Canyon. We hypothesize that, at times, this westward flow from the Beaufort into Barrow Canyon may deflect the ACC against the northern wall of Barrow Canyon. This mechanism may be partially responsible for determining the westward or eastward fate of water parcels transiting Barrow Canyon.

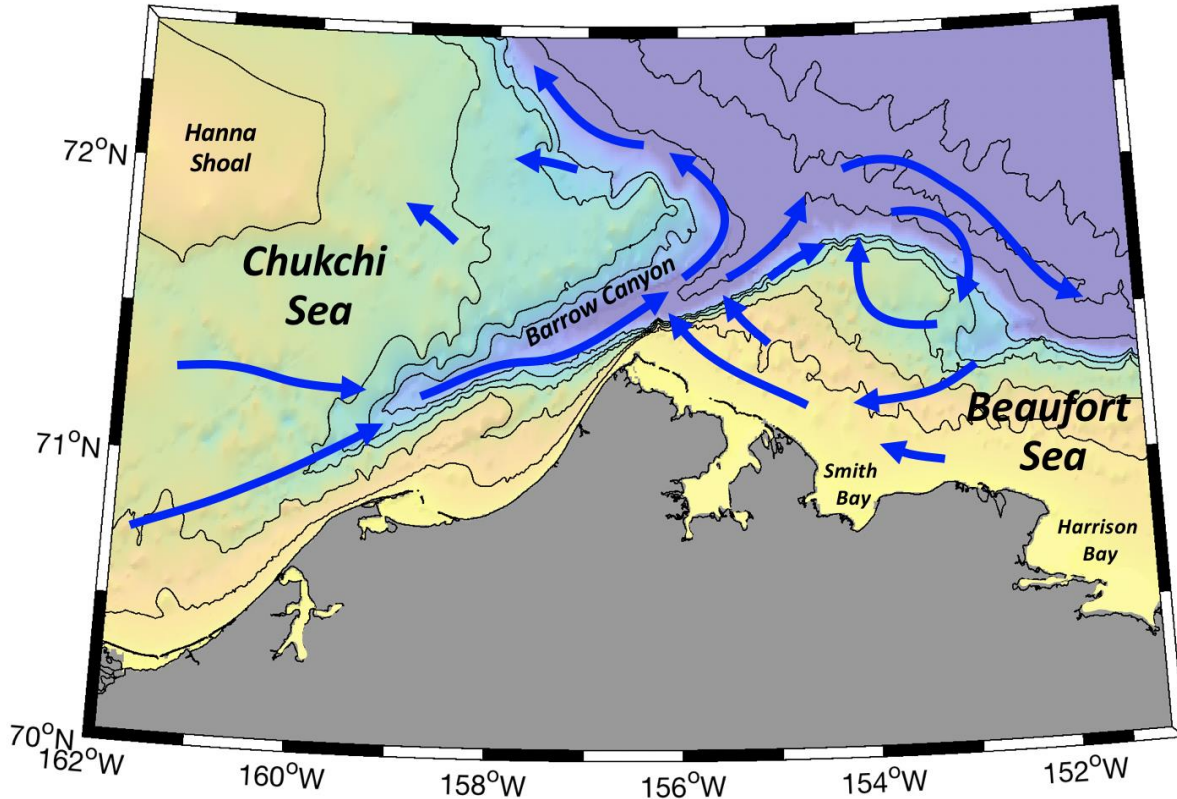


Figure 50: Map depicting an idealized rendering of the typical surface currents in the study region.

#### 4.2 Ecological Importance

The advection patterns depicted by the identified flow regimes exert dominant synoptic-scale control over the advection of plankton, oil, nutrients, and other important water-borne biotic and abiotic constituents. We note that the subsistence whaling communities of Utqiagvik and Wainwright are located adjacent to zones of strong convergence (Figure 16). Convergent flow fields can aggregate zooplankton like euphausiids and copepods, which are key prey items for bowhead whales. The existence of flow convergence in the vicinity of these villages is not new knowledge, but the HFR data provide a more detailed map of its spatial structure than has been available before now.

The flow fields also depict pathways that plankton and other materials follow as they are advected across the continental shelves, through Barrow Canyon, and along the continental slopes. We identify a recurring region of flow that is directed from the Beaufort slope to the inner shelf, where the flow then turns westward and converges with the currents in Barrow Canyon. In addition to the zooplankton that may be carried by this flow, it also represents a potential source of nutrients that could fuel primary productivity over the inner continental shelf.

Wind-driven upwelling and then the alteration of wind direction in the Barrow Canyon region is known to advect and then retain zooplankton in concentrated patches that are targeted by feeding whales (Ashjian et al., 2010; Okkonen et al., 2011). The HFR data may provide a means to better define the characteristics of the water motions and zooplankton movements.

## 5.0 Conclusions

This study analyzed a six-year open water season surface current dataset. Our aggregated results depict a complex flow field in the vicinity of Barrow Canyon, but the complexity can be understood, in part, in terms of time-varying adjustments to the local wind field. We identify a recurrent anticyclonic gyre that straddles the northwestern Beaufort continental shelf and slope. While the gyre typically circulates in a clockwise fashion, winds from the south and southwest can reverse the sense of rotation. In its normal orientation, the eastern leg of the gyre tends to advect water from the slope region toward the inner portion of the Beaufort shelf. The western leg of the gyre directs waters off-shelf.

The flow field maps reveal key locations where flow convergences, divergences, and changing vorticities hint at the dynamics that provide regulation of the flow field. Portions of our results need verification by future research and require additional analyses to fully reveal the dynamical importance of notable features and characteristics such as zones of persistent divergence and vorticity adjustments. These results can improve our understanding of ecosystem dynamics, bowhead whale foraging behaviors, oil spill trajectory calculations, sea ice melt patterns, and tracking of other water-borne constituents and items.

### 5.1 Recommendations

In addition to the oceanographic processes described herein, our results suggest additional research directions to further understanding of the study region flow field and its role in factors that are important for federal management considerations. Such considerations include contaminant response and tracking, critical habitat monitoring, and assessing the population status of many marine species. Hence, we provide the following recommendations:

1. Improve our understanding of the flow convergences, vorticity dynamics, and cross-isobath exchanges on the western Beaufort Sea shelf and in the lower reaches of Barrow Canyon. To our knowledge, only the SBN mooring provides a year-round record of water column flow below the western Beaufort gyre. The results of this study suggest a region of complex flow that promotes both off-shelf and on-shelf exchanges and that dominates over simple wind forced motions. An array of current meter moorings at select sites across the study region would be able to provide a better understanding of the sub-surface structure of the gyre systems and other flow pathways that provide connectivity between the shelf break and the inner shelf.
2. Integrate the new findings into a broader picture view of the U.S. Chukchi-Beaufort shelf circulation. With the high-resolution depiction of the surface currents that this study has afforded, we are now well-positioned to incorporate these findings into a broader regional context. Identifying the pathways and fate of Pacific-origin waters is an ongoing effort that can inform regional and global scale carbon dynamics, Arctic ecosystem productivity, ocean-atmosphere heat exchanges, freshwater fluxes, and many more important high latitude processes.
3. Undertake a joint analysis of HFR data and numerical model results using existing 3D ice and ocean circulation models. Many of the complex flow features observed in the vicinity of Barrow Canyon may be reasonably well reproduced, in a statistical fashion, by high-resolution models. The numerical model hindcasts can provide a much more temporally complete record. This analysis should also include an assessment of how well the existing models reproduce the characteristics of the near-surface shears that we observe in this paper.
4. Relate the physics described here to the local ecosystem and ecosystem dynamics. Some of the features described herein may exert defining control on the character of the regional flow field and, by extension, on the nutrient pathways and uptake, timing and locations, prey aggregations, and carbon sequestration.

## **Acknowledgments**

We recognize and acknowledge the Iñupiat people upon whose traditional lands our field sites reside. In support of our research, they have graciously allowed us to utilize their coastline, which is intrinsic to the heart of their culture and livelihoods. We thank the Indigenous communities of Wainwright and Utqiagvik, as well as the Olgoonik Corporation, Ukpeagvik Iñupiat Corporation, and the North Slope Borough for their permission to allow our field research.

We appreciate the Ukpeagvik Iñupiat Corporation for supporting our logistical needs and field safety during our high-frequency radar fieldwork, and the University of Alaska Fairbanks (UAF) students and technicians who helped keep the field sites operational: Ying-Chih Fang, James Kelly, Cayman Irvine, Jordi Maisch, and especially Hank Statscewich.

We are grateful to Elizabeth Dobbins for processing and formatting mooring data. We thank the National Climate Data Center and the National Center for Environmental Information for providing access to meteorological data, as well as the creators of the Self-Organizing Map Toolbox for MATLAB: Esa Alhoniemi, Johan Himberg, Juha Parhankangas, and Juha Vesanto.

We thank multiple partners for funding field operations: the Alaska Ocean Observing System, Conoco Phillips Alaska, the National Center for Island Maritime and Extreme Environment Security, the State of Alaska Coastal Impact Assistance Program, and the North Slope Borough. We thank Shell Oil for providing match funding. We are grateful for the supplementary mooring and drifter datasets utilized herein, which were collected by UAF and NOAA-PMEL under BOEM OCS Studies: 2012-079, 2015-022, 2015-034, 2017-065, and 2018-008. We thank the University of Alaska Coastal Marine Institute, in partnership with the U.S. Department of the Interior, Bureau of Ocean Energy Management for supporting and funding this study, especially Heather Crowley for her guidance,

This project would not have been possible without the past vision and efforts of Tom Weingartner, UAF Emeritus faculty, and Warren Horowitz, retired from BOEM.

## References

- Ashjian, C. J., S. R. Braund, R. G. Campbell, J. C. George, J. Kruse, W. Maslowski, S. E. Moore, C. R. Nicolson, S. R. Okkonen, B. F. Sherr, E. B. Sherr, and Y. H. Spitz. (2010) Climate variability, oceanography, bowhead whale distribution, and Inupiat subsistence whaling near Barrow, Alaska Arctic, 63(2):179–194.
- Barrick, D. E., B. J. Lipa, and R. D. Crissman. (1985) Mapping surface currents with CODAR. Sea Tech. 26:43–48.
- Barrick, D. E., and B. J. Lipa. (1986) Correcting for distorted antenna patterns in CODAR ocean surface measurements. IEEE J of Oceanic Engr. OE-11(2):304–309.
- Corlett, W. B., and R. S. Pickart. (2017) The Chukchi Slope Current. Prog. Oceanogr. 153:50–65, doi:10.1016/j.pocean.2017.04.005.
- Danielson S. L., O. Ahkinga, C. Ashjian, E. Basyuk, L. W. Cooper, L. Eisner, E. Farley, K. B. Iken, J. M. Grebmeier, G. Khen, S. R. Jayne, T. Kikuchi, C. Ladd, K. Lu, R. M. McCabe, G. W. K. Moore, S. Nishino, F. Ozenna, R. S. Pickart, I. Polyakov, P. J. Staben, R. Thoman, W. J. Williams, K. Wood, and T. J. Weingartner. (2020) Manifestation and consequences of warming and altered heat fluxes over the Bering and Chukchi Sea continental shelves. Deep-Sea Res. II, 177:104781, doi:10.1016/j.dsr2.2020.104781.
- Danielson, S. L., E. L. Dobbins, and R. Potter. (2018) Oceanography. In: Ecology of Forage Fishes in the Arctic Nearshore, Vollenweider et al. (eds), North Slope Borough Shell Baseline Studies Program Final Report, 476 pp.
- Danielson, S. L., L. Eisner, and C. Ladd. (2017a) A comparison between late summer 2012 and 2013 water masses, macronutrients, and phytoplankton standing crops in the northern Bering and Chukchi Seas. Deep-Sea Res. II, 135:7–26, doi:10.1016/j.dsr2.2016.05.024.
- Danielson, S. L., L. Cooper, J. Grebmeier, C. Hauri, K. Iken, R. R. Hopcroft, J. Horne, C. Lalande, A. M. P. McDonnell, K. Stafford, and P. Winsor. (2017b) Collaborative approaches to multi-disciplinary monitoring of the Chukchi shelf marine ecosystem: Networks of networks for maintaining long-term Arctic observations. IEEE OCEANS-Anchorage 2017, p. 1–7.
- Danielson, S. L., and T. J. Weingartner. (2007) Estimates of Oil Spill Dispersion Extent in the Nearshore Alaskan Beaufort Sea Based on In-Situ Oceanographic Measurements, Report prepared for ADEC, 154 pp.
- Fang, Y.-C., R. A. Potter, H. Statscewich, T. J. Weingartner, P. Winsor, and B. K. Irving. (2017) Surface current patterns in the northeastern Chukchi Sea and their response to wind forcing. J. Geophys. Res. Oceans, 122:9530–9547, doi:10.1002/2017JC013121.
- Fang, Y.-C., T. J. Weingartner, E. L. Dobbins, P. Winsor, H. Statscewich, R. A. Potter, et al. (2020). Circulation and thermohaline variability of the Hanna Shoal region on the northeastern Chukchi Sea shelf. J. Geophys. Res. Oceans, 125:e2019JC015639, doi:10.1029/2019JC015639.
- Hauri, C., S. Danielson, A. M. P. McDonnell, R. R. Hopcroft, P. Winsor, P. Shipton, C. Lalande, K. M. Stafford, J. K. Horne, L. W. Cooper, J. M. Grebmeier, A. Mahoney, K. Maisch, M. McCammon, H. Statscewich, A. Sybrandy, and T. Weingartner. (2018) From sea ice to seals: A moored marine ecosystem observatory in the Arctic. Ocean Sci., 14:1423–1433, doi:10.5194/os-14-1423-2018.
- Jones, B. M., L. M. Farquharson, C. A. Baughman, R. M. Buzard, C. D. Arp, G. Grosse, et al. (2018) A decade of remotely sensed observations highlight complex processes linked to coastal permafrost bluff erosion in the Arctic. Env. Res. Lett., 13:115001, doi:10.1088/1748-9326/aae471.

- Kohonen, T. (2001) Self-organizing maps. Springer Series in Information Sciences (3rd ed., Vol. 30, 501 pp.). Springer, New York, NY
- Lalande, C., J. M. Grebmeier, A. M. P. McDonnell, R. R. Hopcroft, S. O'Daly, and S. L. Danielson. (2021) Impact of a warm anomaly in the Pacific Arctic region derived from time-series export fluxes. *PLoS ONE*, 16(8):e0255837, doi:10.1371/journal.pone.0255837.
- Okkonen, S. R., C. J. Ashjian, R. G. Campbell, W. Maslowski, J. L. Clement-Kinney, and R. Potter. (2009) Intrusion of warm Bering/Chukchi waters onto the shelf in the western Beaufort Sea. *J. Geophys. Res.*, 114:C00A11, doi:10.1029/2008JC004870.
- Okkonen, S. R., C. J. Ashjian, R. G. Campbell, J. T. Clarke, S. E. Moore, and K. D. Taylor. (2011) Satellite observations of circulation features associated with a bowhead whale feeding 'hotspot' near Barrow, Alaska. *Remote Sens. Env.*, 115:2136–2174, doi:10.1016/j.rse.2011.04.024.
- Pickart, R. S., L. M. Schulze, G. W. K. Moore, M. A. Charette, K. R. Arrigo, G. Gijken, and S. L. Danielson (2013) Long-term trends of upwelling and impacts on primary productivity in the Alaskan Beaufort Sea. *Deep-Sea Res. I*, 79:106–121, doi:10.1016/j.dsr.2013.05.003.
- Stabeno, P., N. Kachel, C. Ladd, and R. Woodgate (2018) Flow patterns in the eastern Chukchi Sea: 2010–2015. *J. Geophys. Res. Oceans*, 123:1177–1195, doi:10.1002/2017JC013135.
- Schulze, L.M. and R.S. Pickart. 2012. Seasonal variation of upwelling in the Alaskan Beaufort Sea: Impact of sea ice cover. *J. of Geophys. Res.*, 117:C06022, doi.org/10.1029/2012JC007985.
- Teague, C. (2001) Ionospheric Effects on Coastal Radar Systems, p. 56-61, In: *Radiowave Oceanography; First International Workshop*, H. C. Graber and J. D. Paduan (eds), University of Miami, 152 pp.
- Vollenweider, J. J., R. A. Heintz, K. M. Boswell, B. L. Norcross, C. Li, M. B. Barton, L. Sousa, A. Pinchuk, S. L. Danielson, and C. George. (2018) Ecology of Forage Fishes in the Arctic Nearshore. North Slope Borough Shell Baseline Studies Program, Final Report, 476 pp.
- Weingartner, T. J., E. Dobbins, S. Danielson, P. Winsor, R. Potter, and H. Statscewich. (2013). Hydrographic variability over the northeastern Chukchi Sea shelf in summer-fall 2008–2010. *Continental Shelf Research*, 67:5–22, doi.org/10.1016/j.csr.2013.03.012.
- Weingartner T. J., C. B. Irvine, E. L. Dobbins, S. Danielson, L. Deousa, B. Adams, R. Suydam, and W. Neakok. (2015) Satellite-tracked Drifter Measurements in the Chukchi and Beaufort Seas. U.S. Dept. Interior Alaska Outer Cont. Shelf Reg. OCS Study BOEM 2015-022, 171 pp.
- Weingartner, T. J., R. Pickart, P. Winsor, W. B. Corlett, E. L. Dobbins, Y.-C. Fang, C. Irvine, B. Irving, M. Li, K. Lu, et al. (2017a) Characterization of the Circulation on the Continental Shelf Areas of the Northeast Chukchi and Western Beaufort Seas. Fairbanks, AK: US Department of the Interior, Bureau of Ocean Energy Management. OCS Study BOEM 2017-065, 221 pp.
- Weingartner, T. J., R. A. Potter, C. A. Stoudt, E. L. Dobbins, H. Statscewich, P. R. Winsor, T. D. Mudge, and K. Borg. (2017b) Transport and thermohaline variability in Barrow Canyon on the Northeastern Chukchi Sea Shelf. *J. Geophys. Res. Oceans*, 122(5):3565–3585, doi:10.1002/2016JC012636.

## Appendices

### Appendix A: Mean current speed magnitude by year.

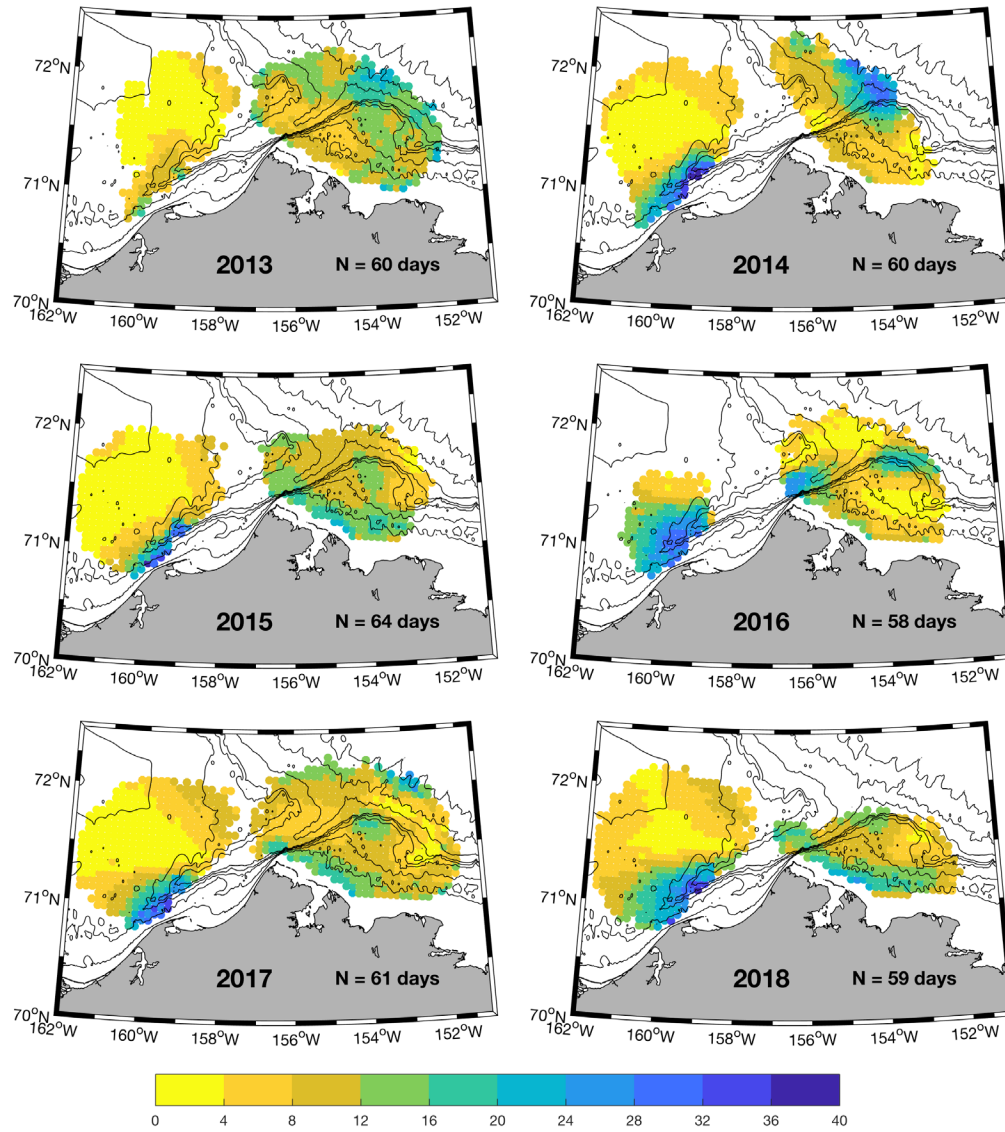


Figure A1: Mean current speeds ( $\text{cm s}^{-1}$ ) of the HFR flow field by year. Bathymetric contours are drawn at 20, 40, 60, 80, 100, 200, 1000, and 2000 m depth levels.

## Appendix B: Mean current variance magnitude by year.

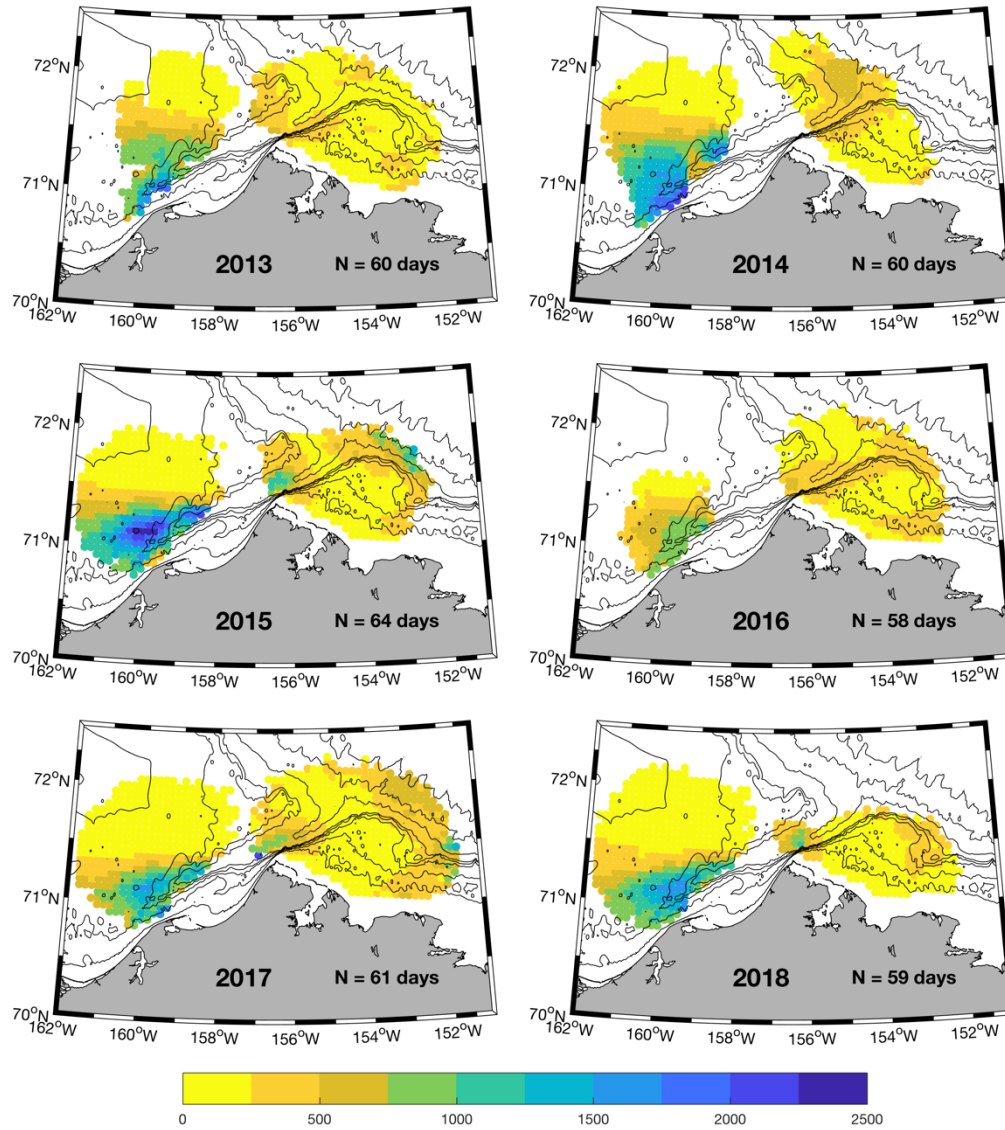


Figure A2: Mean variance ( $\text{cm}^2 \text{s}^{-2}$ ) of the HFR flow field by year. Bathymetric contours are drawn at 20, 40, 60, 80, 100, 200, 1000, and 2000 m depth levels.

**Appendix C: Surface current composites for the case of weak mean daily wind speed, and blowing to each of the four quadrants.**

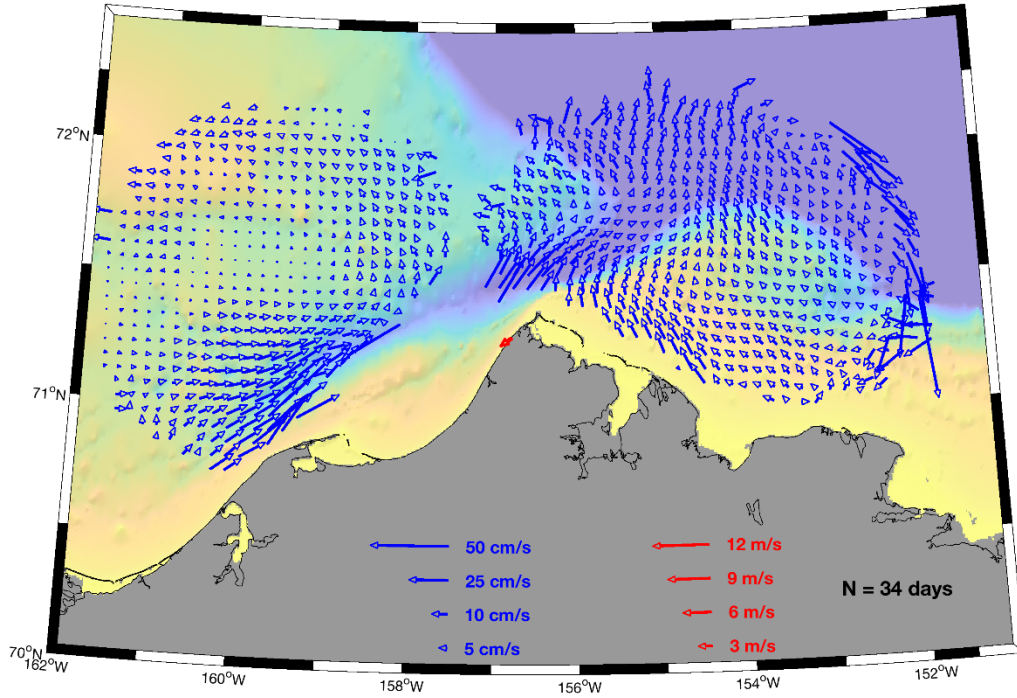


Figure A3: Average surface current vectors for wind speed  $< 4 \text{ m s}^{-1}$ ,  $U < 0$ , and  $V < 0$ .

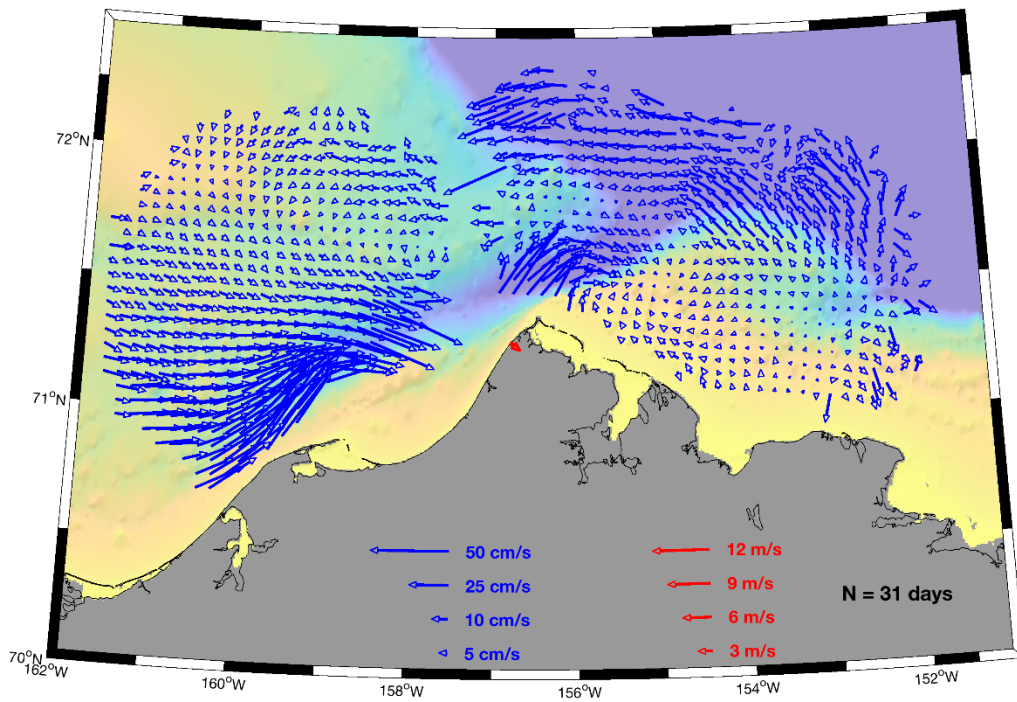


Figure A4: Average surface current vectors for wind speed  $< 4 \text{ m s}^{-1}$ ,  $U > 0$ , and  $V < 0$ .

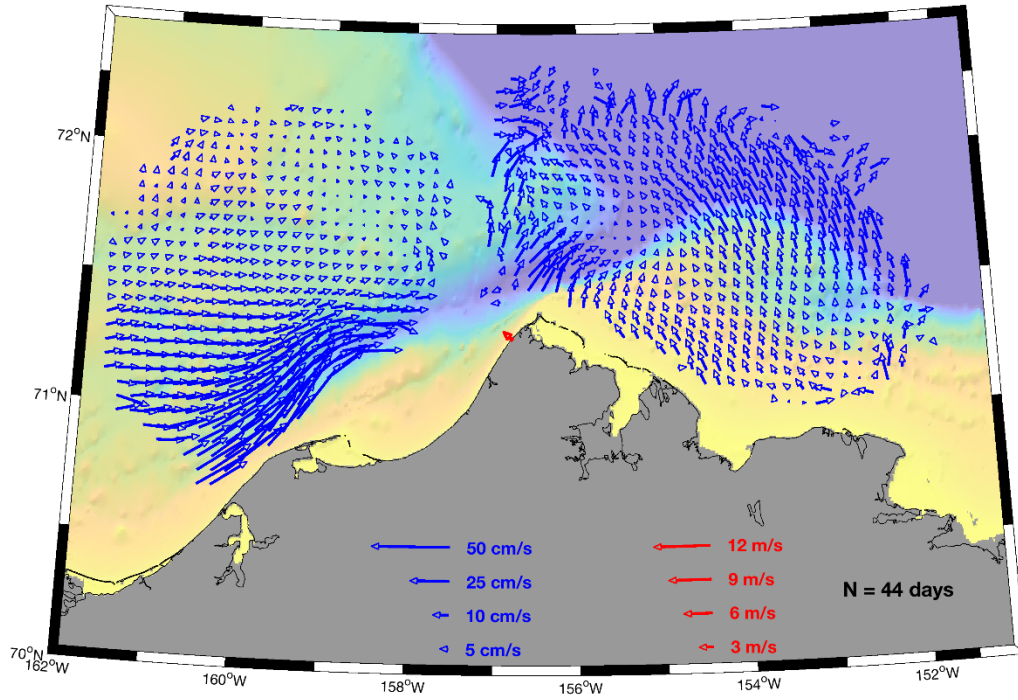


Figure A5: Average surface current vectors for wind speed  $< 4 \text{ m s}^{-1}$ ,  $U < 0$  and  $V > 0$ .

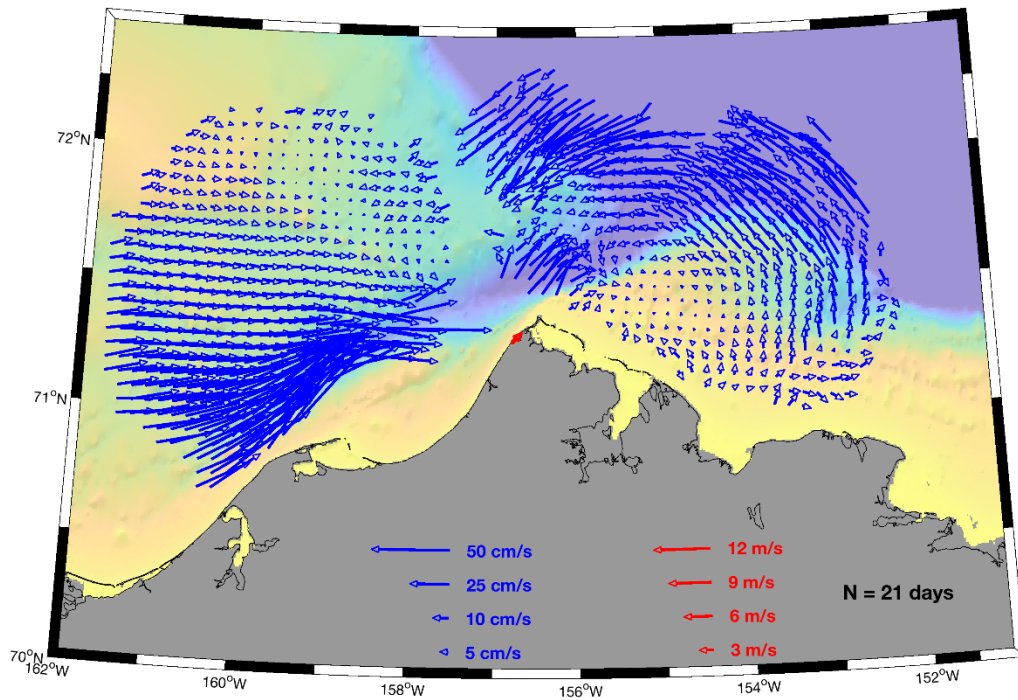


Figure A6: Average surface current vectors for wind speed  $< 4 \text{ m s}^{-1}$ ,  $U < 0$  and  $V > 0$ .

## Appendix D: Flow field divergence based on wind speed and direction.

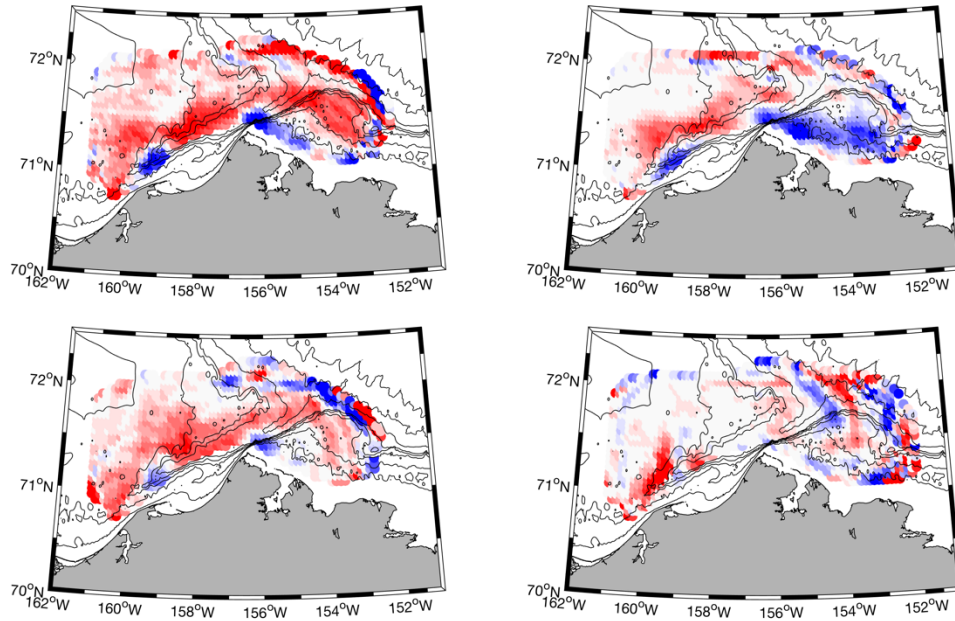


Figure A7: Divergence ( $\text{cm s}^{-1} \text{ km}^{-1}$ ) composites based on wind speed and direction. All four panels are for daily mean wind speed  $> 6 \text{ m s}^{-1}$ . Upper left:  $U > 0$  &  $V > 0$ ; Upper right:  $U < 0$  &  $V > 0$ ; Lower left:  $U > 0$  &  $V < 0$ ; Lower right:  $U < 0$  &  $V < 0$ .

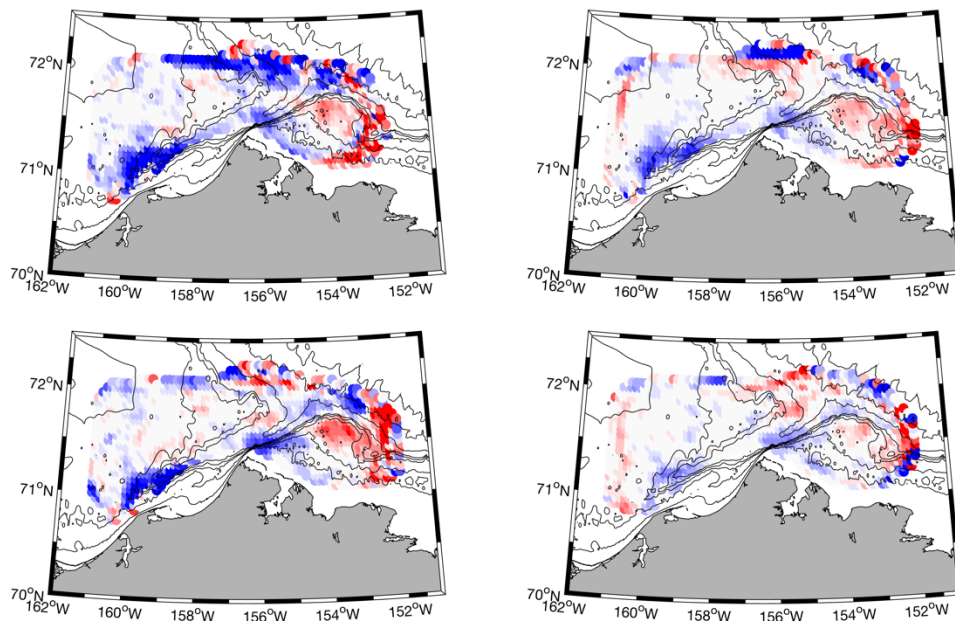


Figure A8: Divergence ( $\text{cm s}^{-1} \text{ km}^{-1}$ ) composites based on wind speed and direction. All four panels are for daily mean wind speed  $< 4 \text{ m s}^{-1}$ . Upper left:  $U > 0$  &  $V > 0$ ; Upper right:  $U < 0$  &  $V > 0$ ; Lower left:  $U > 0$  &  $V < 0$ ; Lower right:  $U < 0$  &  $V < 0$ .

## Appendix E: Flow field relative vorticity based on wind speed and direction.

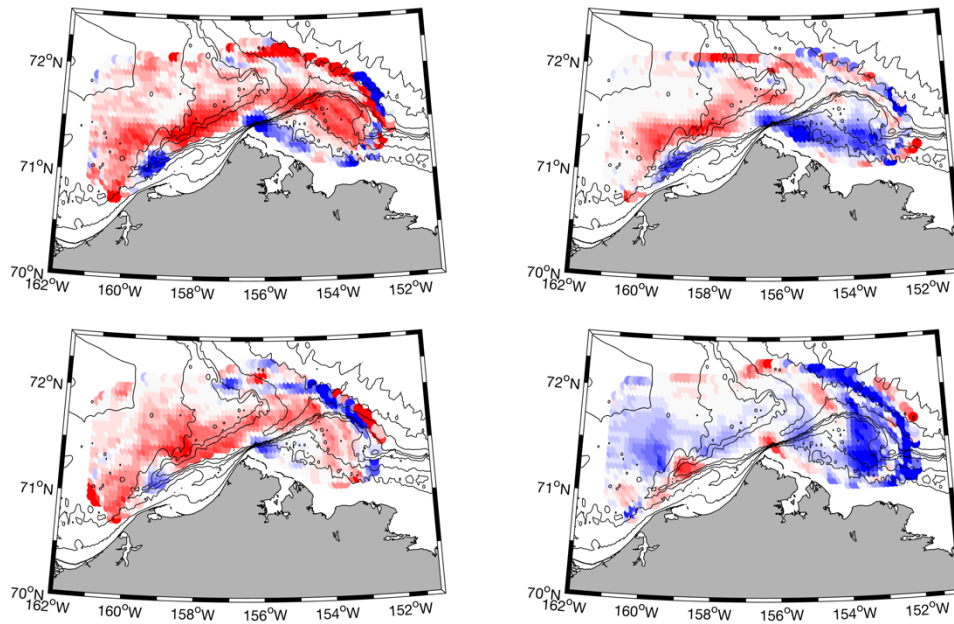


Figure A9: Relative vorticity composites based on wind speed and direction. All four panels are for daily mean wind speed  $> 6 \text{ m s}^{-1}$ . Upper left:  $U > 0$  &  $V > 0$ ; Upper right;  $U < 0$  &  $V > 0$ ; Lower left:  $U > 0$  &  $V < 0$ ; Lower right:  $U < 0$  &  $V < 0$ .

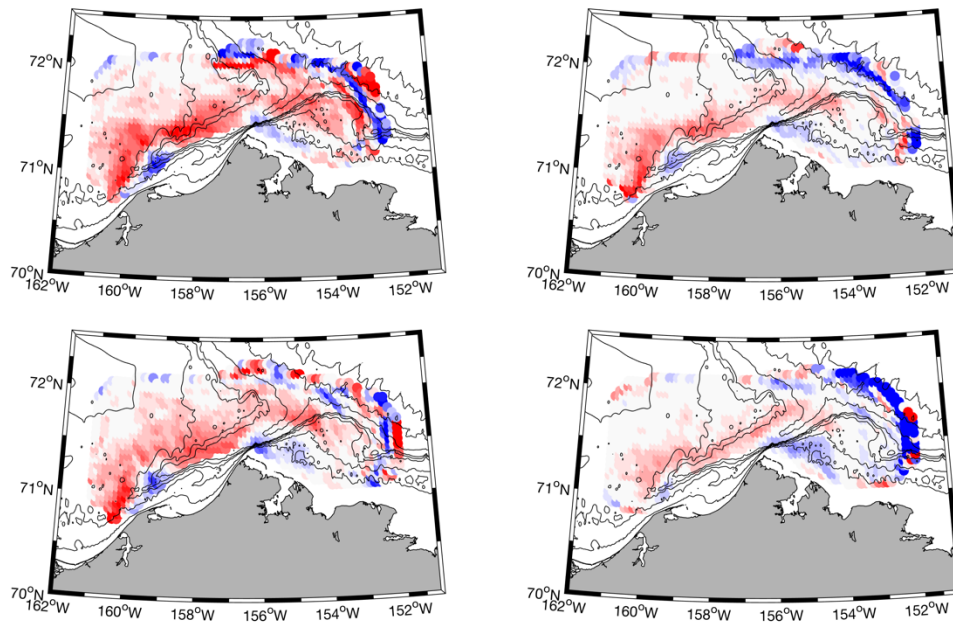


Figure A10: Relative vorticity composites based on wind speed and direction. All four panels are for daily mean wind speed  $< 4 \text{ m s}^{-1}$ . Upper left:  $U > 0$  &  $V > 0$ ; Upper right;  $U < 0$  &  $V > 0$ ; Lower left:  $U > 0$  &  $V < 0$ ; Lower right:  $U < 0$  &  $V < 0$ .

# Appendix F: Self-organized Maps by Year

2013

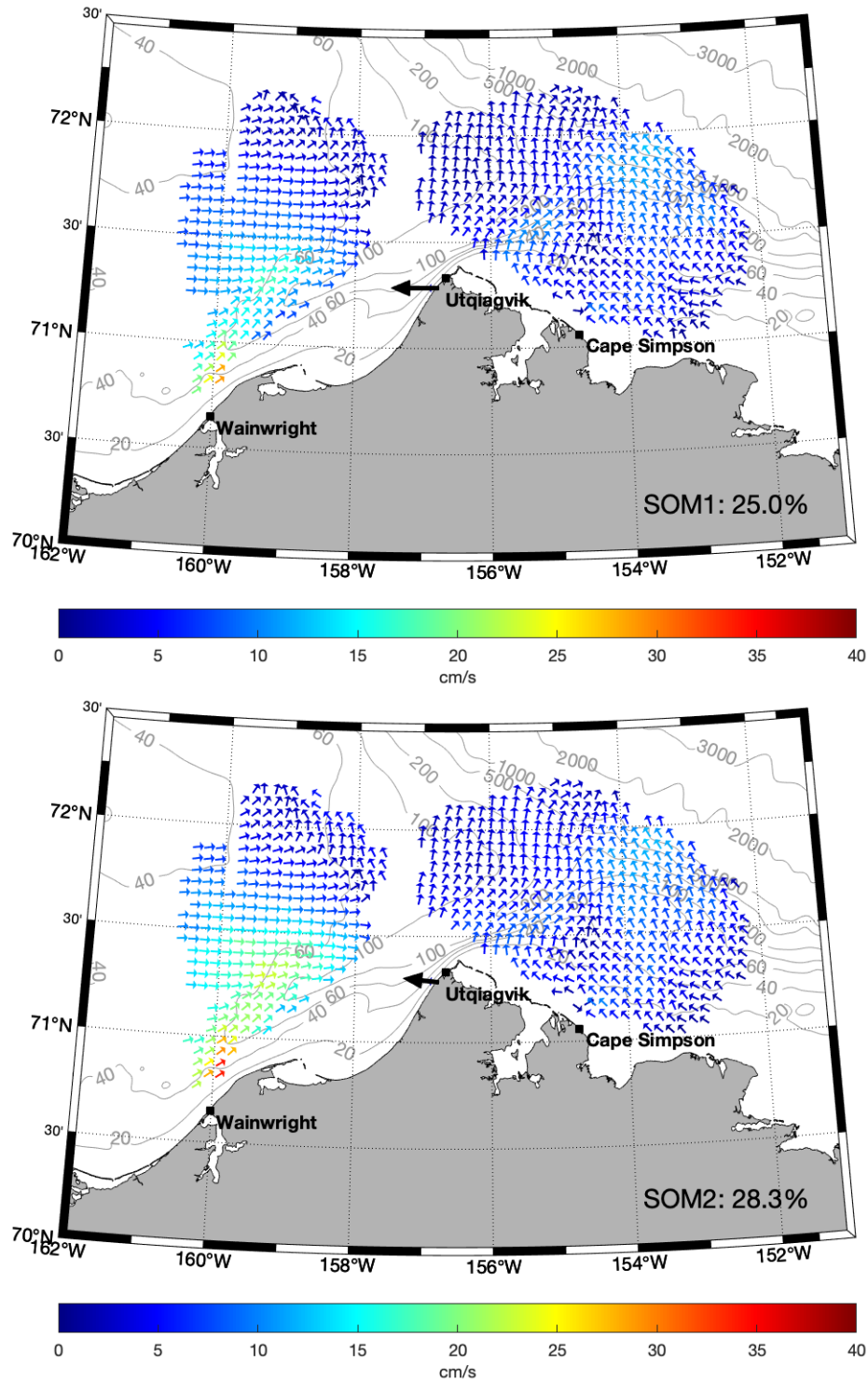


Figure A11: Self-organized map (SOM) patterns 1 (top) and 2 (bottom) for all daily HFR mean maps from 2013.

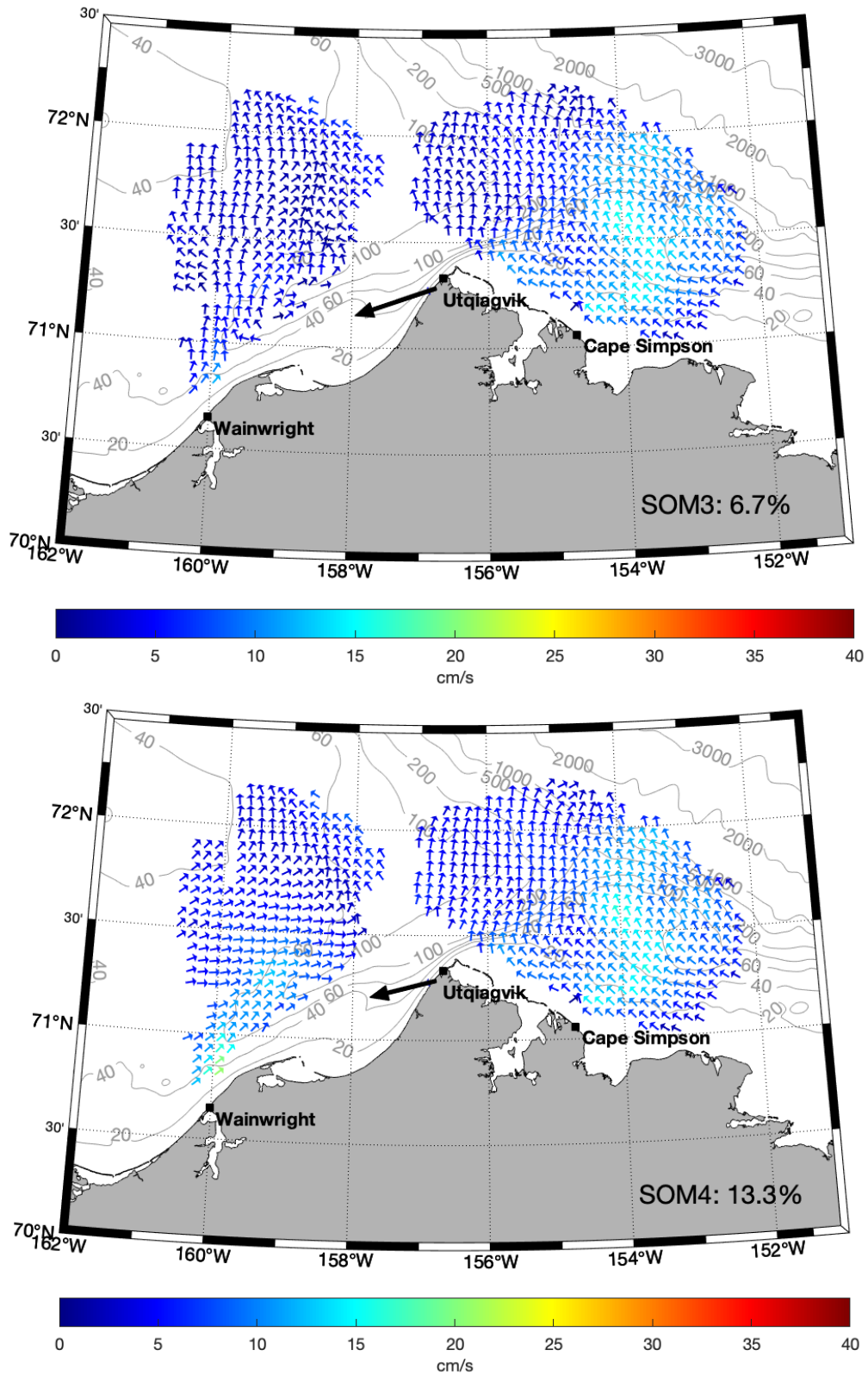


Figure A12: Self-organized map (SOM) patterns 3 (top) and 4 (bottom) for all daily HFR mean maps from 2013.

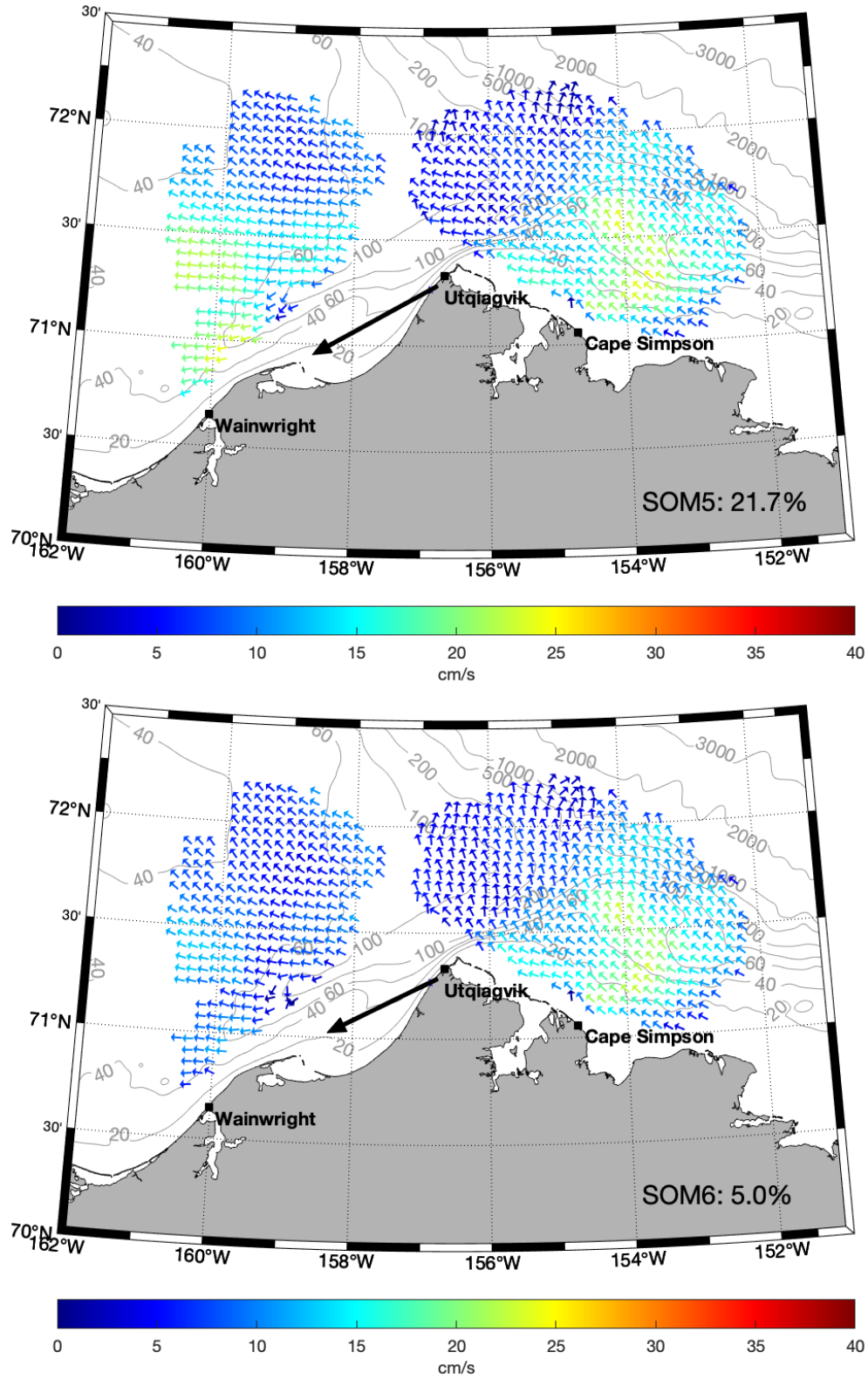


Figure A13: Self-organized map (SOM) patterns 5 (top) and 6 (bottom) for all daily HFR mean maps from 2013.

2014

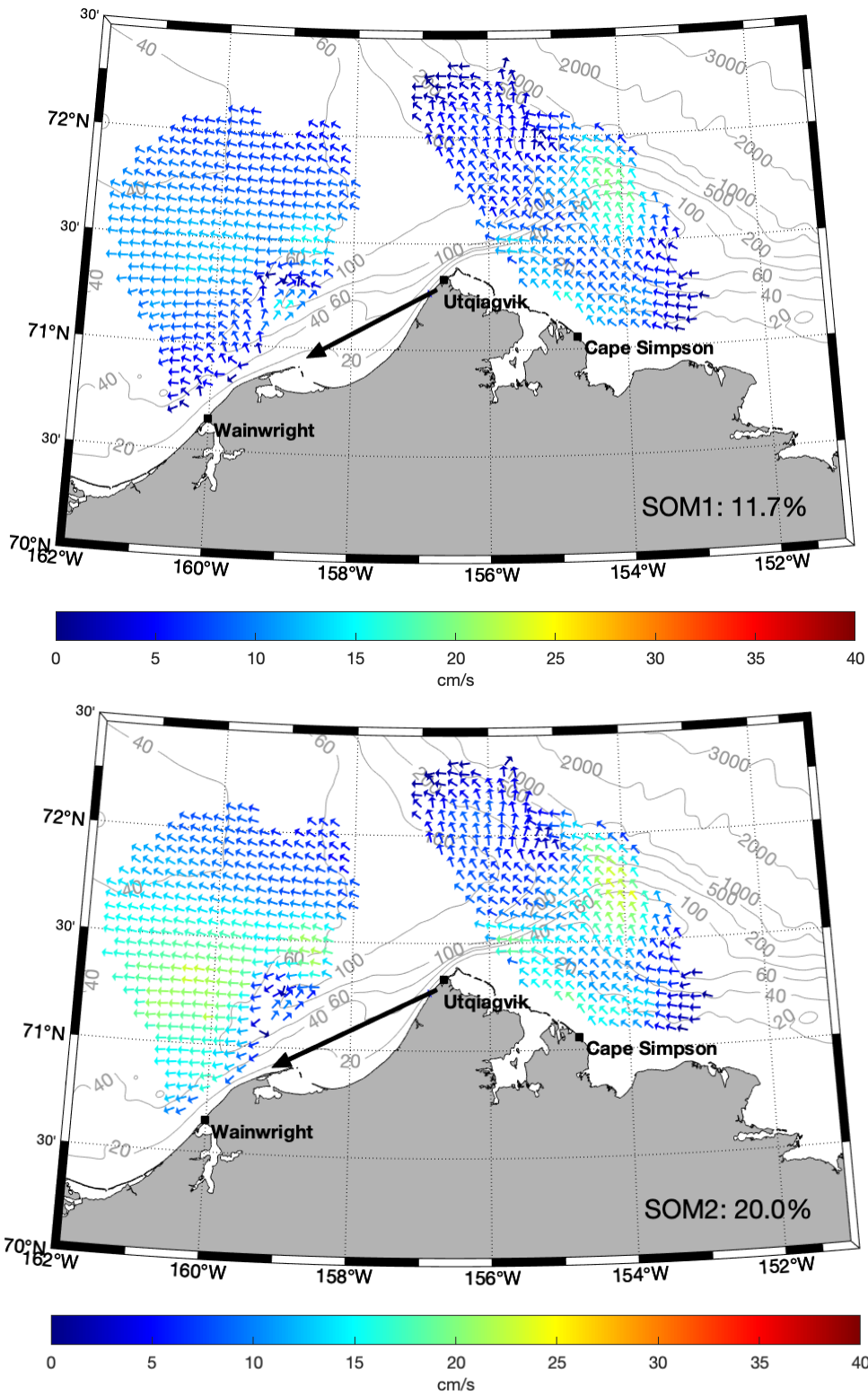


Figure A14: Self-organized map (SOM) patterns 1 (top) and 2 (bottom) for all daily HFR mean maps from 2014.

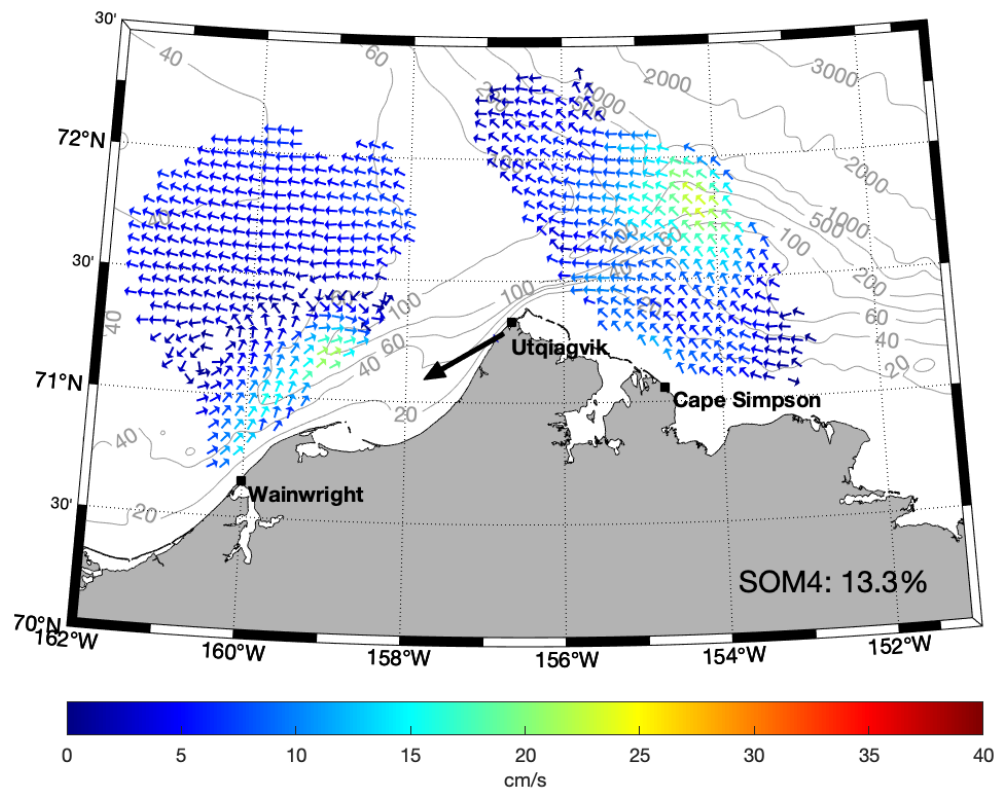
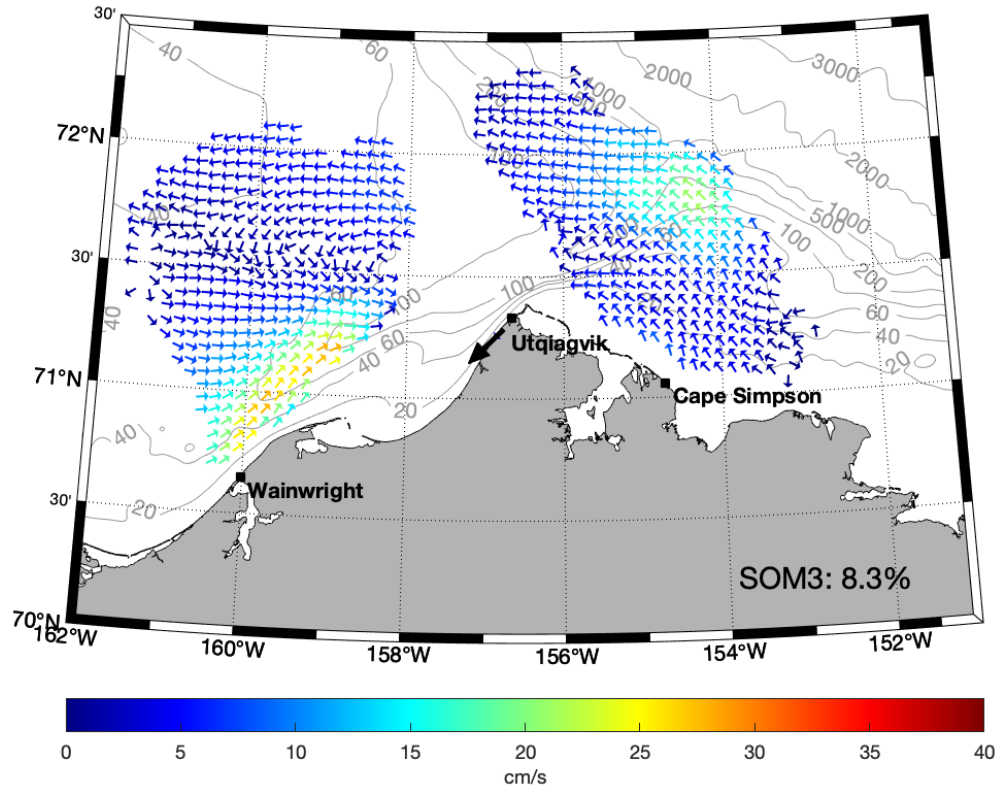


Figure A15: Self-organized map (SOM) patterns 3 (top) and 4 (bottom) for all daily HFR mean maps from 2014.

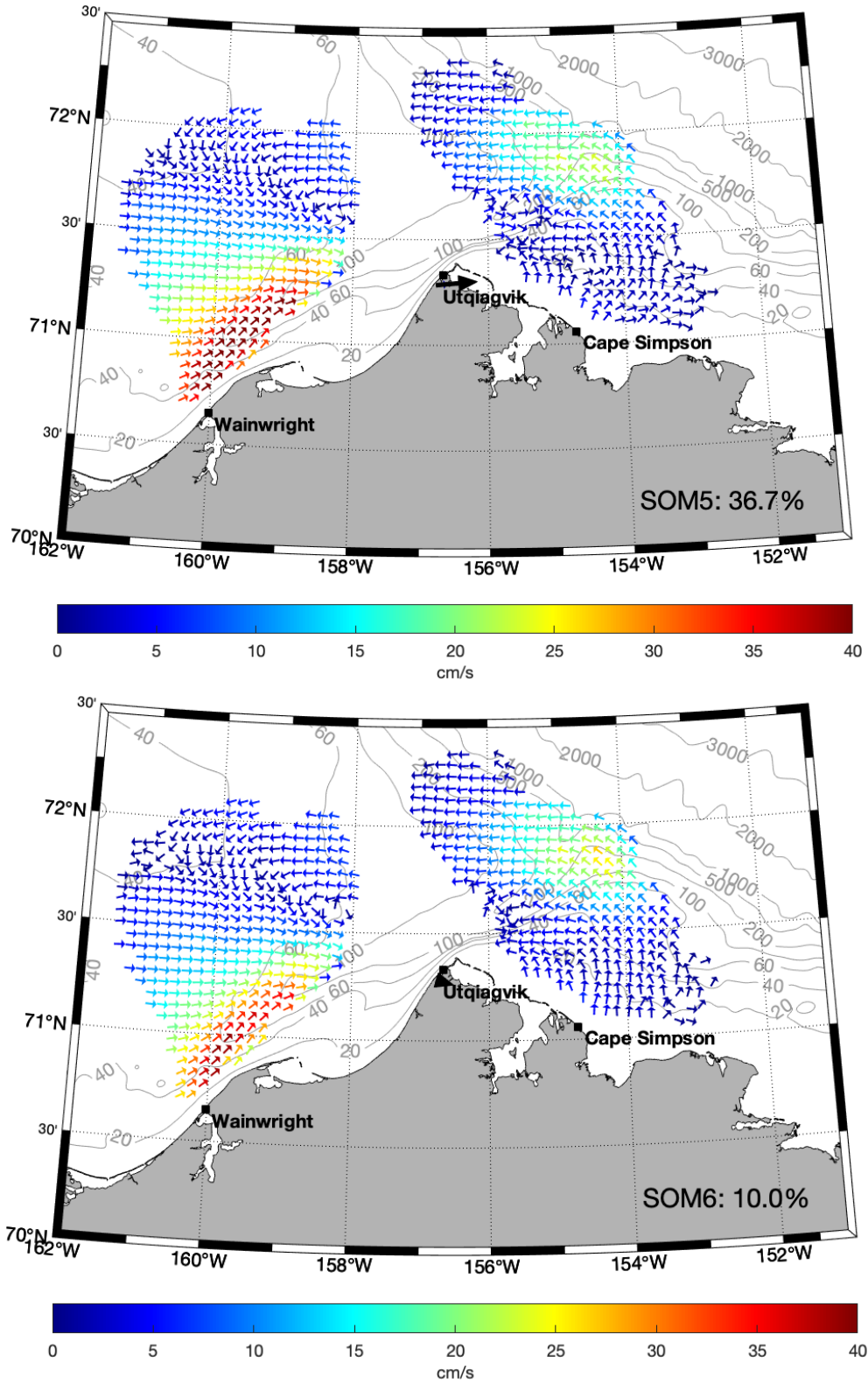


Figure A16: Self-organized map (SOM) patterns 5 (top) and 6 (bottom) for all daily HFR mean maps from 2014.

2015

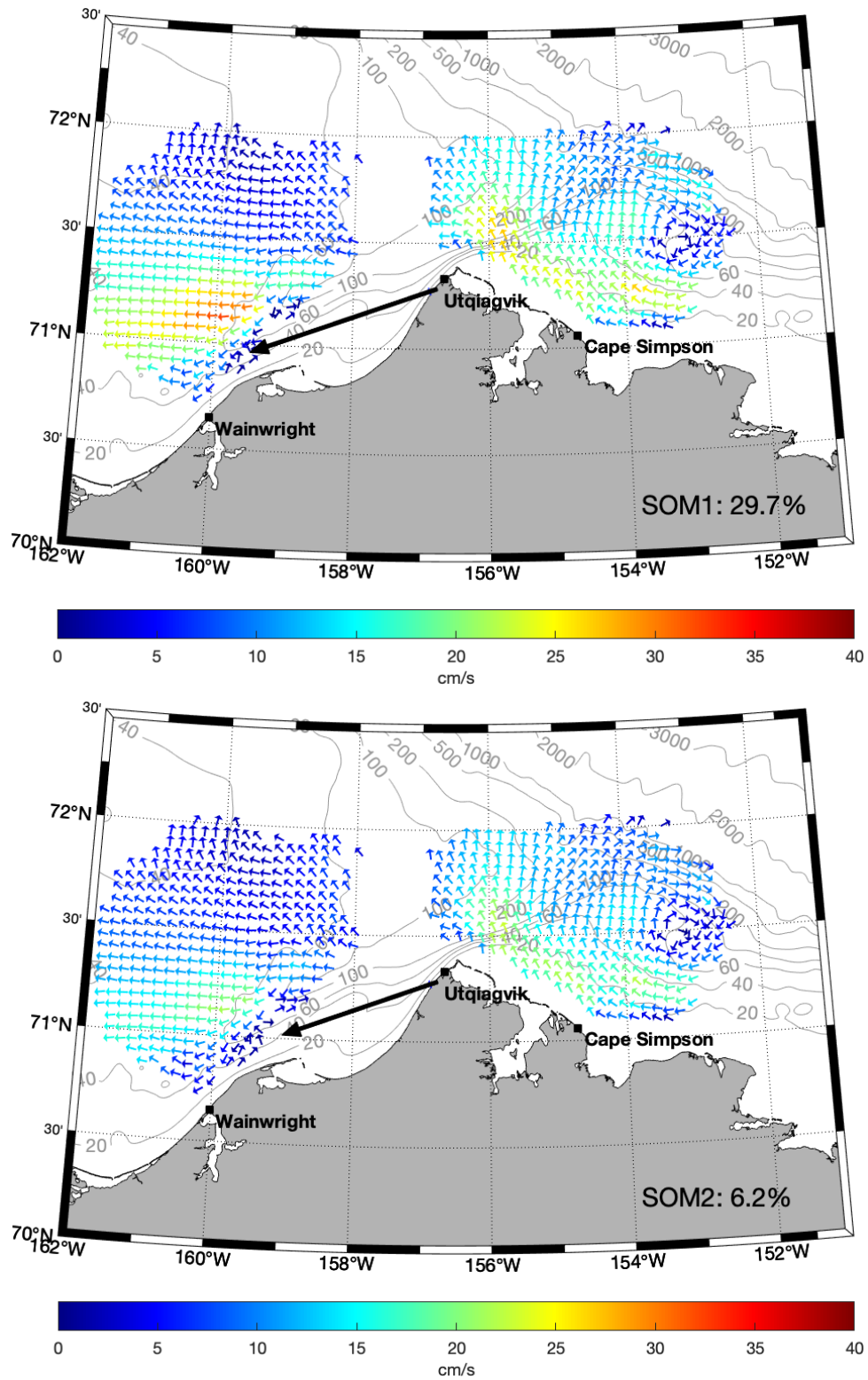


Figure A17: Self-organized map (SOM) patterns 1 (top) and 2 (bottom) for all daily HFR mean maps from 2015.

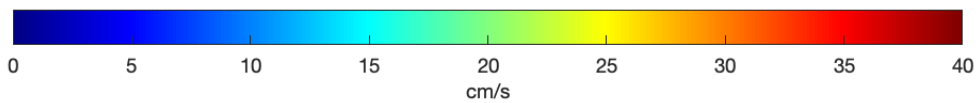
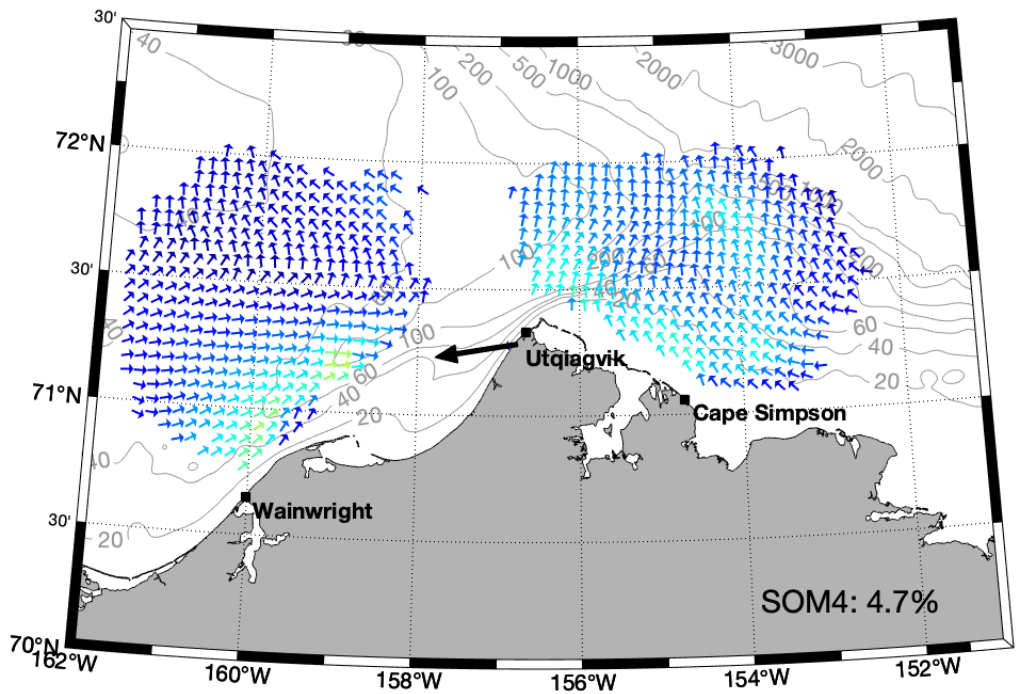
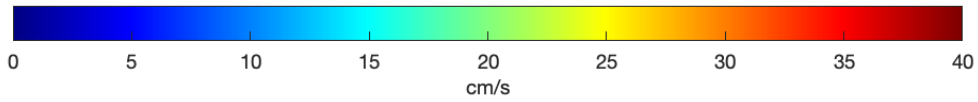
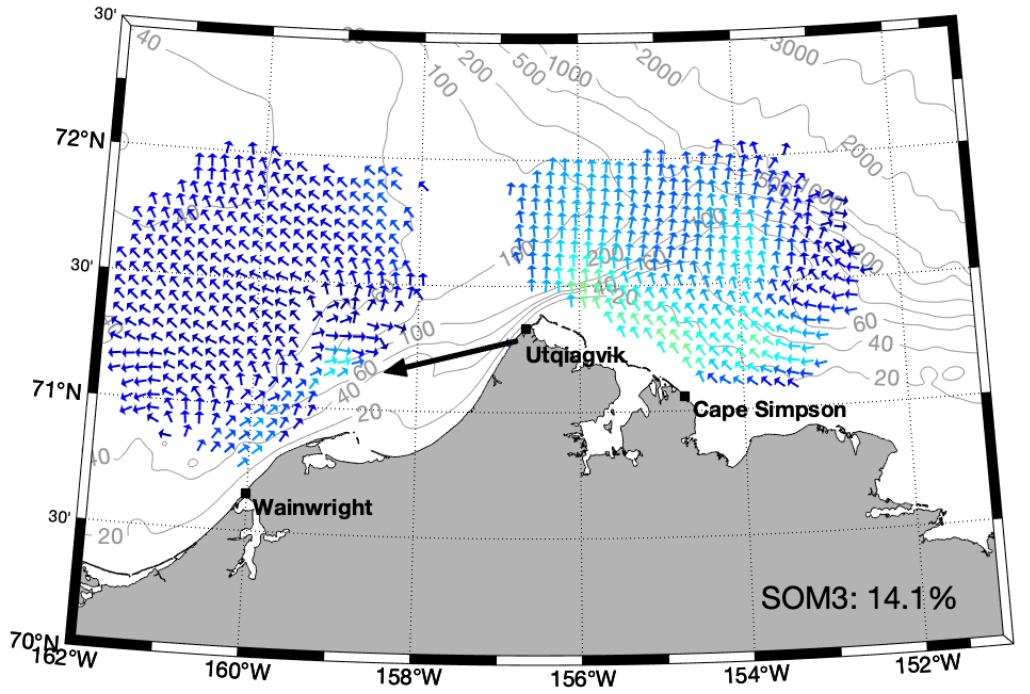


Figure A18: Self-organized map (SOM) patterns 3 (top) and 4 (bottom) for all daily HFR mean maps from 2015.

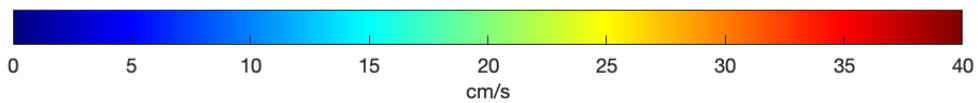
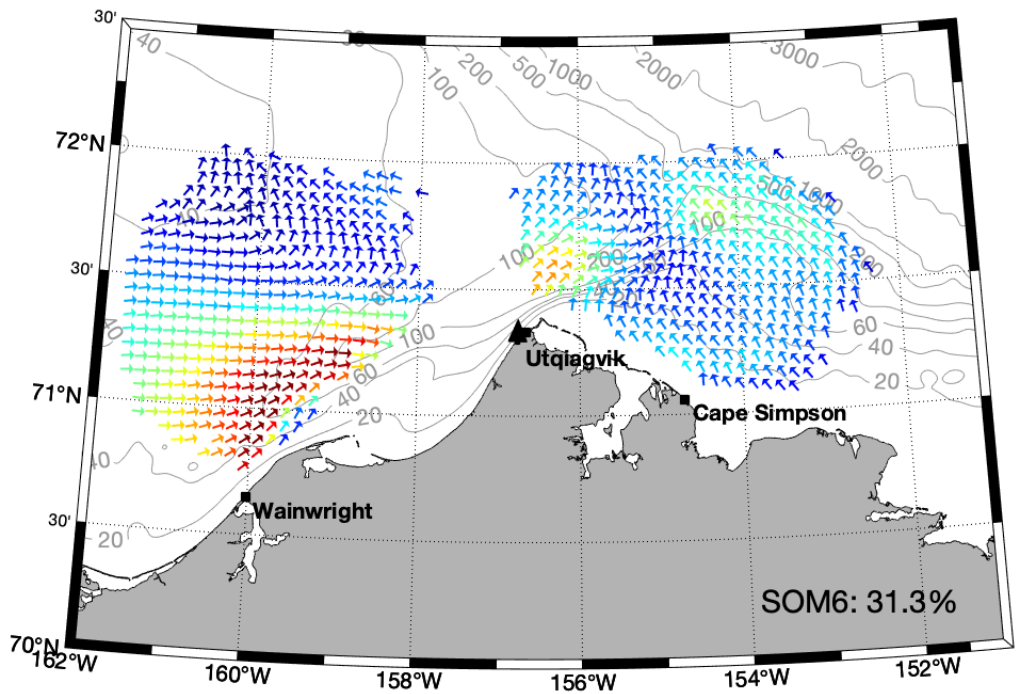
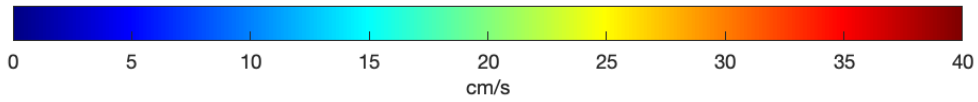
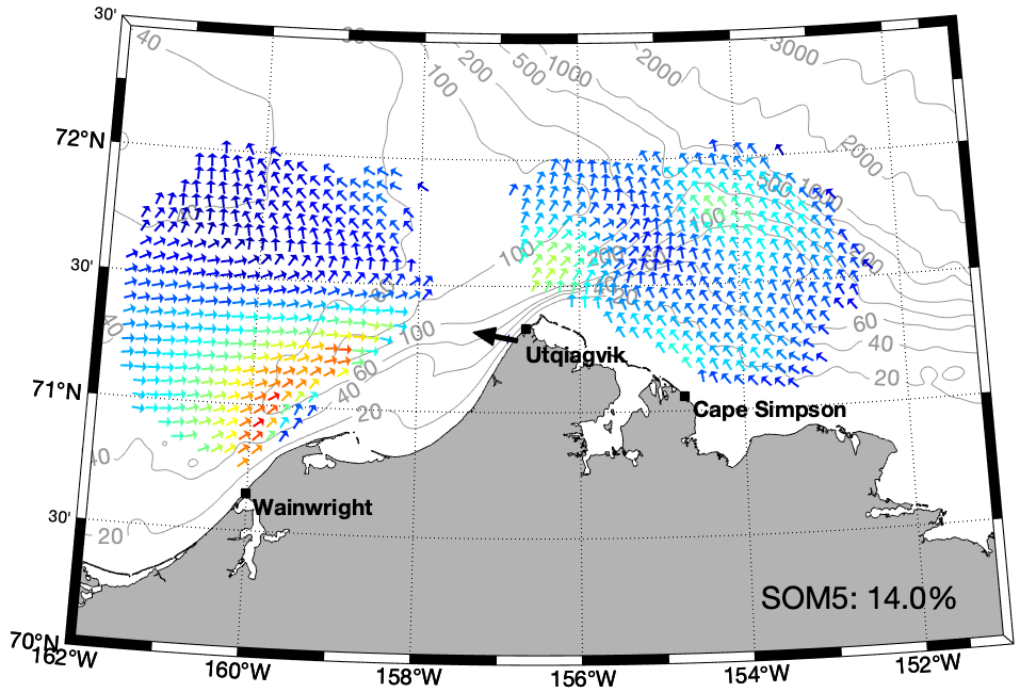


Figure A19: Self-organized map (SOM) patterns 5 (top) and 6 (bottom) for all daily HFR mean maps from 2015.

2016

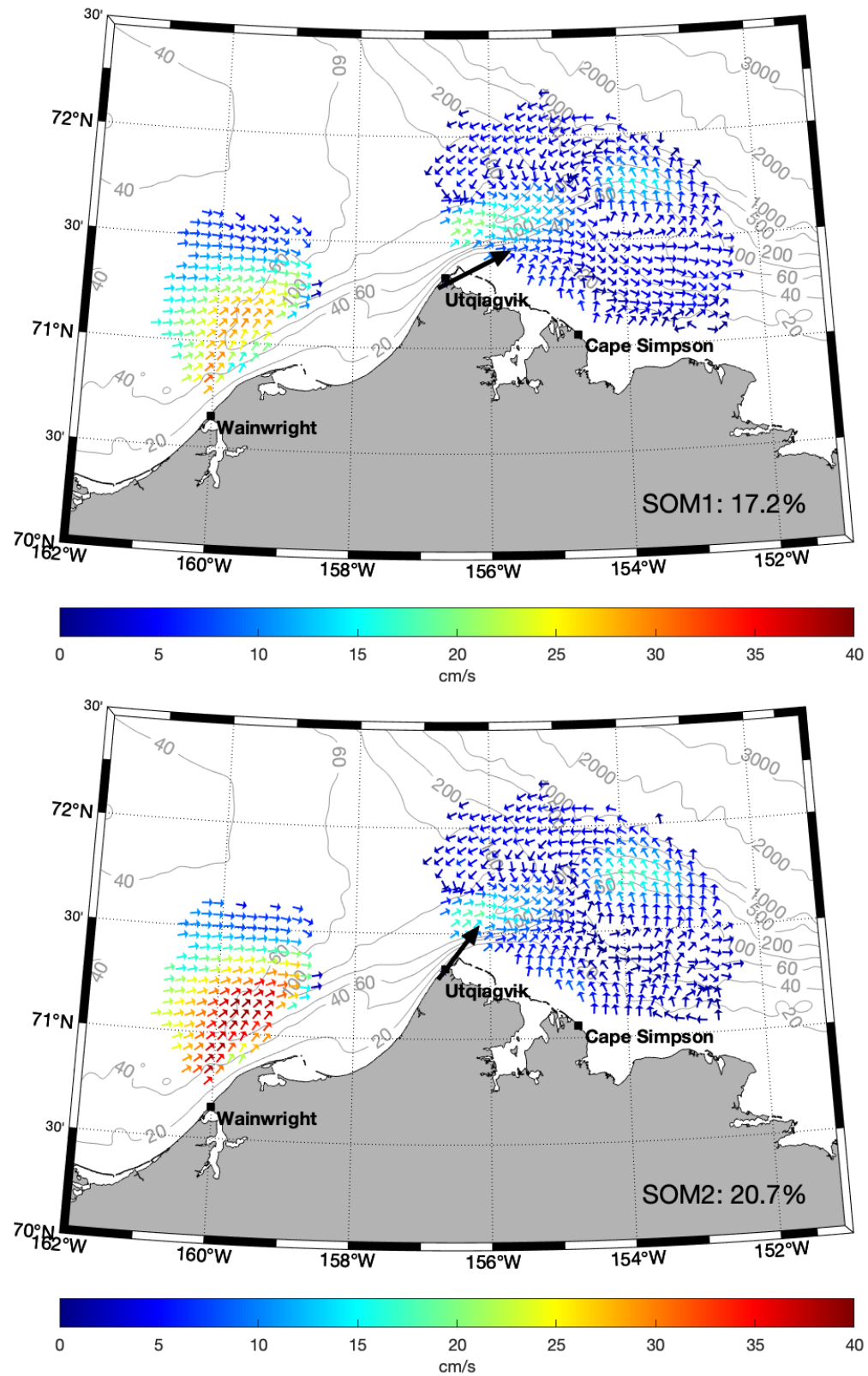


Figure A20: Self-organized map (SOM) patterns 1 (top) and 2 (bottom) for all daily HFR mean maps from 2016.

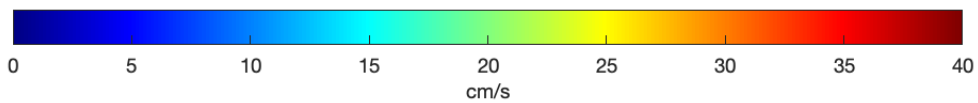
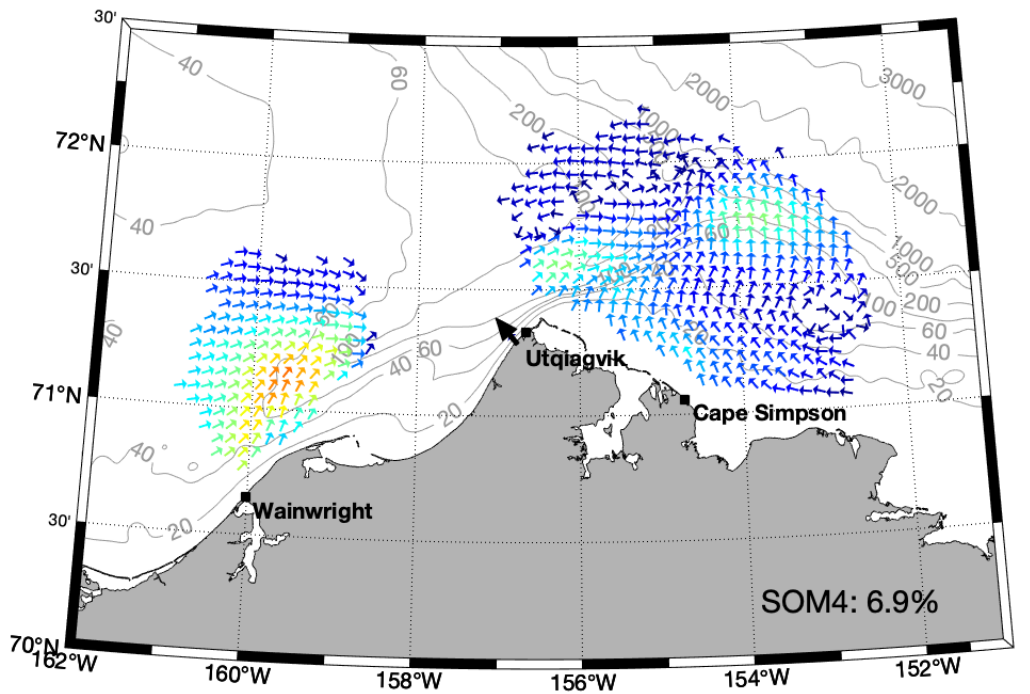
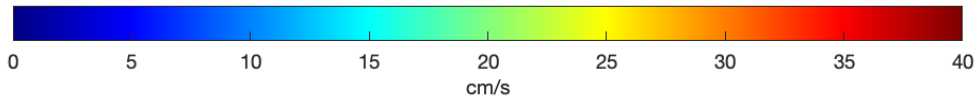
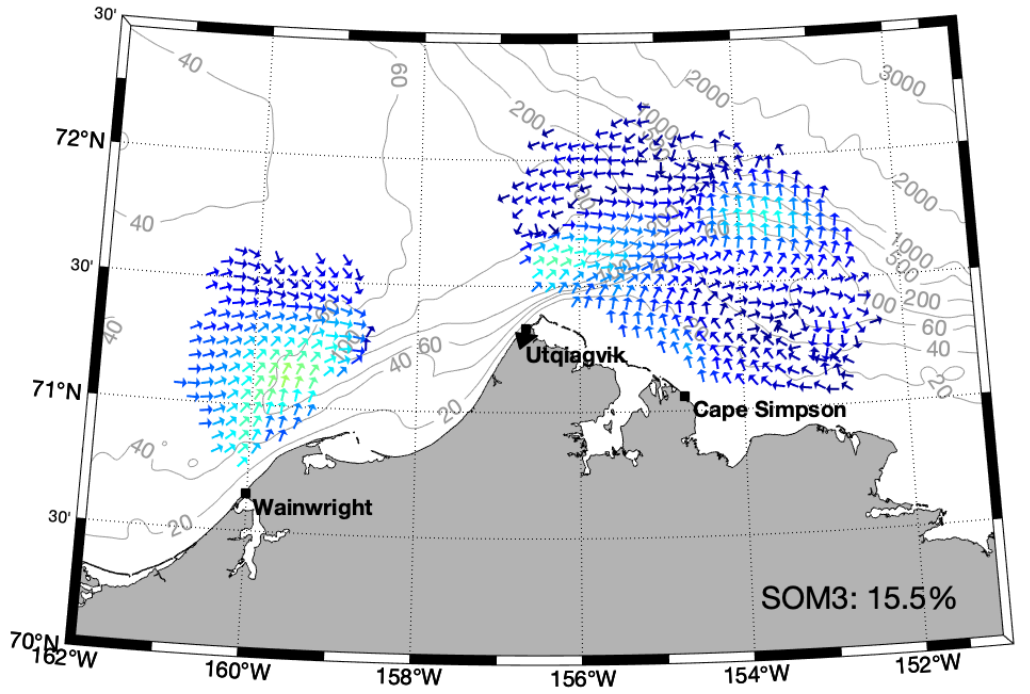


Figure A21: Self-organized map (SOM) patterns 3 (top) and 4 (bottom) for all daily HFR mean maps from 2016.

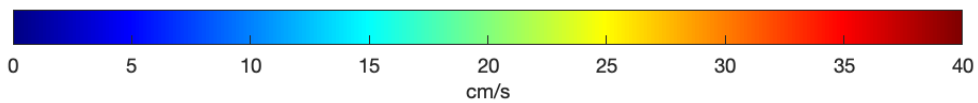
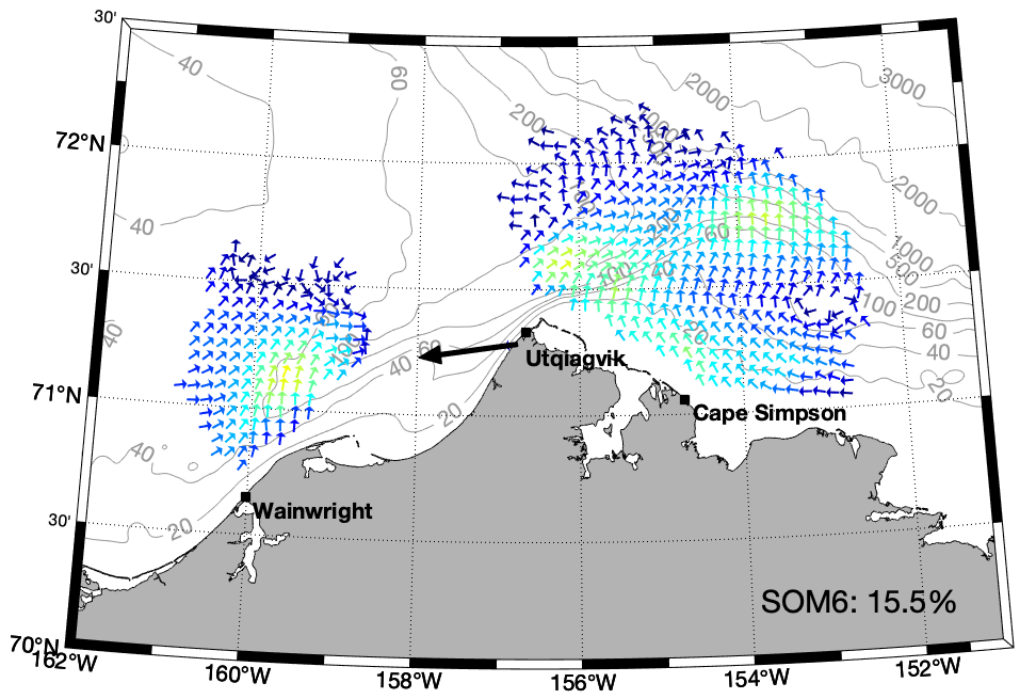
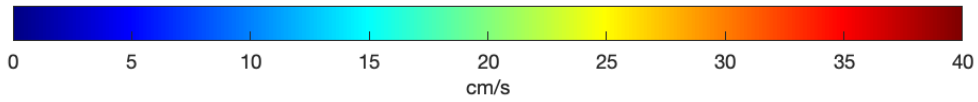
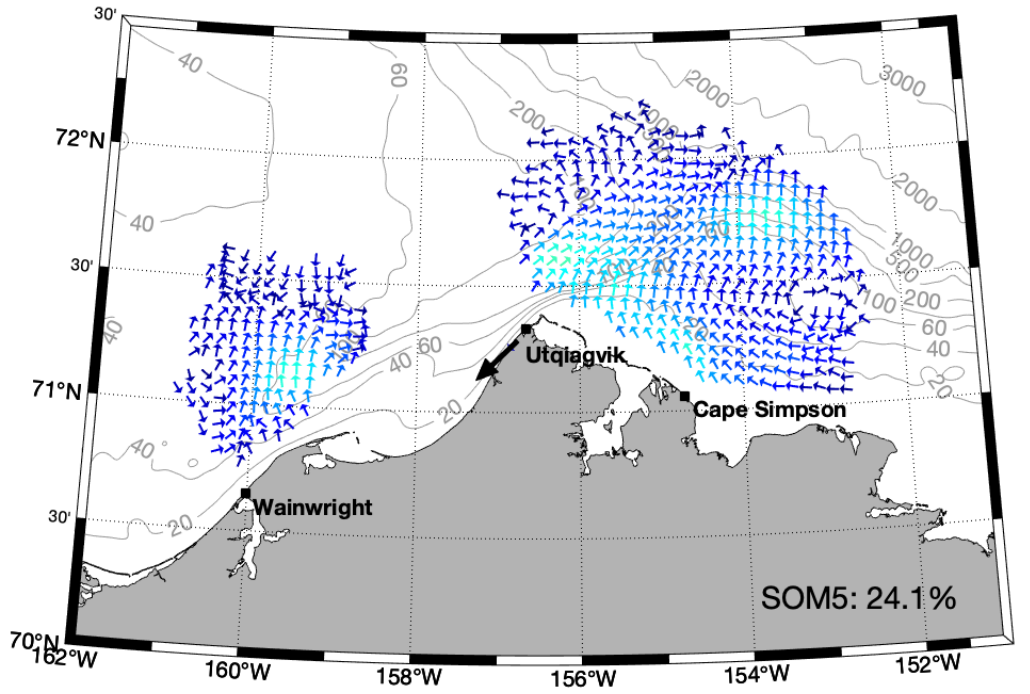


Figure A22: Self-organized map (SOM) patterns 5 (top) and 6 (bottom) for all daily HFR mean maps from 2016.

2017

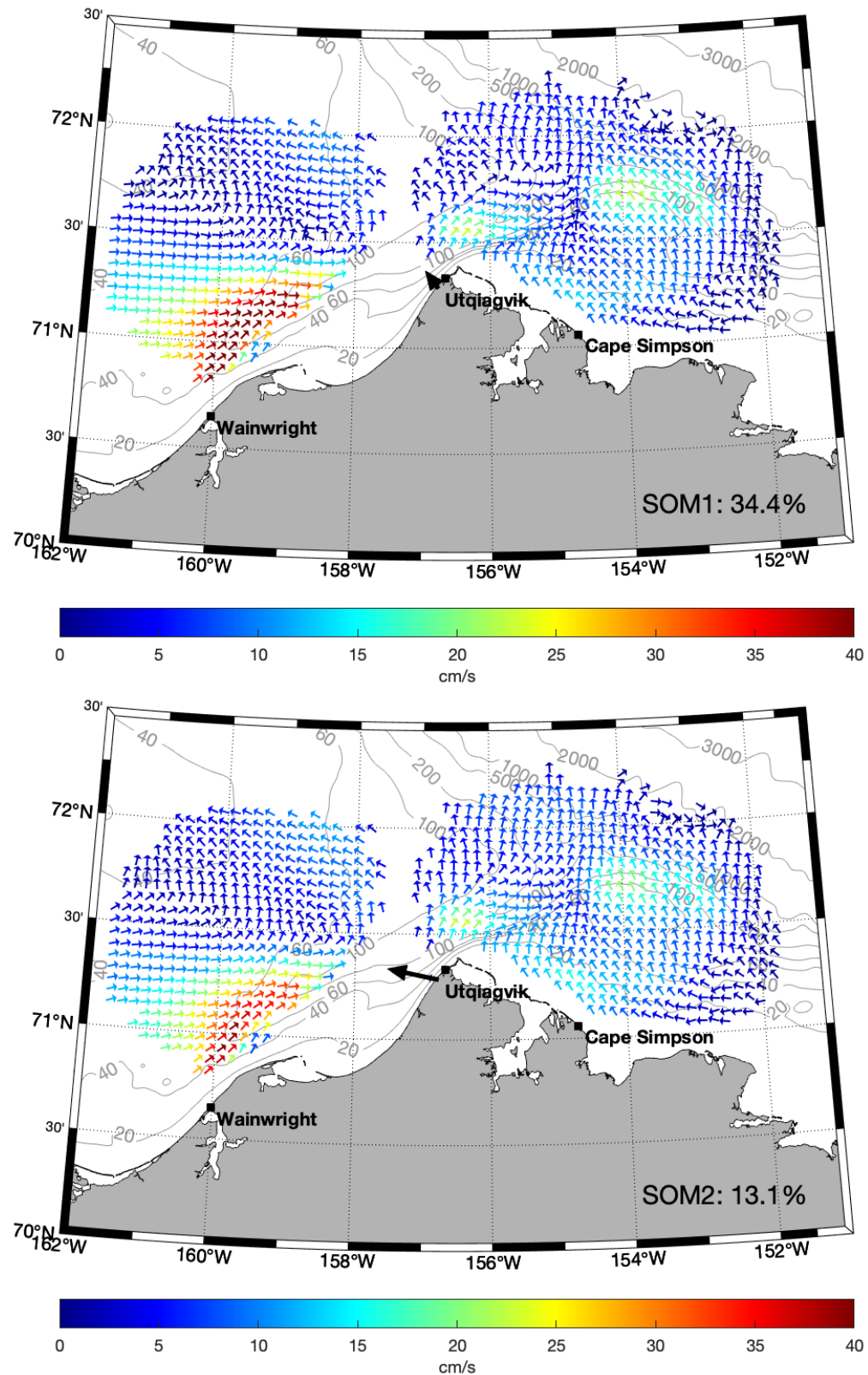


Figure A23: Self-organized map (SOM) patterns 1 (top) and 2 (bottom) for all daily HFR mean maps from 2017.

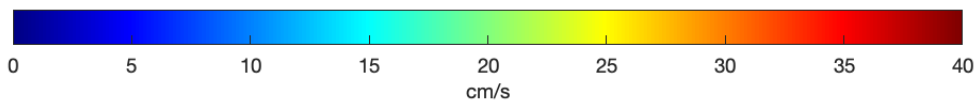
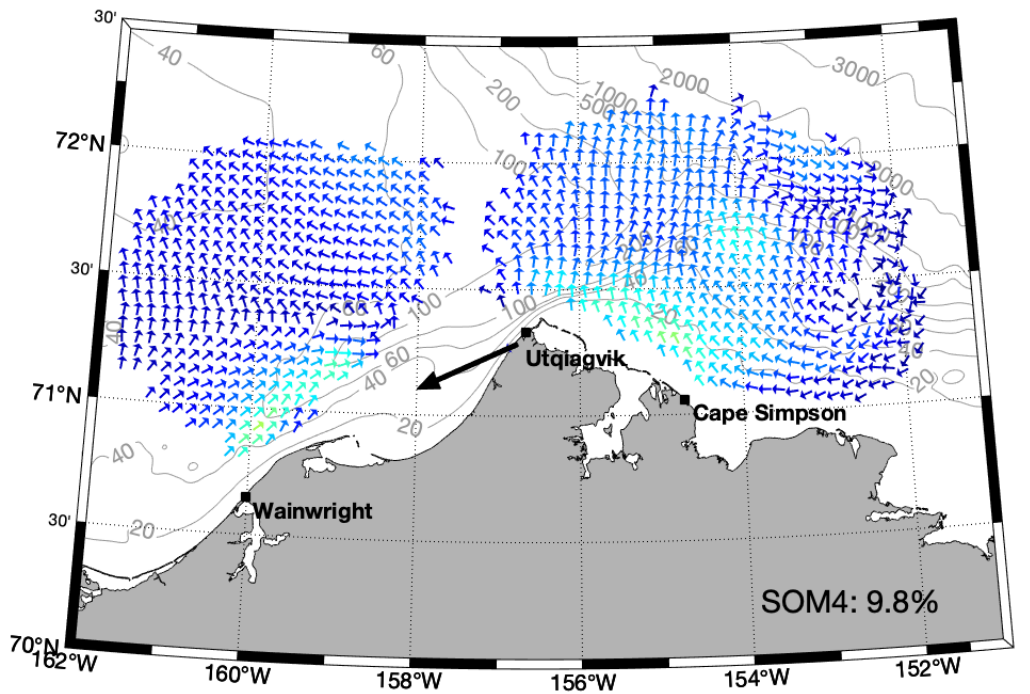
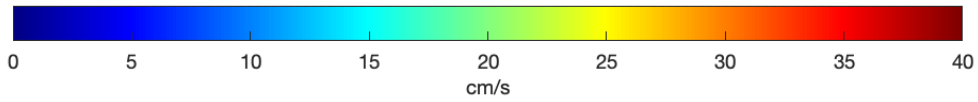
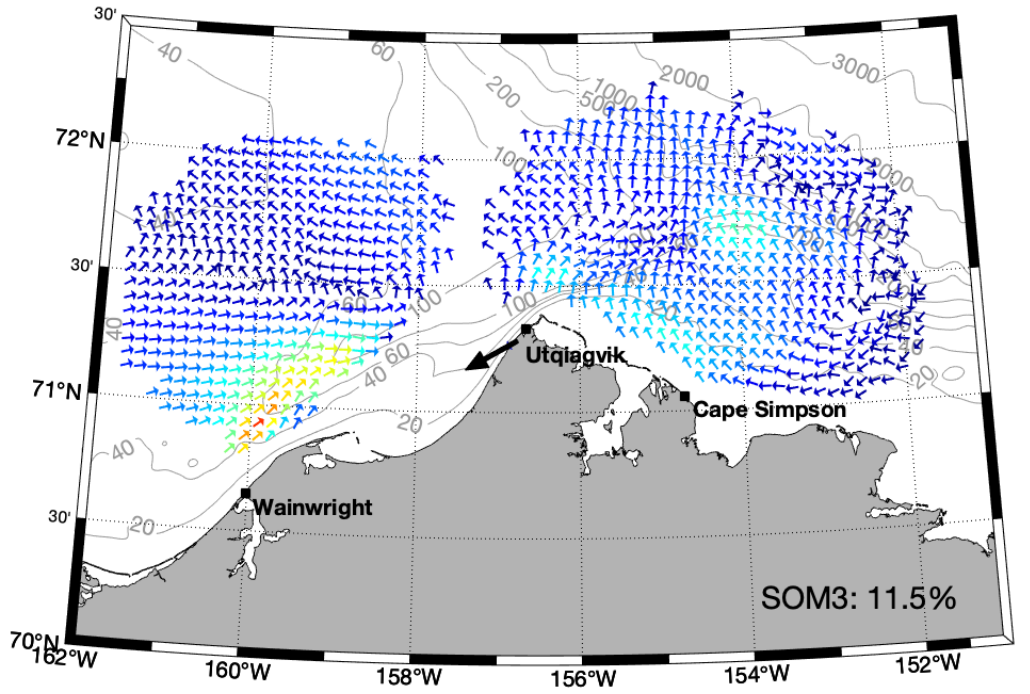


Figure A24: Self-organized map (SOM) patterns 3 (top) and 4 (bottom) for all daily HFR mean maps from 2017.

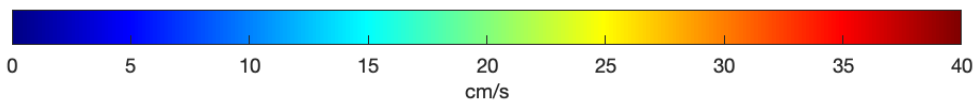
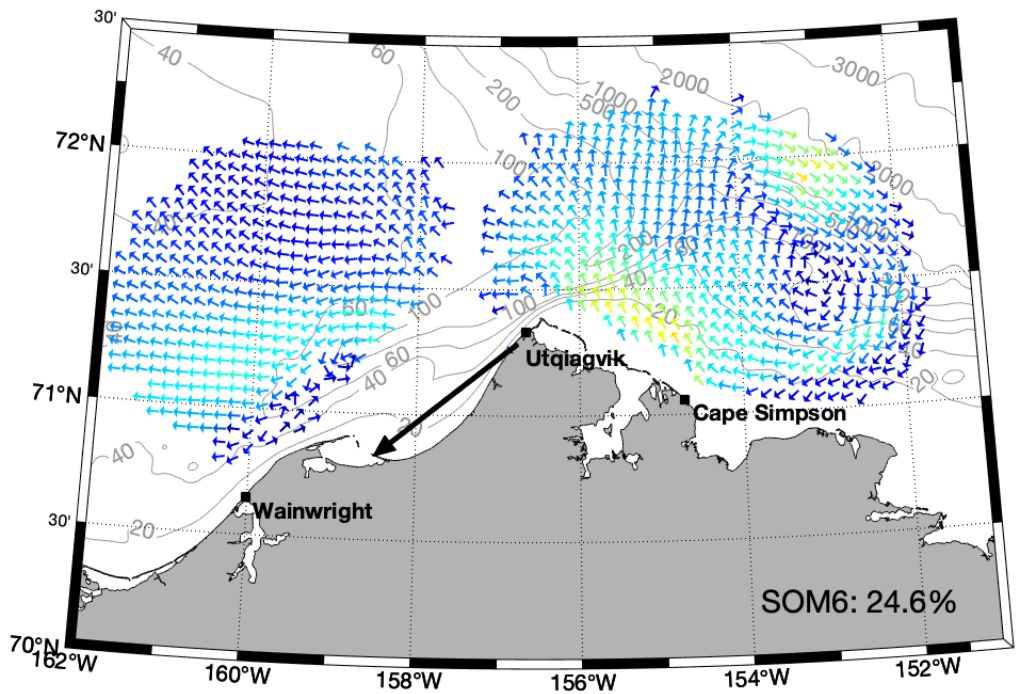
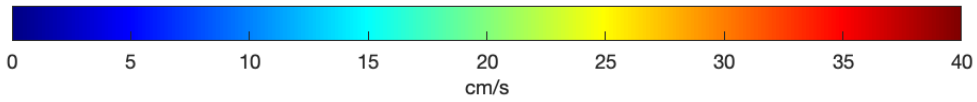
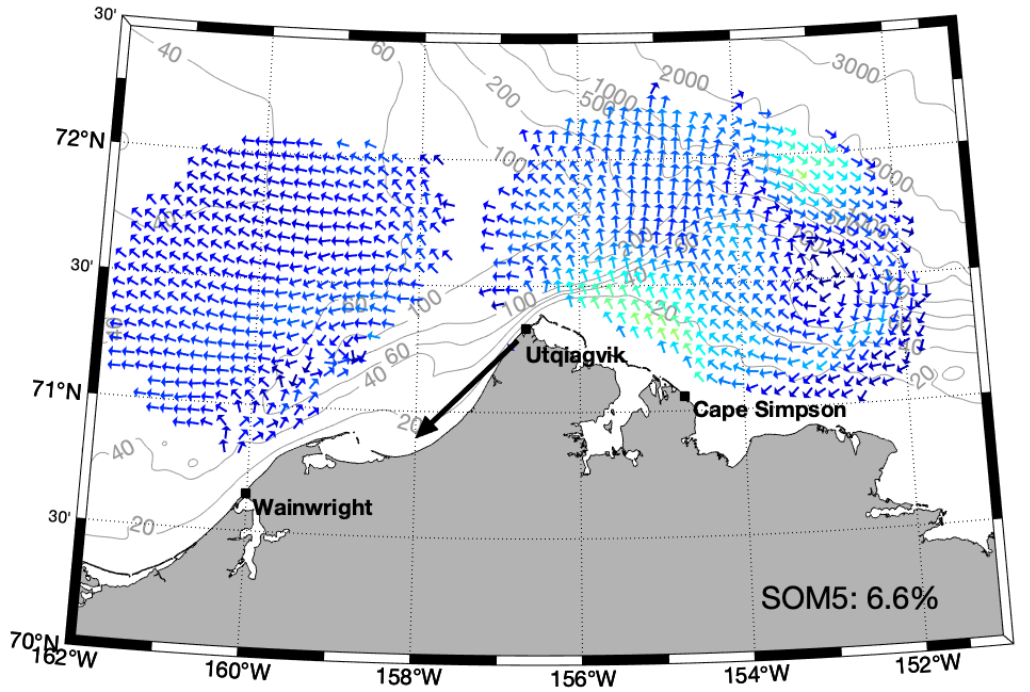


Figure A25: Self-organized map (SOM) patterns 5 (top) and 6 (bottom) for all daily HFR mean maps from 2017.

2018

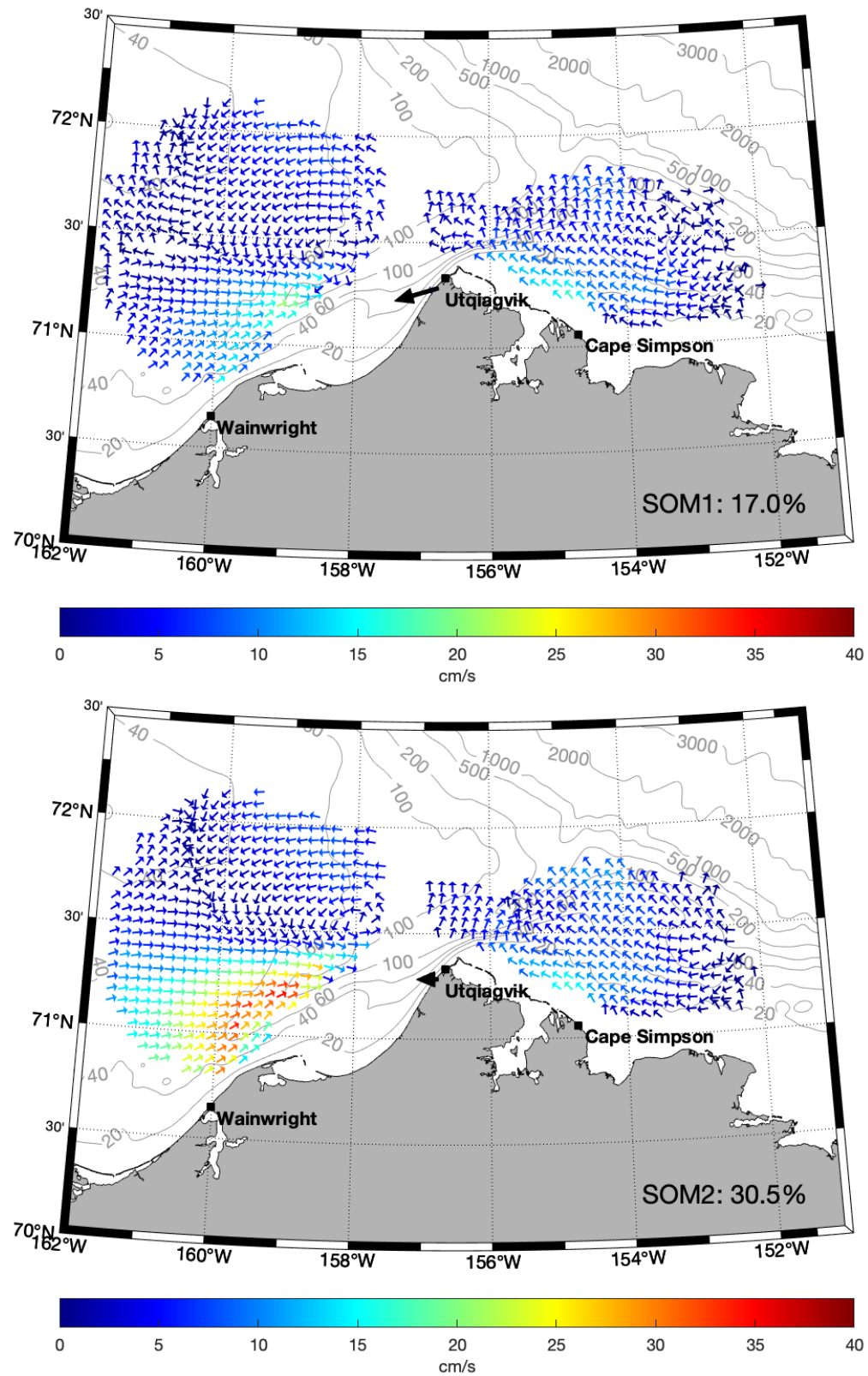


Figure A26: Self-organized map (SOM) patterns 1 (top) and 2 (bottom) for all daily HFR mean maps from 2018.

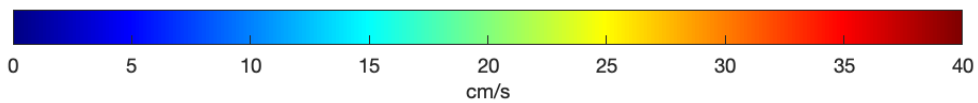
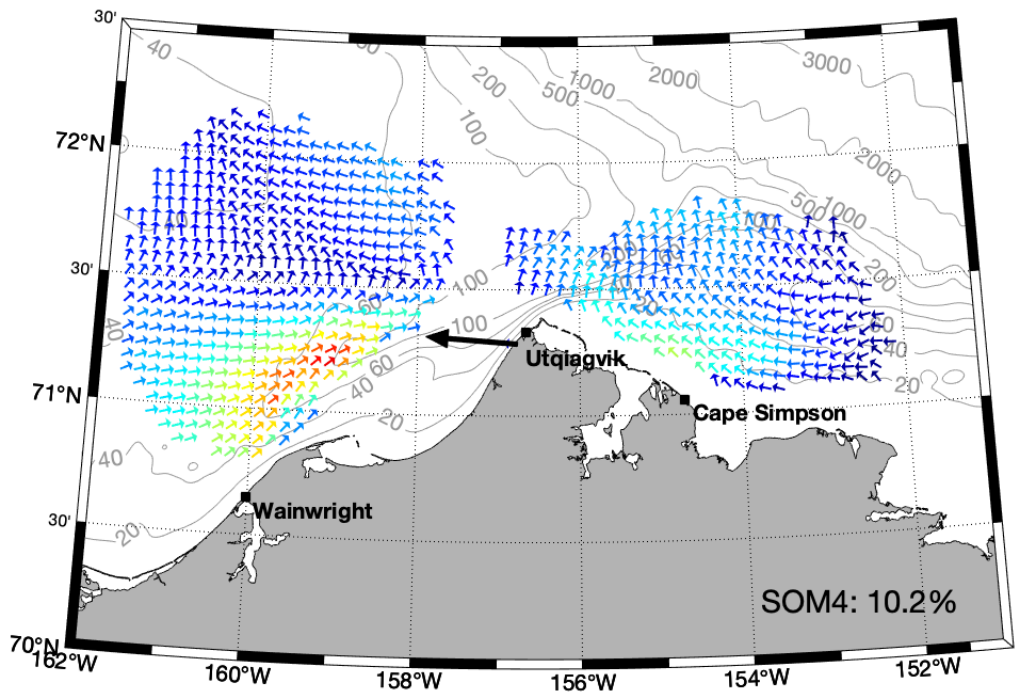
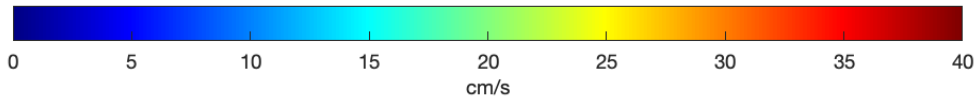
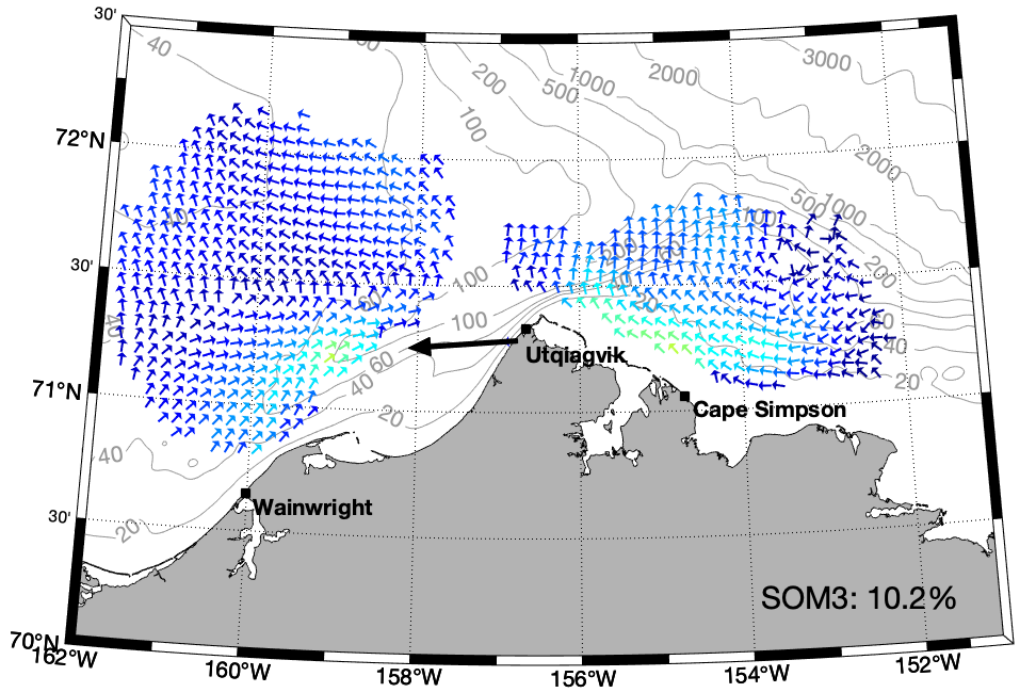


Figure A27: Self-organized map (SOM) patterns 3 (top) and 4 (bottom) for all daily HFR mean maps from 2018.

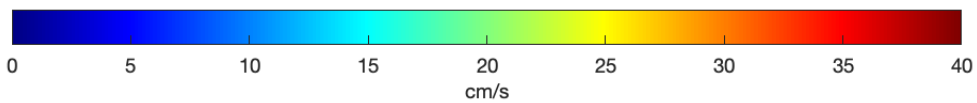
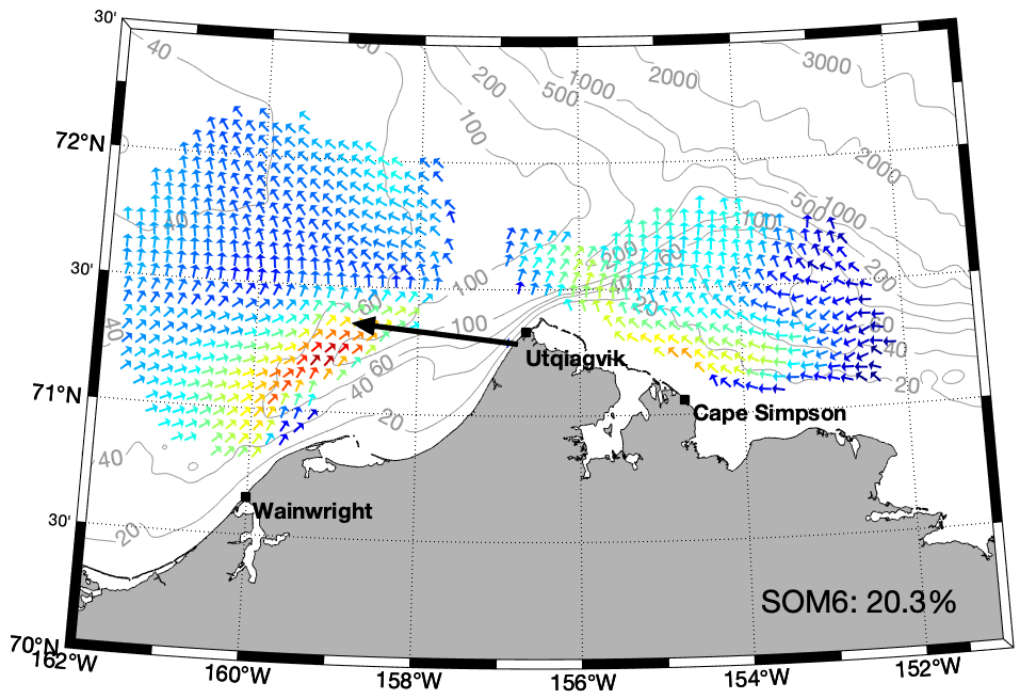
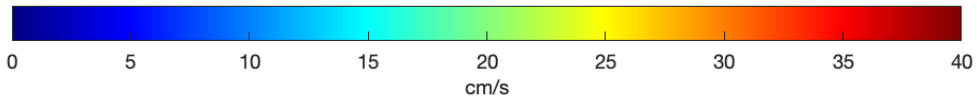
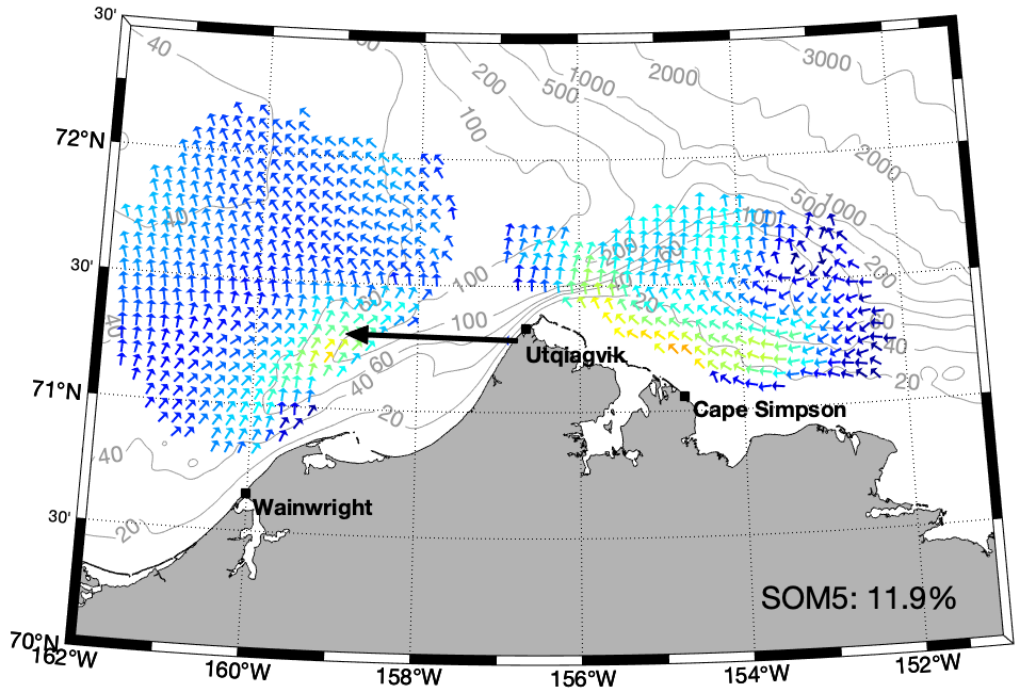


Figure A28: Self-organized map (SOM) patterns 5 (top) and 6 (bottom) for all daily HFR mean maps from 2018.



## **The Department of the Interior Mission**

As the Nation's principal conservation agency, the Department of the Interior has responsibility for most of our nationally owned public lands and natural resources. This includes fostering the sound use of our land and water resources, protecting our fish, wildlife and biological diversity; preserving the environmental and cultural values of our national parks and historical places; and providing for the enjoyment of life through outdoor recreation. The Department assesses our energy and mineral resources and works to ensure that their development is in the best interests of all our people by encouraging stewardship and citizen participation in their care. The Department also has a major responsibility for American Indian reservation communities and for people who live in island communities.



## **The Bureau of Ocean Energy Management**

The Bureau of Ocean Energy Management (BOEM) works to manage the exploration and development of the nation's offshore resources in a way that appropriately balances economic development, energy independence, and environmental protection through oil and gas leases, renewable energy development and environmental reviews and studies.